UNIVERSIDADE DE LISBOA
FACULDADE DE CIÊNCIAS
DEPARTAMENTO DE QUÍMICA E BIOQUÍMICA

Conducting and Redox-Based Copolymeric Materials for Energy Storage

Katherine Valentina da Silva Bettencourt

Mestrado em Química
Especialização em Química

Dissertação orientada por:
Ana Pimenta da Gama Silveira Viana Semedo
Jorge Manuel Palma Correia

2025

Acknowledgements

First and foremost, I would like to thank my supervisors, Dr. Ana Viana and Dr. Jorge Correia, who captivated me with their unique way of communicating science and electrochemistry. You will always stay in my heart as my "*electrochemistry parents*" and as examples of how to explain science in a fun and simple way. I will always remember being welcomed with a big smile the first time I asked to "*do something*" with electrochemistry. Two years later, I am still received with a smile, a joke, or a good scientific discussion. I am deeply thankful and proud to have had you as my supervisors, for all the opportunities you opened to me, for believing in me when I didn't believe in myself, and for your endless patience, even when I broke EQCM and Arrandee electrodes while learning.

To Daniel Santos, thank you for your kindness, for teaching me how to use *in-situ* UV-vis spectroscopy, and for always being available when I needed help. I enjoyed our scientific conversations and everything I learned about PEDOT from you. I also thank Catarina Alves, although our interactions were brief, your advice and passion for science left a lasting impression on me.

To all my colleagues from the *Laboratório de Electroquímica Interfacial e Nanomateriais*, and to Dr. Olinda Monteiro and Dr. Virginia Ferreira, I am grateful to have worked alongside you. To Diana, Mariana, Daniela, Gonçalo, and my colleagues from 8.3.47, thank you for the scientific discussions, random conversations, and for making the lab an enjoyable place every day. To my BSc and MSc friends, later my 3rd-floor corridor companions – Gabriel, Gonçalo, and Eduardo – thank you for the funny and unforgettable moments over the past five years. To my lifelong friends, Bárbara and Johanna, thank you for always being here. To my *velhotes das aguarelas* – Jorge, José, Manuel, and Manuela – and my professor Jorge Alexandre, thank you for teaching me to flow like watercolors flow.

I would particularly like to thank Diana Carneiro, with whom I learned so much professionally and personally. Thank you for your warmth, our conversations about copolymers and electrochemistry (or life in general), for cheering me up, and for always being there when I needed support.

Last but not least, I would like to thank the people closest to me: my parents, my brothers, and my boyfriend. To my parents, Luis and Rita, thank you for your resilience, joy, and support, and for giving me the opportunity to pursue my passion. To my dad, for welcoming me with an *arepa* and my cat Kiki. To my mom, from whom I inherited my curiosity, who always tries to understand my work. To Guillermo, thank you for always believing in me, supporting me, cheering me up when I needed it the most, and lending me your laptop so I could finish this thesis. To Alejandro, from whom I stole my passion for energy, thank you for all our conversations about physics and new energy sources. To my sister-in-law Daniela, for always supporting me to follow my passion and for my nieces Sofia and Andrés, who always make me smile.

To Bruno, my best friend and partner, thank you for staying late at the lab waiting for me, listening to my presentations countless times, supporting me through difficult moments, and celebrating the best ones. Thank you for being my boyfriend, lab-mate, partner in science and in life – for the conversations, sushi dinners, and stand by side through everything.

To Dr. Bárbara Anes and Dr. Luis Santos, thank you for your dedication and availability in measuring FTIR and Raman analyses. I would also like to thank my *alma mater* (FCUL) and all the Professors and colleagues I met in my academic pathway.

Thank you once again to everyone mentioned. Words cannot express how grateful and fortunate I feel to have met you all. I will carry you with me always: "*Yo te llevo dentro, hasta la raíz*."

Resumo

A comercialização das baterias de ião de lítio, iniciada pela SONY em 1991, transformou permanentemente o mercado dos dispositivos eletrónicos, tornando-os parte integrante do dia a dia, desde telemóveis a computadores portáteis. Paralelamente, a crescente preocupação com o aquecimento global e a procura de alternativas às energias renováveis impulsionaram a utilização destas baterias como suporte essencial para infraestruturas de energias renováveis (*e.g.*, solar, eólica) e no setor automóvel, visando reduzir emissões. Apesar do bom desempenho, o seu crescimento trouxe desvantagens, mostrando-se menos sustentável do que se pensava. Assim, a otimização da reciclagem e o desenvolvimento de novas baterias tornou-se essencial para apoiar a economia circular e sustentabilidade.

Com isto em mente, é natural considerar as baterias de ião-sódio como uma alternativa promissora. A sua abundância natural e semelhança química com o lítio as tornam atraentes para a sua aplicação na conversão de energia. Por mais imediato que pareça, a aplicação de materiais desenvolvidos para baterias de ião-lítio nas de sódio revela interações diferentes entre as estruturas hospedeiras e os iões, relacionadas com o tamanho do ião sódio, comportamento eletroquímico e coeficientes de difusão aparentes. Um desafio crucial nos cátodos das baterias de ião-sódio são as reações secundárias durante os ciclos da bateria, que podem levar ao colapso estrutural do material, particularmente em materiais inorgânicos, com estruturas mais rígidas. Assim, é fundamental repensar o desenho dos materiais de cátodo para otimizar o seu desempenho.

Considerando o papel crucial do cátodo nas baterias de ião-sódio, os cátodos à base de compostos orgânicos surgem como alternativa promissora. Estes materiais apresentam baixo custo, facilidade de modificação, e flexibilidade para incorporar iões. Entre eles, destacam-se os materiais à base de compostos com grupos carbonilo e polímeros condutores, com desempenho comparável a alguns materiais inorgânicos. Embora apresentem limitações, a combinação complementar destas duas classes de materiais permite obter cátodos híbridos com boas capacidades específicas, maior estabilidade e elevado potencial para a sua aplicação em baterias de ião sódio.

Os cátodos à base de compostos orgânicos são uma alternativa promissora, sobretudo pela possibilidade de modificação para otimizar as suas propriedades. Por este motivo, neste trabalho estudou-se a eletrossíntese de materiais híbridos à base de polidopamina (PDA) e poli(3,4-etilenodioxitiofeno) (PEDOT). A PDA destaca-se pela forte adesão a superfícies, devido aos grupos catecol e amina, que mimetizam aminoácidos presentes nas proteínas adesivas do mexilhão, promovendo interações intermoleculares e reações químicas. No entanto, a sua natureza isolante limita o crescimento por eletropolimerização e o desempenho eletroquímico. O PEDOT, por sua vez, apresenta boas propriedades condutoras, estabilidade química e compatibilidade biológica.

Inicialmente, a eletrossíntese potenciodinâmica de filmes de PDA/PEDOT foi estudada no intervalo de -800 a 900 mV *vs.* Ag/AgCl, durante 10 ciclos a 50 mVs^{-1}, em 10 mM de 3,4-etilenodioxitiofeno (EDOT), 20 mM de dopamina (DA) e 50 mM de sal dissódico de sulfato de dextrano (DS). Visto que a deposição dos filmes foi pouco significativa, o estudo foi prolongado para 50 ciclos e acompanhado por Microbalança Eletroquímica de Cristal de Quartzo (EQCM, do inglês *Electrochemical Quartz Crystal Microbalance*). A partir deste ensaio concluiu-se que este método de síntese não era eficiente e, por este motivo, avançou-se ao estudo da deposição dos filmes por métodos potenciostáticos.

Com os estudos prévios, foi possível selecionar uma gama ideal de potenciais para depositar potenciostaticamente os filmes de PDA/PEDOT. Assim, os filmes foram sintetizados em 10 mM de EDOT, 20 mM de DA e 50 mM de DS, aplicando diferentes potenciais (-800 a 950 mV *vs.* Ag/AgCl)

durante 320 s. A caracterização eletroquímica posterior mostrou que a deposição dos filmes copoliméricos foi bem sucedida, mostrando propriedades híbridas de ambos os materiais: do PEDOT, a pseudocapacidade característica deste material, e da PDA, o processo redox característico quinona/catecol. Observou-se ainda que, quanto maior o potencial aplicado, maior era a atividade eletroquímica de ambas as funcionalidades. Por este motivo, 950 mV *vs.* Ag/AgCl e 320 s foram escolhidos como parâmetros eletroquímicos.

Uma vez selecionados os parâmetros electroquímicos, foram avaliados outros parâmetros de síntese para otimizar as propriedades redox destes filmes. Quando a concentração de monómeros de DA foi aumentada para 40 mM, observou-se uma diminuição do comportamento pseudocapacitivo do material e uma resposta quinona/catecol semelhante. Por outro lado, quando se testou uma concentração inferior de eletrólito (10 mM DS) ou diferentes eletrólitos (50 mM de dodecilsulfato de sódio e poli(4-estirenosulfonato de sódio)), também se verificou uma diminuição tanto da resposta pseudocapacitiva como do comportamento redox quinona/catecol.

Após a otimização, as melhores condições dentro dos parâmetros testados foram 20 mM de DA, 10 mM de EDOT e 50 mM de DS, a um potencial constante de 950 mV *vs.* Ag/AgCl durante 320 segundos. Nessas condições, não se observou deposição para a PDA pura, enquanto os filmes de PEDOT puro apresentaram uma resposta pseudocapacitiva comparável à do copolímero PDA/PEDOT. Posteriormente, estudos com EQCM revelaram cinéticas de deposição muito diferentes, sendo que o filme de PEDOT atingiu cerca do dobro da massa do copolímero no final da síntese.

Uma vez escolhidas as condições de síntese, o filme copolimérico foi caracterizado por métodos físico-químicos. Inicialmente, para comparar os modos de deposição do copolímero com o filme de PEDOT, estes foram acompanhados e caracterizados durante diferentes tempos de deposição (40 s, 160 s, 240 s e 320 s) usando voltametria cíclica, EQCM e Microscopia de Força Atómica (AFM, do inglês *Atomic Force Microscopy*). Os resultados mostraram que os filmes copoliméricos de PDA/PEDOT apresentam morfologia uniforme e compacta, muito diferente da estrutura porosa e irregular do PEDOT. Observou-se que, durante a deposição, o copolímero passa de uma forma muito densa e uniforme, com menor composição de PEDOT, para uma morfologia ligeiramente menos uniforme e menos compacta, refletindo maior incorporação de PEDOT e PDA. Estes resultados foram posteriormente suportados pela análise da composição estrutural e molhabilidade dos filmes (FTIR, Raman e gonoimetria ângulos de contacto), bem como pela avaliação dos parâmetros dielétricos, por elipsometria.

Adicionalmente, a deposição e caracterização dos filmes de PDA puro, PEDOT puro e do copolímero foram acompanhadas por UV-vis de refelectância *in-situ*. A análise espectroscópica dos filmes sugeriu a possível incorporação de espécies oligoméricas DA-EDOT, devido às alterações observadas no espectro em comparação com a deposição dos filmes puros. Por outro lado, a caracterização eletroquímica dos filmes em $NaClO_4$ (0,1 M) mostrou que, apesar da incorporação das funcionalidades da PDA, o comportamento do copolímero como polímero condutor não é comprometido, apresentando variações espectrais durante a oxidação e redução, típicas de polímeros condutores. A diferença no espectro durante estudos de UV-vis *in-situ* dos filmes copoliméricos em comparação com o PEDOT puro no estado oxidado indica que a conjugação e a ligação dos monómeros de EDOT foram alteradas, sugerindo novamente a possível incorporação de oligómeros DA-EDOT.

Finalmente, o copolímero PDA/PEDOT sintetizado e o polímero puro de PEDOT foram testados e comparados como materiais de cátodo para baterias de ião-sódio. Como abordagem inicial, os materiais foram depositados potenciostaticamente sobre elétrodos de ouro, permitindo acompanhar a variação de massa por EQCM durante os ciclos de carga e descarga e obter informações sobre a degradação do

material. Os filmes de copolímero e PEDOT foram depositados respetivamente durante 95 s e 20 s a 950 mV *vs.* Ag/AgCl, e posteriormente analisados em $NaClO_4$ (0,1 M) por 1000 ciclos, aplicando pulsos de -600 mV e 700 mV (*vs.* Ag/AgCl) durante 5 segundos cada. Os resultados mostraram que, no caso destes filmes finos depositados em ouro, apesar do copolímero apresentar o dobro da capacidade específica, sofreu maior degradação (33 % de perda de capacidade), enquanto o filme de PEDOT apresentou melhor retenção (16 % de perda de capacidade).

Posteriormente, os filmes foram depositados em grafite para uma abordagem mais sustentável e menos dispendiosa. Neste caso, o copolímero foi depositado durante 320 s e o filme de PEDOT durante 135 s aplicando um potencial de 950 mV *vs.* Ag/AgCl. O filme foi testado também em $NaClO_4$ (0,1 M) aplicando pulsos de -600 mV e 700 mV (*vs.* Ag/AgCl) durante 5 segundos cada, mas neste caso durante 1500 ciclos. Surpreendentemente, apesar de ambos os filmes apresentarem uma capacidade semelhante, a retenção da capacidade do copolímero aumentou significativamente, face ao PEDOT, mostrando uma perda de apenas 4%. Em contraste, o PEDOT sofreu uma maior degradação de 34 %.

Os ciclos de carga e descarga galvanostática dos filmes foram também analisados. No entanto, após a caracterização e o estudo dos filmes a diferentes *C-rates*, verificou-se a interferência de uma reação parasita durante os ciclos de carga e descarga, possivelmente associada à redução do oxigénio. Por este motivo, este tipo de ciclagem não pôde ser abordada nesta fase e deverá ser explorada futuramente, após a otimização do material do elétrodo e parâmetros experimentais.

Em suma, o presente trabalho conseguiu demonstrar, pela primeira vez, a síntese otimizada de filmes copoliméricos de PDA/PEDOT, seguida de uma caracterização físico-química detalhada e da sua aplicação como materiais de cátodo. A abordagem permitiu compreender a relação entre os parâmetros de síntese, a morfologia e as propriedades eletroquímicas dos filmes, evidenciando o potencial destes copolímeros para baterias de ião-sódio.

Palavras-chave: Polidopamina, PEDOT, Polímeros Condutores, Eletropolimerização, Baterias de Ião-Sódio.

Abstract

Lithium-ion batteries are every day at the palm of our hands in smartphones, laptops, and watches. However, with their growing demand, environmental repercussions have come to light, creating an urgent need for alternative battery chemistries. Sodium-ion batteries are a promising alternative due to their natural abundance and chemical similarity to lithium. Despite this, Li-ion technology cannot be directly applied to Na-ion systems since the larger sodium ions destabilize crystalline matrices during battery cycles, making it necessary to rethink electrode materials.

Organic cathode materials have gained attention for sodium-ion batteries, being flexible, sustainable, and cost-effective. Among them, carbonyl compounds and conducting polymers stand out. Yet, their low energy densities limit their use. To address this, the present work intends to combine both materials to give place to a hybrid coating with improved stability that can be further modified to increase the specific capacity of the material. In this work, dopamine (DA) and 3,4-ethylenedioxythiophene (EDOT) were electropolymerized to combine their distinct functionalities into a copolymer with enhanced properties. PDA offers strong surface adhesion and easy chemical modification, while PEDOT is known for its good conductivity and chemical stability.

During this study, the electrosynthesis of a PDA/PEDOT copolymer was explored, testing various applied potentials, electrolytes, and monomer proportions to optimize it as a cathode. The extensive physicochemical characterization of the copolymer supported the successful combination of these materials, with the electroactivity of the film showing the typical pseudocapacity of PEDOT and the quinone/catechol redox of PDA. Techniques such as FTIR, Raman, AFM, ellipsometry, and *in-situ* UV-vis, alongside electrochemical methods, allowed detailed analysis of the film's composition, morphology, thickness, and optoelectronic properties. When tested as cathode, the copolymer showed greater stability and specific capacities than PEDOT, retaining 96 % capacity after 1500 cycles, highlighting its potential as a platform for next-generation hybrid organic cathodes.

Keywords: Polydopamine, PEDOT, Conducting Polymers, Electrocopolymerization, Sodium-Ion Batteries.

Scientific Outputs

The work developed during this dissertation gave place to 5 scientific communications – 2 oral presentations and 3 posters.

Oral Presentations (National)

1) Bettencourt, Katherine; Correia, Jorge P.; Viana, Ana S. "*Powering Everyday Life: Designing Copolymeric Cathode Materials for Sustainable Ion-Batteries"*. Presented at *XXIX Encontro Nacional da SPQ*, Coimbra, Portugal, 2025.
2) Bettencourt, Katherine; Viana, Ana S.; Correia, Jorge P. "*Copolymeric Cathode Material for Sodium-Ion Battery"*. Presented and Awarded as the Best Oral Communication at *CQE Days*, Lisbon, Portugal, 2024.

Poster Presentations (National / International)

1) Bettencourt, Katherine; Viana, Ana S.; Correia, Jorge P. *"Unraveling the Electrosynthesis of Copolymeric Film Deposition".* Presented at *CQE Days 2025*, Lisbon, Portugal, 2025.
2) Bettencourt, Katherine; Correia, Jorge P.; Viana, Ana S. "*Flexible Host Materials for Energy Storage"*. Presented at *16th National Physical Chemistry Meeting*, Lisbon, Portugal, 2024.
3) Bettencourt, Katherine; Correia, Jorge P.; Viana, Ana S. "*A Versatilidade dos Copolímeros: Matrizes Baseadas em Dopamina e Tiofeno"*. Presented at *Sociedade Ibero-Americana de Eletroquímica (SIBAE),* Lisbon, Portugal, 2024.

Index

Table Index

Figure Index

Abbreviation Index

AFM	Atomic Force Microscopy
AQ	Anthraquinone
BQ	1,4-Benzoquinone
ca.	Around (from Latin, *circa*)
CB	Conducting Band
CPB	Citrate-Phosphate Buffer
CV	Cyclic Voltammetry
DA	Dopamine
DS	Dextran Sodium Sulfate
e.g.	For example (from Latin, *exempli grati*)
EDOT	(3,4-ethylenedioxythiophene)
EDS	Energy-Dispersive X-Ray Spectroscopy
EIS	Electrochemical Impedance Spectroscopy
EQCM	Electrochemical Quartz Microbalance
et al.	And others (from Latin, *alia*)
FTIR	Fourier Transform Infrared Spectroscopy
GC	Glassy Carbon
HOMO	Highest Occupied Molecular Orbital
In-situ	On site (from Latin)
LIB	Lithium-Ion Battery
LUMO	Lowest Unoccupied Molecular Orbital
MO	Molecular Orbital
MW	Molecular Weight
NQ	Naphthoquinone
ORR	Oxygen Reduction Reaction
PAAQ	Poly(aminoanthraquinone)
PANI	Polyaniline
PB	Phosphate Buffer
PBD	Probe Beam Deflection
PDA	Polydopamine
PEDOT	Poly(3,4-ethylenedioxythiophene)
PHQ	Polyhydroquinone
PPy	Polypyrrole
PQ	Phenanthrenequinone
PSS	Poly(4-styrenesulfonate)
SDS	Sodium Dodecyl Sulfate
SEM	Scanning Electron Microscopy
SHE	Standard Hydrogen Electrode
SIB	Sodium-Ion Battery
SPB	Sodium Phosphate Buffer
SPM	Scanning Probe Microscopy
UV-vis	Ultraviolet-visible
VB	Valence Band
vs.	Against (from Latin, *versus*)
WCA	Water Contact Angle
XPS	X-Ray Photoelectron Spectroscopy

Symbols

α	Absorption coefficient of the material
$\bar{z}$	Average Height
ψ	Azimuthal angle (°)
C^*	Bulk concentration of electroactive specie (mol cm^{-3})
I_c	Capacitive Current (A)
ρ	Complex reflectance ratio
N	Complex refractive index
N_f	Complex refractive index of film
j	Current density (A cm^{-2})
j_p	Current Peak Density (A cm^{-2})
D	Diffusion coefficient (cm^2 s^{-1})
A	Electrode area (cm^2)
E_g	Energy Band Gap (eV)
k	Extinction coefficient of the material
I_f	Faradaic Current (A)
F	Faraday's constant (96485 C mol^{-1})
L_f	Film thickness (Å)
E_f	Final Potential (V)
$E^{0'}$	Formal Potential (V)
Δf	Frequency shift (Hz)
$\hat{r}_p$	Fresnel reflection coefficient of the *p* component
R	Gas constant (8.314 J mol^{-1} K^{-1})
z_i	Height of point i
E_i	Initial Potential (V)
r	Ionic radius (Å)
q_1	Light propagation angle in the environment (°)
q_2	Light propagation angle in the substrate (°)
λ	Light wavelength (nm)
γ_{lv}	Liquid-vapor interfacial tension (N m^{-1})
Δm	Mass change (g)
E_p	*p* component of the electric field vector
i_p	Peak Current (V)
E_p	Peak Potential (V)
Δ	Phase difference (°)
A	Piezoelectrically active area (cm^2)
E	Potential (V)
$E_{\tau/4}$	Quarter wave potential (V)
ρ_q	Quartz density (2.648 g cm^{-3})
n_1	Refractive index of environment
n_2	Refractive index of substrate
n	Refractive index of the material
f_0	Resonant frequency of the quartz crystal (7978181 Hz)
R_q	Root mean square roughness of a sample
μ_q	Shear modulus of AT-cut quartz (2.947×10^{11} dyn cm^{-2})
γ_{sl}	Solid-liquid interfacial tension (N m^{-1})
γ_{sv}	Solid-vapor interfacial tension (N m^{-1})

E^o	Standard electrode potential (V)
Γ	Surface coverage (mol cm^{-2})
v	Sweep Rate (V s^{-1})
T	Temperature (K)
t	Time (s)
n	Transferred number of electrons
τ	Transition time (s)
θ	Young's contact angle (°)

Chapter 1
Introduction

"...No place is more filled with imaginary voices that a library or a lab. Whether you read a book or a lab report, you silently converse with its writer – and through her with everyone else she has read"

Wayne C. Booth, Gregory G. Colomb and Josep M. Williams in *The Craft of Research*

1. Introduction

1.1 From Lithium to Sodium-Ion Batteries

The intricate nature of energy is present in all aspects of human life, shaping society and transforming how we communicate, live, and interact.[1,2] Yet, our dependence on fossil fuels has led to severe environmental consequences, with carbon emissions being the main driving source of global climate change. This challenge has led to the need for a transition toward sustainable alternatives.[3,4]

Since the late 20th century, renewable energy has gained increasing popularity as a means to mitigate greenhouse gas emissions, becoming a key part of global energy infrastructure.[5] By 2023, renewables accounted for 46% of total energy production, emerging as the leading energy source.[6] Despite this, the efficiency of solar, wind, geothermal, and hydropower remains constrained by environmental conditions.[7] In this context, electrochemical energy storage is fundamental to reduce fossil fuel reliance, supporting reliability and meeting growing demands of the energy grid.[4,8]

Among the electrochemical storage technologies, rechargeable batteries are the most versatile systems due to their simplicity, sustainability, portability, and conversion efficiency.[4,7,9] These devices store and provide energy by reversibly converting chemical energy into electricity and typically consist of an anode, cathode, and electrolyte.[10] In recent years, Lithium-ion Batteries (LIBs) have gained attention as leading candidates for large-scale energy applications.[11] Given their relevance, the following subchapters will briefly overview their development and main drawbacks.

1.1.1 The Lithium-Ion Battery Revolution

During the 1980s, rechargeable batteries in electronic devices were primarily based on lead-acid and nickel-cadmium chemistries. While these were essential for early technological advancements, their bulky and heavy nature limited the development of lighter and more compact portable devices. As a result, the need for a new small and lightweight rechargeable battery became of growing interest.[12]

To maximize the energy stored in a rechargeable battery, it is essential to ensure a large potential difference between the anode and the cathode, minimize material mass and volume per transferred electron, and prevent unwanted reactions with the electrolyte.[1] Given these demands, lithium chemistry quickly caught the attention as a promising candidate due to its low atomic weight and high electropositivity (-3.04 V *vs*. Standard Hydrogen Electrode, SHE), enabling the design of batteries with high specific energy and energy density.[13,14]

As shown in **Figure 1.1**, lithium-ion batteries operate via a "*rocking chair*" mechanism: during charging, lithium ions migrate from the cathode and are stored in the anode. During discharge, they intercalate back into the cathode.[7,10] While ions move through the electrolyte, electrons flow through an external circuit, generating electrical energy.[10] This can be visualized as "*game of tennis*", where the electrodes are the players and the tennis ball is the lithium-ion. The ion moves back and forth if the players are robust and fast.

The commercialization of lithium-ion batteries was delayed nearly a decade due to the lack of suitable negative electrode materials.[14] After extensive research, carbon-based materials, especially graphite, became the preferred anodes. Positive electrodes usually consist of structured materials with 3d transition metals (*e.g.*, Co, Mn, Fe, Ni), with layered oxides and polyanionic compounds showing great performance.[15] After years of optimizing both energy storage and portability safety, SONY commercialized the first lithium-ion battery in 1991.[12] This breakthrough revolutionized technology, enabling portable electronics like laptops and smartphones, transforming daily life.[11]

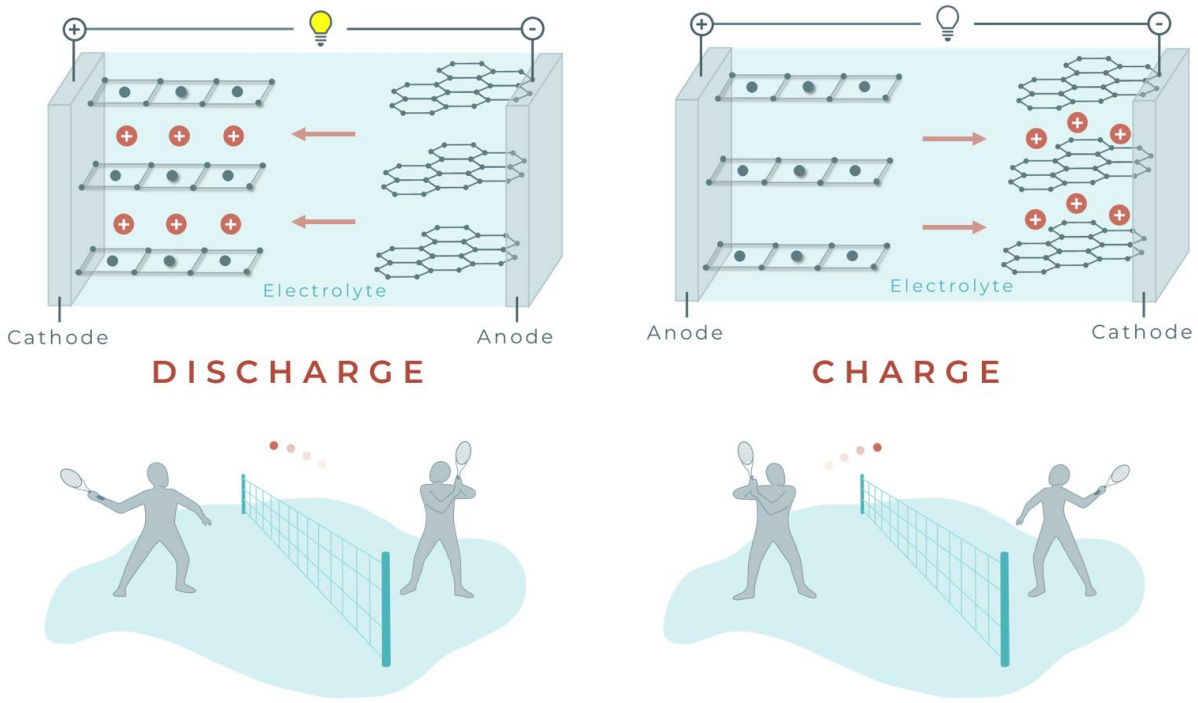

Figure 1.1 – Schematic representation of charge and discharge of an ion battery and the "tennis game" analogy.

1.1.2 Pitfalls of Lithium-Ion Batteries

Since their commercialization, lithium-ion batteries have become integral to daily life and caught attention for broader uses, especially in decarbonizing transportation.[15] As a result, lithium-ion batteries began to be sought in sectors where weak energy infrastructures required reinforcements.[16] However, the growing demand for these batteries, along with the increasing waste generated from their use, brought significant challenges.[16,17]

One of the most controversial challenges of LIBs is the uneven resource distribution and ethical issues related to mining extraction, which contribute directly to their increasing costs.[18,19] Lithium reserves are primarily concentrated in Australia, Chile, and Argentina, while the copper used in current collectors is mainly sourced from the Democratic Republic of the Congo.[16,17] Their extraction processes face social, ethical, and environmental problems, including excessive water use, harm to local communities, and risks of child labor in artisanal mining.[16]

These critical consequences demand alternatives to current rechargeable batteries, through better recycling or new battery chemistries.[13,17] Even though recycling reduces landfill waste, it may not keep pace with the rapid growth of electric vehicles.[16] Moreover, stockpiling used batteries presents safety and environmental hazards. Recycling processes themselves require a superfluous amount of materials, and disassembling battery modules poses significant safety risks, including electrocution, short circuiting, and the release of hazardous byproducts such as HF gas.[16,20]

Combined with future advancements in battery recycling, a shift toward other ion chemistries could help minimize the secondary repercussions associated with LIBs. In this context, battery technologies based on sodium, magnesium, and aluminum have gathered growing attention due to their natural abundance and potential lower costs compared to lithium.[15,21] However, transitioning to new chemistries implies a profound re-evaluation of electrode materials and battery architectures. In the following subchapters, Sodium-Ion Batteries (SIBs) will be introduced, highlighting their main advantages and limitations when compared to LIBs.[21]

1.1.3 The Sodium-Ion Battery: New Materials and Perspectives

Given that lithium and sodium are in the same periodic group, their chemical similarity might suggest a smoother transition between the two ions. Sodium's abundance and low cost make it attractive for large-scale use. Unlike lithium, sodium doesn't alloy with aluminum, allowing cheaper current collectors and fewer ethical concerns.[17] During the early development of LIBs in the 1970s, SIBs were also being explored, operating through the same "*rocking chair*" mechanism.[7,15] However, lithium's superior performance soon overshadowed sodium-ion battery development.[9]

Transitioning from lithium to sodium is not straightforward despite their similar chemical behavior. Sodium ions (r = 1.02 Å; MW (Molecular Weight) = 23 g mol^{-1}) are larger and heavier than lithium ions (r = 0.76 Å; MW = 6.9 g mol^{-1}).[18] Additionally, sodium has a less negative standard electrode potential (-2.71 V *vs.* SHE for Na^+/Na) when compared to lithium (-3.02 V *vs.* SHE for Li^+/Li) and exhibits a less polarizing nature.[7,15] These differences directly compromise how sodium ions interact with host materials, resulting in lower apparent diffusion coefficients and kinetically sluggish processes.[15,22]

An example of this are graphite anodes,[a] which easily intercalate lithium but are ineffective for sodium ion storage.[15] However, alternative non-graphitic materials have proven to be more suitable as anodes for SIBs.[18] Indeed, early evidence suggests that some electrode materials that are incompatible with lithium may perform well with sodium. Therefore, the major challenge in advancing SIBs lies in identifying and optimizing electrode materials that efficiently accommodate sodium ions.[11]

Considering the crucial role of cathode materials in optimizing SIBs performance, this work focuses on developing a new cathode material.[2] Current SIB materials are largely inspired by compounds designed for lithium-ion batteries.[9] To date, three categories stand out: transition metal oxides, polyanionic compounds, and Prussian blue analogues[b] (*e.g.*, layered $LiCoO_2$, olivine $LiFePO_4$).[24] These are summarized in **Table 1.1**, showing their advantages and challenges.[13,27,28] Despite their promising properties, many suffer rapid capacity decay due to irreversible structural changes during cycling.[2] This challenge demands a change in perspective, moving towards the design of novel cathode materials for SIBs.[7,22]

Organic compounds have recently gained attention as alternative cathode materials for energy storage. Composed of abundant elements like C, N, H, and O, they offer more sustainable and cost-effective options. Their lightweight and flexible nature also helps address stability concerns.[27] Given their relevance, the next chapter explores various types of organic cathodes and reviews key materials studied in the literature.

---

[a] Currently, carbon-based anodes are the most studied, though metal ions and alloys are also being explored.[23–25] While graphite is used in LIBs, sodium cannot intercalate in this material for reasons that remain unclear.[15,23] Instead, hard carbons (with disordered structures) are applied in SIBs, enabling sodium adsorption and desorption. Their mechanisms of sodium insertion and kinetic limitations remain poorly understood, keeping anode materials an active research field.[15,23]

[b] The most studied cathode materials in sodium batteries are inevitably those derived from previous research on lithium batteries, primarily based on 3d-transition metal crystal lattices.[15,24]

- *Layered metal oxides* can be described by the general formula Na_xMO_2, where M corresponds to a transition metal, and their structure is composed of alternating octahedral layers of MO_6 and NaO_6 that share edges.[7]
- *Polyanionic* materials follow the general formula $NaM_x(XO_y)_z \cdot nH_2O$, where M corresponds to a transition metal and X to a non-metal element (commonly P, S, Si, As, Mo, or W). According to the type of polyanion, they can be classified as phosphates, sulfates, silicates, borates, and mixed-polyanion materials.[23,24]
- *Prussian Blue analogues* follow the general formula $A_xM_1[M_2(CN)_6]_yV(1-y)_n \cdot H_2O$, where M_1 and M_2 correspond to transition metals, and V represents cyanogen vacancy defects.[26]

Table 1.1 – Advantages and challenges of the three main categories of cathode materials for SIBs.[15,27,28]

Cathode	Advantages	Challenges
Layered Transition Metal Oxides	High energy density and specific capacities. Structural versatility. Potential scalability.	Structural degradation during cycling. Reduction of ion diffusion coefficient. Sensitive to moisture.
Polyanionic Compounds	Stable frameworks. High operating voltage. Excellent thermal stability.	Poor cycling stability and specific capacity. Low electronic conductivity. High production costs.
Prussian Blue Analogs	Low production costs. Adjustable working voltage.	Low electrochemical efficiency. Low chemical and structural stability.

1.2 Organic Cathode Materials for Flexible Sodium-Ion Batteries

The search for organic cathode materials began early with lithium-ion battery development but declined with advancements of inorganic materials.[29] In recent years these materials caught the attention for their use in SIBs, meaning the area is in its early stages.[30] Organic materials are promising candidates for more sustainable batteries, as they can be produced from biomass resources, processed and recycled at low temperatures, and their flexible structure accommodates larger ions, such as sodium.[29]

These materials present high energy densities, fast ion kinetics, and extended cycle life.[31] As summarized in **Table 1.2**,[32] their development has been hindered by their tendency to dissolve in electrolytes, their low specific capacities, and limited intrinsic conductivity, which compromises their electrochemical performance.[31] Still, their tunable structure allows these issues to be addressed through chemical modification.[29] Depending on their redox, they can be categorized into three different groups: p-type, n-type, and b-type (**Figure 1.2**).[33] P-type compounds can form a positively charged cation upon oxidation, whereas n-type organic materials render negatively charged ions during reduction. As for the b-type materials, these combine p- and n-types redox, generating positive and negative ions.[32–34]

Among organic cathode materials (*e.g.,* imines, nitroxide radicals), in recent years, carbonyl compounds and conducting polymers have attracted attention due to their promising characteristics and ease of modification, making them suitable materials for ion storage. Therefore, the following subchapters intend to explain their general properties, ion storage mechanisms, and current strategies to improve their performance.

Table 1.2 – Advantages and challenges of the main categories of organic cathode materials for SIBs.[32]

Type	Advantages	Challenges
Conducting Polymers	Good conductivity.	Low capacities. Sloped discharge plateau.
Carbonyl Compounds	High capacity. Fast reaction kinetics.	Low electronic conductivity. High solubility.
"Organic Radicals"	Fast kinetics. Flat plateau.	Low electrochemical efficiency. Low capacity and conductivity. High solubility
Organosulfur Compounds	High Capacity.	Low reaction kinetics and conductivity. High solubility.

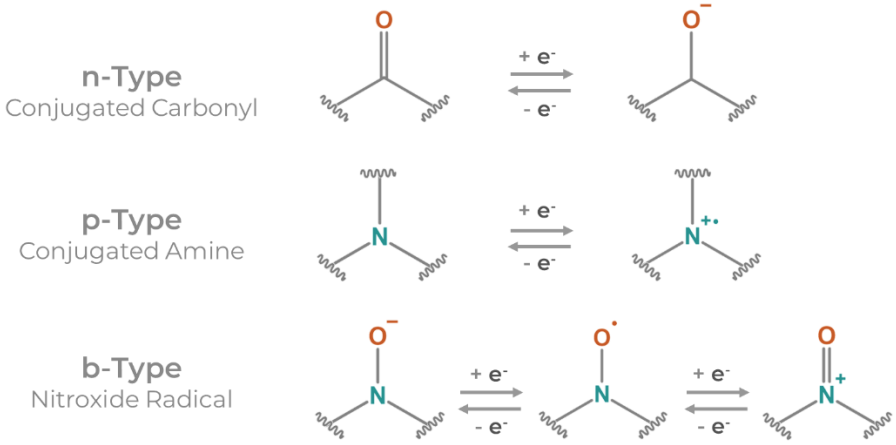

Figure 1.2 – Examples of p-type, n-type, and b-type organic cathode materials.

1.2.1 Carbonyl Compounds

As their name suggests, the most used carbonyl-based compounds for ion batteries contain two carbonyl groups that can be adjacent to each other – or not – in an unsaturated six-member ring structure.[35] They act as cathodes when the carbonyl groups suffer a reduction, giving place to negatively charged oxygen anions that coordinate guest cations (**Figure 1.3**). This class of organic compounds presents the highest theoretical capacities, being 1,4-benzoquinone (BQ) the simplest member of the quinone family with a theoretical specific capacity of 496 mAh g^{-1} at a redox potential of 2.8 V *vs.* Li/Li^+.[35] As represented in **Figure 1.3**,[36] due to the inverse relation of molar mass with the theoretical specific capacity, a progressive decrease in specific capacity is observed upon the modification of the basic BQ unit.[33]

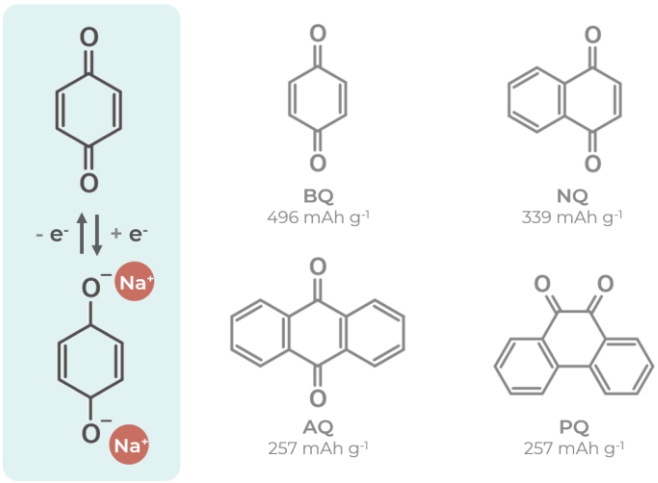

Figure 1.3 – Generalized ion exchange mechanism of carbonyl-based compounds for ion batteries and examples of the most reported materials: benzoquinone (BQ), naphthoquinone (NQ), anthraquinone (AQ) and phenanthrenequinone (PQ).

Current cathode design for carbonyl compounds addresses their major drawbacks. To improve low redox potential, molecules are modified with electron-withdrawing or electrodonating groups.[33] As for their stability, it can be improved with higher ordered structures, which increases their molecular weight and decreases their solubility. Examples of this are supramolecular polymeric/oligomeric structures or preparing oligomeric salts in polymeric form like, for instance, developing macrocyclic calixarenes with a cyclic array of *p*-quinones.[37] Regarding their conductivity, introducing conductive units like carbon coatings/nanostructures and polymeric binders with conducting additives are the most common approaches, which also help improve the stability of the material.[33,37]

Despite the improvements, they also introduce new challenges. For example, synthesis methods often require multistep processes. Additionally, large amounts of additives lower the specific capacity due to its increased weight and inaccessible active sites, while the deposition method influences the performance of the material. Moreover, these approaches remain poorly understood, leaving a great space for improvement.[33]

1.2.2 Conducting Polymers

For the most part, conventional polymers like plastics and rubbers have long been regarded as insulating materials.[38] However, the unexpected discovery of conductive polyacetylene in the 1970s permanently changed our understanding of these materials, introducing a new class known as conducting polymers.[39] Their low cost, lightweight, and mechanical flexibility, combined with their optoelectronic properties resembling those of inorganic semiconductors, soon caught interest across multiple research areas.[40] These distinctive properties are attributed to their electronic structure, constituted by alternating single (σ) and double bonds (π), as exemplified in the simple structure of polyacetylene in **Figure 1.4.**[41] Upon doping through chemical or electrochemical oxidation, these polymers enable electron transport by electron hopping.[39]

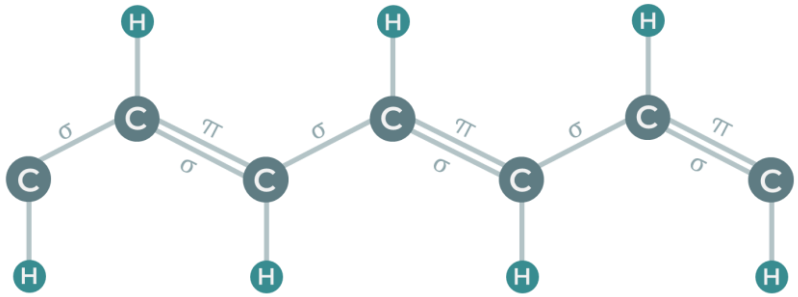

Figure 1.4 – Representation of the π conjugated polyacetylene system (Adapted from ref 41).

If one considers a pure, undoped conducting polymer, it will behave as an electronic insulator. The incorporation of donor or acceptor substituents within the polymer matrix is what significantly increases the conductivity of the material.[38] Analogous to inorganic semiconductor doping, n-doping and p-doping imply the addition or removal of charge carriers.[38,42] While n-doping adds an electron to increase the concentration of charge carriers, p-doping removes an electron. Nevertheless, the instability of organic anions (the negatively charged polymer itself) during the n-doping process diminished their interest, shifting towards the study of p-doped polymers, which facilitate electron hopping along the conjugated backbone.[38] Dopants can be incorporated into the conducting polymer during synthesis or by subsequent chemical or electrochemical processes. In this regard, because of several constraints, achieving a 1:1 doping level (ratio of charged dopant to charged monomeric unit) is rarely possible, meaning that this process is far from uniform.[42]

In all materials, the overlap of molecular electronic states generates electronic bands. The Highest Occupied Molecular Orbital (HOMO) constitutes the valence band (VB), while the Lowest Unoccupied Molecular Orbital (LUMO) corresponds to the conduction band (CB).[42,43] As such, the energy required to promote an electron from the VB to the CB, known as the energy band gap (E_g), is what determines the intrinsic properties of materials. In a polymer, the interaction between polymeric units and their neighbors also forms electronic bands.[43]

When a conducting polymer is in its undoped state, it is nonconducting and thus presents the conventional VB and CB (**Figure 1.5a**). The removal of an electron from the conjugated polymeric chain forms a polaron, originating an energetically favored deformation on the polymer backbone whose

relaxation gives rise to two localized electronic levels within the band gap (**Figure 1.5b**). After this, if a second electron is removed, an even more energetically favored deformation is observed, giving place to a bipolaron (**Figure 1.5c**). The continuous oxidation of the polymers eventually leads to an overlap between bipolaron states, forming two narrow bipolaronic bands (**Figure 1.5d**). Thus, the process from low doping to high doping is responsible for the great decrease in band gap, facilitating electron transitions that give place to the conducting character of these materials.[41,43]

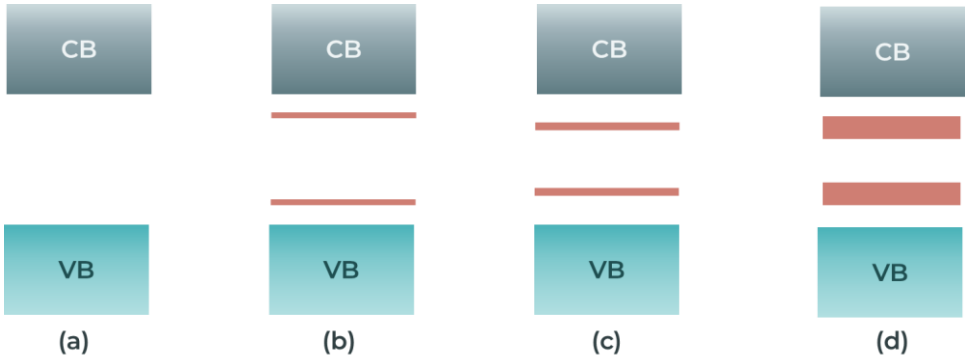

Figure 1.5 – Representation of the valence bands of a conducting polymer with increasing doping level where (a) corresponds to its nonconducting state, (b) polaronic state, (c) bipolaronic state, and (d) heavily doping levels (Adapted from ref 43).

Conducting polymers can be synthesized chemically or electrochemically, where electrosynthesis is often preferred for its simplicity, shorter times, and controlled morphologies.[39,42] In this method, applying a potential oxidizes and activates the monomer, triggering polymerization. The process follows addition polymerization via radical-radical coupling, where activated monomers form oligomers that further react to create the conducting polymer.[42]

In an ion battery, conducting polymers act as cathodes in their p-doped state, exchanging ions with the electrolyte during cycling, having theoretical specific capacities comparable to inorganic materials. However, doping levels limits their performance, with experimental capacities of 80 - 150 mAh g^{-1}.[36] Common polymers studied include polypyrrole (PPy), polyaniline (PANI), and poly(3,4-ethylenedioxythiophene) (PEDOT).[44] Among conducting polymers, PEDOT stands out due to its high stability, relatively high conductivity, and electrochemical reversibility.[45] These properties motivated its study in energy storage and conversion, functional coatings, sensors, and organic field effect transistors.[46]

PEDOT is a polythiophene derivative directly synthesized from 3,4-ethylenedioxythiophene (EDOT), which has low solubility in aqueous solutions.[38] To address this limitation, EDOT can be dispersed with a surfactant before polymerization.[47] The surfactant must be a polyanion with a long carbon chain, with poly(sodium 4-styrenesulfonate) (NaPSS) being the most commonly used (**Figure 1.6**), although other surfactants have also been considered for its synthesis.[45] These polyanionic surfactants can be immobilized within the polymer matrix during synthesis to act as counterions, enabling pseudocationic doping. This will involve cation exchange during the redox conversion of the film, where cations are expelled during oxidation and incorporated during reduction (**Figure 1.6**). To date, this polymer has been mainly reported with two surfactants: PSS and Dextran Sulfate.[45,47]

Although recent studies consider PEDOT's conductivity and stability as beneficial features for ion batteries, its intrinsic ability to incorporate ions within its matrix tends to be overlooked. Current battery applications with lithium and zinc ions often use PEDOT to coat inorganic materials[48–52] or to serve as interlayers[53–55] to enhance their electron transfer and structural stability.

Therefore, it is important to find a binding point between other sodium-withdrawing compounds and polymeric materials, implying their further optimization to be applied in ion batteries. As mentioned, organic materials are still in their infancy, but their inherent structural tunability offers great promise. The chemical compatibility of carbonyl-based compounds and conducting polymers opens possibilities to overcome limitations by combining these two materials. As such, the following chapter will approach recent studies focused on their integration.

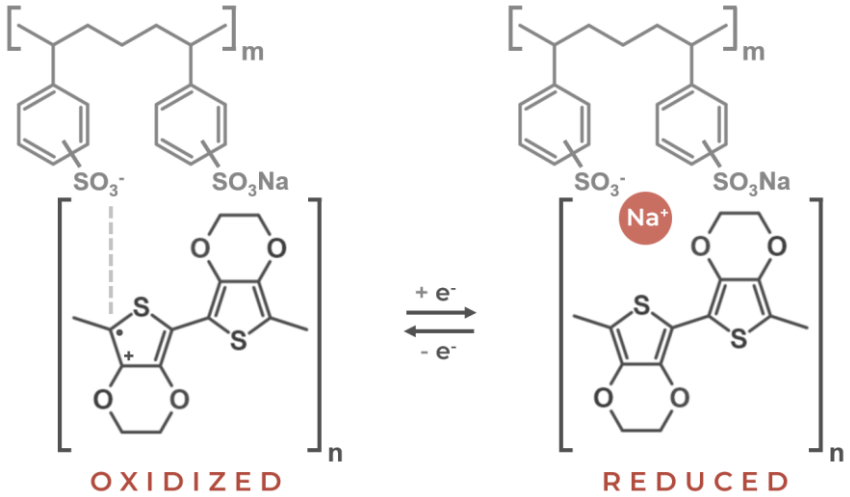

Figure 1.6 – Simplified chemical structure of PEDOT:PSS films and its ion incorporation mechanism.

1.3 Hybrid Carbonyl and PEDOT Polymers as Cathode Materials

Considering the limitations of carbonyl compounds and conducting polymers, it is evident that their shortcomings complement. Instead of using carbon and chemical additives, which compromise battery performance, carbonyl compounds can be immobilized within conducting polymer matrices. In this configuration, the conducting polymer enhances electronic conductivity and contributes to ion storage.[56] Conversely, the limited ion incorporation capacity of conducting polymers can be improved by introducing redox-active carbonyl compounds, enhancing their overall electrochemical activity.[57] Knowing the relevance of PEDOT, all the recent methods to design cathode materials that incorporate carbonyl compounds into this material are summarized in the following discussion and **Table A1** (Appendix A).

One of the most reported strategies is to electrosynthesize conducting redox polymers. These materials were first introduced by Sjödin's group[56,58–60] and consist of covalently binding a redox pendant group to the conductive polymer backbone. The first step is the chemical modification of the *β*-carbon in EDOT with the redox pendant group. With this monomeric unit, the polymer is synthesized potentiodynamically under the desired conditions (**Figure 1.7a**). This method renders experimental specific capacities of approximately 40 mAh g^{-1}.[56,58–60] Another approach is to electrochemically synthesize the polymeric material in a mixture of EDOT and modified monomers.[61]

Recent studies on conducting redox polymers use post-deposition polymerization, starting with a PEDOT trimer modified with a redox pendant group. The trimer is dissolved in a volatile solvent, deposited on the electrode, and dried. The dry film is then exposed to electrolyte and polymerized potentiostatically (**Figure 1.7b**), yielding materials with specific capacities of 60 to 81 mAh g^{-1}.[62–66]

Another method to obtain hybrid carbonyl/PEDOT polymers is by immobilizing modified sulfonated dopants (**Figure 1.7c**). This starts by chemically modifying the dopant with catechol groups,

followed by electrochemical PEDOT synthesis incorporating these polyanions. Modified polyanions include poly(4-vinylcatechol-r-styrenesulfonic acid), sulfonated poly(3,4-dihydroxystyrene), and sulfonated poly(vinylcatechol).[67–69] Specific capacities range from 52 to 95 mAh g^{-1}. Large quinones like anthraquinone can also be sulfonated and used as dopants in PEDOT synthesis.[70]

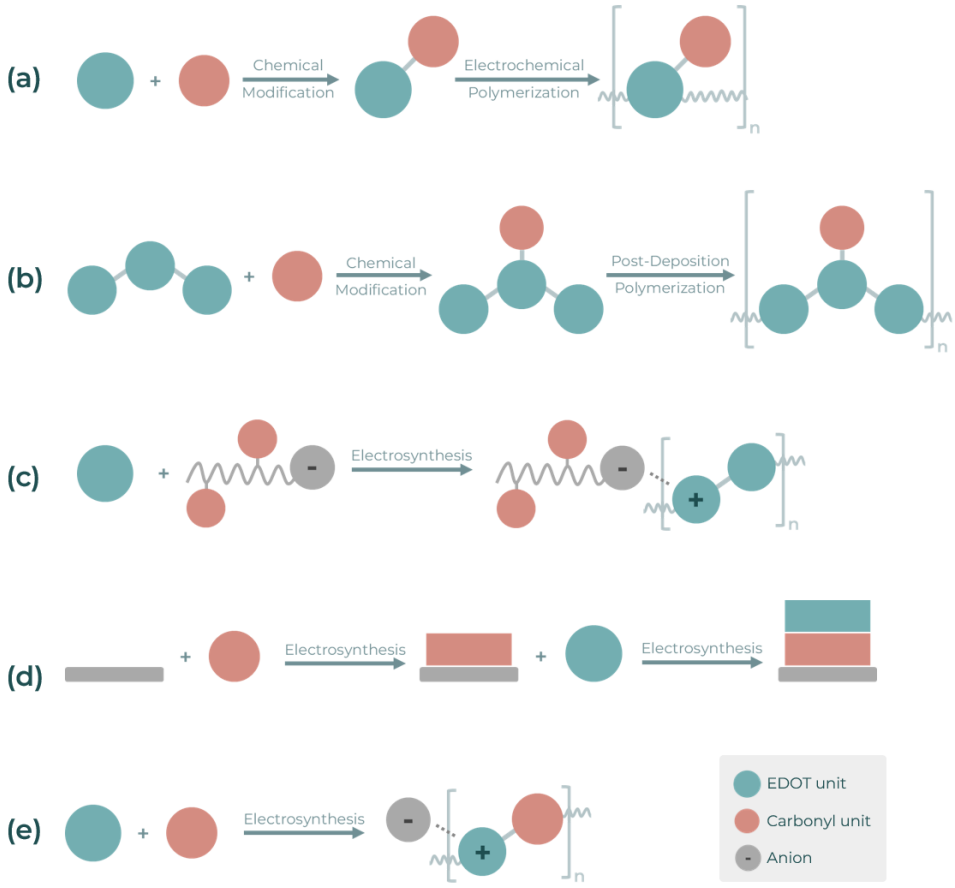

Figure 1.7 – Representation of the most common strategies to synthesize hybrid carbonyl and PEDOT-based materials.

The layered galvanostatic deposition of poly(aminoanthraquinone) (PAAQ) and PEDOT involves depositing one polymer layer, followed by electrosynthesis of the second layer (**Figure 1.7d**).[71,72] The PAAQ/PEDOT composite shows a specific capacity of 106 mAh g^{-1}. Alternatively, two materials can be combined by potentiostatic copolymerization (**Figure 1.7e**). This method has been used for polyhydroquinone (PHQ) and PEDOT copolymers, which present a theoretical specific capacity of 112 mAh g^{-1}.[73]

Less conventional methods include chemical synthesis of hybrid materials. One involves a two-step oxidative polymerization where poly(1-amino-5-chloroanthraquinone) nanoparticles are coated with PEDOT, achieving 198 mAh g^{-1}.[57] Another study used slurry casting to incorporate dibenzo[b,i]thianthrene tetraone into PEDOT, reaching 220 mAh g^{-1}.[74] Sustainable materials like lignin have also been integrated via oxidative polymerization, with a capacity of 159 mAh g^{-1}.[75]

1.3.1 Polydopamine and PEDOT-Based Copolymers for Energy Storage

Although carbonyl/PEDOT hybrid cathodes show good capacities, integrating species that enhance sodium ion uptake is a key to surpassing lithium-ion batteries. Using easy-to-modify organic materials with diverse chemical affinities is essential. Polydopamine (PDA) stands out as a versatile material and has been previously regarded as a cathode host.[76,77] Given its potential, the following section will describe the chemistry of PDA and its great advantages for rechargeable battery design.

1.3.1.1 PDA as a Bridge to Higher Stability and Capacities

Initial studies on the wet-adhesive properties of mussel proteins drove the development of a unique polymeric coating known as polydopamine in 2007.[76] This biomimetic polymer presents a wide chemical versatility whose adhesive properties, later explained and represented in **Figure 1.8**, made it the first material-independent surface chemistry, meaning that it can deposit on any substrate, regardless of its properties.[78,79] The simplicity, adaptability, and low cost of this method rapidly led to its application in biomedicine, catalysis, nanotechnology, and, energy conversion.[76–78,80]

These advantageous characteristics of PDA not only come from its interesting chemical nature, but also from its surprisingly simple synthesis. The most widely used method consists of simply dip coating the desired substrate into a slightly alkaline aqueous dopamine solution (pH ≥ 7.4) in the presence of oxygen to trigger a chemical oxidative polymerization.[78,80] Although the details on polymerization are an active subject of discussion, it has been considered that this process is initiated by the spontaneous oxidation of dopamine monomers (driven by oxygen) followed by its self-polymerization.[79] Despite the versatility of this method, it has low efficiency, selectivity, and uniformity.[78]

As an alternative synthesis method, the electrochemical polymerization of PDA has gathered attention in recent years, allowing faster deposition times with higher morphology control and selectivity. However, this method is limited to the use of conductive or semiconductive substrates.[80] Until now, it has been considered that the electrosynthesis of PDA is initiated by the electrochemical oxidation of dopamine monomers, followed by chemical additions accompanied by monomer cycling and isomerization that give place to the deposition of PDA over the electrode surface.[78]

Understanding the resulting structure of PDA, regardless of the synthesis method, remains a significant challenge due to the material's inherent chemical diversity and structural heterogeneity.[79] Various structural studies suggest that PDA consists of a complex network of alternating uncyclized dopamine units and cyclized indole-type structures, interconnected through covalent bonds and stabilized by intermolecular interactions.[81] Despite this complexity, its distinctive chemical behavior is largely attributed to the unique combination of amine and catechol functional groups.[76,82]

When dopamine units are in their reduced state, the catechol moiety can chelate metal ions and is prone to oxidize to quinone. The primary amine and β-carbon also act as nucleophilic sites, enabling reactions such as Schiff base formation and Michael addition, respectively.[79] Upon oxidation, quinones become electrophilic and can react with nucleophiles like amines and thiols. Besides allowing covalent bonding, dopamine units can stablish intermolecular interactions like hydrogen bonding and π–π stacking through its hydroxyl groups and aromatic ring.[83] All these observations, which highlight the chemical versatility of PDA, are summarized in **Figure 1.8**.[84]

The chemical diversity of this material makes it valuable for many applications, especially energy conversion. Its ionic incorporation involves coordinating sodium ions, for instance, with the reduced form rather than introducing protons. Strong interactions with electrode surfaces improve stability by adjusting to the significant volume changes during cycling while enabling increased capacities. It also offers better biocompatibility and lower cytotoxicity than other quinones.[77] It is currently used as coating on nanostructured materials, porous layers on Prussian blue cathodes, and as active electrode/binder.[85,86]

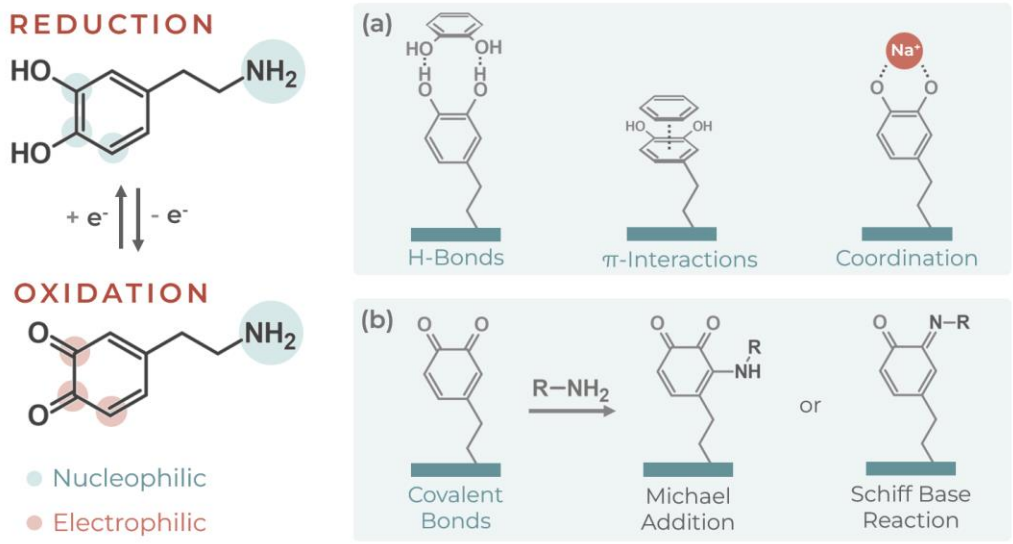

Figure 1.8 – Reactivity of dopamine units and its possible (a) intermolecular interactions and (b) covalent modifications.

1.3.2 Hybrid PDA/PEDOT Materials

Although with the previous description one can idealize PDA as an optimal material for its use in a wide variety of applications, like carbonyl compounds, this material suffers from low conductivity. This limits its application in areas that rely on electron transfer, such as energy conversion and electrochemical biosensors, as evidenced by the inhibition of charge transfer in films with thicknesses of *ca.* 20 nm.[87]

Therefore, considering the same motivation behind the development of carbonyl and PEDOT hybrid materials, along with the promising properties of PDA, this work will focus on the electrocopolymerization of these two materials as a cathode for sodium-ion batteries. The powerful combination of PEDOT and PDA has already been explored in the literature for neural electrode applications,[88–90] enhancement of PEDOT's work function in solar cells,[91,92] flexible optoelectronic devices,[93] mechanical sensors for human monitoring,[94] and supercapacitors for energy storage.[95,96] Their synthesis methods and processing strategies are briefly summarized in **Table A2** (Appendix A). It is important to highlight that the combination of PDA with other conducting polymers, such as PPy[97–107] and PANI,[108–113] has already been reported in the literature, revealing interesting synergistic behaviors.

Among PDA/PEDOT hybrid materials, electrocopolymerization has already been reported, yet this method has been scarcely optimized and understood. Kim *et al.*[88] potentiostatically synthesized at 1 V *vs.* Ag/AgCl for 10 minutes, what they referred to as a polydopamine-doped conductive polymer in Sodium Phosphate Buffer (SPB). In their study, morphology changes during deposition were monitored using Scanning Electron Microscopy (SEM), revealing that the material gradually formed a denser porous structure over time. Energy-Dispersive X-Ray Spectroscopy (EDS) confirmed an increasing content of PEDOT relative to PDA throughout the electrodeposition. Additionally, impedance spectroscopy showed a progressive increase in film resistance with longer synthesis times. The polymeric films were characterized only in ferricyanide, showing no PDA redox activity and an increasing pseudocapacity with synthesis time. This hybrid material was later successfully applied in neuronal signal recording and electrical stimulation.

Another electrosynthesized material was also reported for neural electrode applications for brain-machine interfaces by Huang *et al.*[90] In their work, they potentiodynamically deposited what they refer to as a PEDOT/PDAM material from an aqueous DA and EDOT solution, at 50 °C for 500 cycles at 200 mV s^{-1}, sweeping from −1 V to 1 V *vs*. Ag/AgCl. The formation of a new material was confirmed using Ultraviolet-visible (UV-vis), X-Ray Photoelectron Spectroscopy (XPS), SEM, Atomic Force Microscopy (AFM), impedance spectroscopy, and cyclic voltammetry. The voltammetric characterization revealed the presence of PDA, although with a low pseudocapacitive response from the PEDOT component.

Despite the previously reported hybrid materials exhibiting adequate behavior for their intended applications, their synthesis methods are not ideally suited when considering the typical conditions required for PEDOT and PDA formation. In particular, the electrosynthesis methods described in the literature do not employ anionic surfactants, which are fundamental to dissolve EDOT monomers in aqueous media and, more importantly, to provide the required pseudocationic character to the polymer that allows it to function as a cathode in metal-ion batteries. Furthermore, all reported syntheses involve either long deposition times or multi-step procedures, making them less practical. Thus, the present work will not only explore the first application of PDA/PEDOT hybrid materials as cathodes for sodium-ion batteries but also introduce a novel and simplified electrosynthesis as an improved method for their efficient preparation.

1.4 Objectives

The use of solid-state materials as hosts for ion storage is unsuitable for big ions, whose dimensions lead to a structure collapse that compromises the performance of ion-based batteries.[8] Therefore, the flexibility and ease of modification of polymeric materials poses the possibility of storing large ionic structures with promising performances. As such, the main objective of this work is to *explore the complementary properties of conducting and carbonyl copolymers, with appended quinone/catechol moieties, and evaluate their efficiency as hosts for sodium in ion batteries.* To implement this idea, the following objectives were defined:

1. Electrosynthesize functional copolymers based on EDOT and DA and optimize their physicochemical properties for their application as cathode materials in sodium-ion batteries.
2. Perform extensive characterization of the copolymer films using cyclic voltammetry, Electrochemical Quartz Crystal Microbalance (EQCM), AFM, ellipsometry, water contact angle goniometry, and spectroscopic optical techniques to evaluate and compare their physicochemical features (*e.g.*, electroactivity, morphology, thickness, optoelectronic properties, chemical composition) against pristine PEDOT and PDA.
3. Evaluate the stability of the copolymer films through galvanostatic and potentiostatic half-cell cycling in graphite electrodes.

Chapter 2

Characterization Techniques and Experimental Details

"*... if we conceive of a being whose faculties are so sharpened that he can follow every molecule in its course, such a being, whose attributes are as essentially finite as our own, would be able to do what is impossible to us*."

James Clerk Maxwell

2. Characterization Techniques and Experimental Details

2.1 Physicochemical Characterization Techniques

To design new polymeric cathode materials, it is crucial to assess their properties and performance with respect to the intended goals. Thus, the following subchapter summarizes the main techniques and principles considered throughout this work. Electrochemical, gravimetric, microscopic and spectroscopic methods were fundamental to characterize the physicochemical properties of the synthesized materials and assess their potential as cathodes for SIBs.

2.1.1 Electrochemical Systems and Methods

Electrochemistry is born at the interface, where two different states of matter meet. Introducing an electronic conductor into an electrolytic solution creates a compromise between both states, leading to charge separation and the formation of the *electrical double layer*. At this boundary, the formation and exchange of charge at the interface occurs, being the core of electrochemical processes.[114]

The electrode potential dictates the direction and rate of these reactions, making its precise measurement and control essential. One can control the potential of an electrode by using an external source of electrons, such as a potentiostat. Applying a negative potential raises the energy of the electrode's electrons, transferring them into vacant electronic states on the species in the electrolyte and originating *reduction currents.* Conversely, applying a positive potential lowers the electrode's energy so that electrons are transferred from the electrolyte species to the electrode and generate a flow of electrons that correspond to *oxidation currents*.[115] This process is schematically shown in **Figure 2.1**.

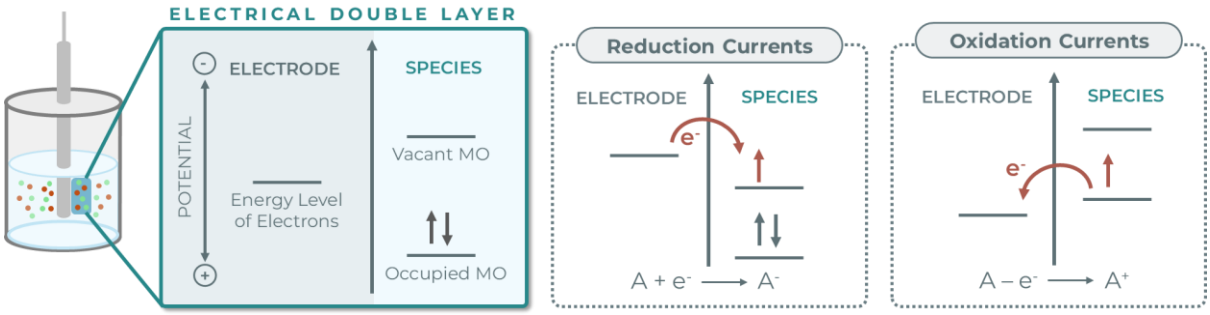

Figure 2.1 – Schematical representation of reduction and oxidation of A species in solution, with their corresponding Molecular Orbitals (MO).

In general, when one studies a desired chemical phenomenon, the system is intentionally perturbed, and its response is measured and interpreted. In electrochemistry, this may involve applying a potential overtime and recording how the current feedback changes. This can be performed by using different potential waveforms, such as potentiodynamic profiles and potentiostatic pulses, which will be discussed next.[115]

2.1.1.1 Cyclic Voltammetry

In the case of Cyclic Voltammetry (CV), a triangular potential waveform is applied. As represented in **Figure 2.2a**, we sweep from an initial known potential (E_i) to a second selected potential (E_λ) and switch back to a final potential E_f at a constant sweep rate (v). The potential varies linearly with time, resulting in a triangular waveform that follows the relation $E = E_i + vt$, where E corresponds to the electrode potential.[115]

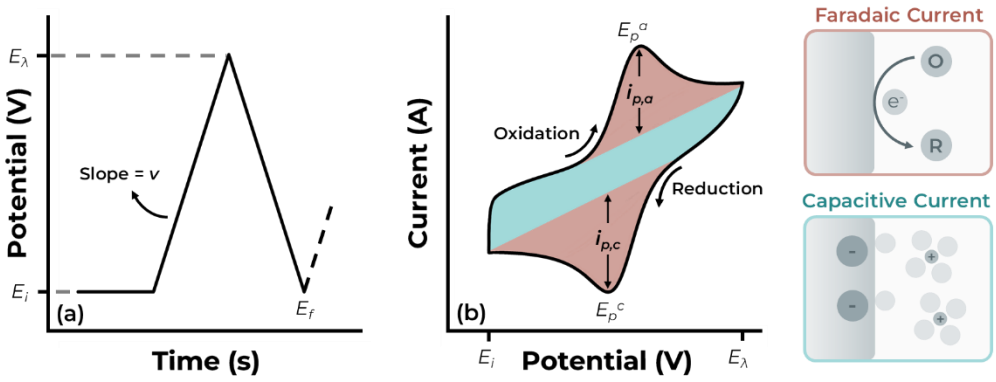

Figure 2.2 – (a) Potential pulse in cyclic voltammetry and (b) cyclic voltammogram of a reversible charge transfer.

As the potential is swept, a concentration gradient forms at the interface, generating flux of oxidation and reduction currents. When a certain potential promotes a charge-transfer reaction across the metal-solution interface, a faradaic current (I_f) is observed. Additionally, capacitive currents (I_c) can be recorded, arising from other processes at the double layer where charge does not cross the interface, such as adsorption or desorption. Therefore, the total current will correspond to the sum of the faradaic and capacitive currents ($I = I_c + I_f$), originating cyclic voltammograms (**Figure 2.2b**).[115–117]

These voltammetric responses give insights about redox reactions and other phenomena occurring at the interface, providing valuable qualitative and quantitative information about electrochemical, thermodynamic and kinetic parameters.[118] In the case of reversible processes (**Figure 2.2b**), one observes oxidation and reduction peaks with equal intensity. These peaks correspond to anodic and cathodic peak currents (i_p^a;i_p^c) and potentials (E_p^a;E_p^c), respectively. From this information, the redox conversion can be evaluated thermodynamically using the formal potential ($E^{0'}$) which is the average of the peak potentials ($E^{0'} \approx E^{1/2} = (E_p^a + E_p^c)/2$).[117]

The use of different scan rates during cyclic voltammetry makes it possible to assess whether a redox reaction is controlled by diffusion or by charge transfer. For instance, if the peak current is linearly related to the square root of the scan rate ($v^{1/2}$), the process is diffusion-controlled. On the other hand, if the peak current is linearly related to the scan rate (v), the process is controlled by charge transfer, resulting in a voltammetric and linear response as shown in **Figure 2.3** and predicted by the Randles–Ševčik equation (**Equation 2.1** for 25 ºC). In this case, the species are either adsorbed or very close to the electrode surface, and knowing the number of electrons involved in the redox reaction allows to estimate the surface coverage using **Equation 2.2** (for 25 ºC).[117]

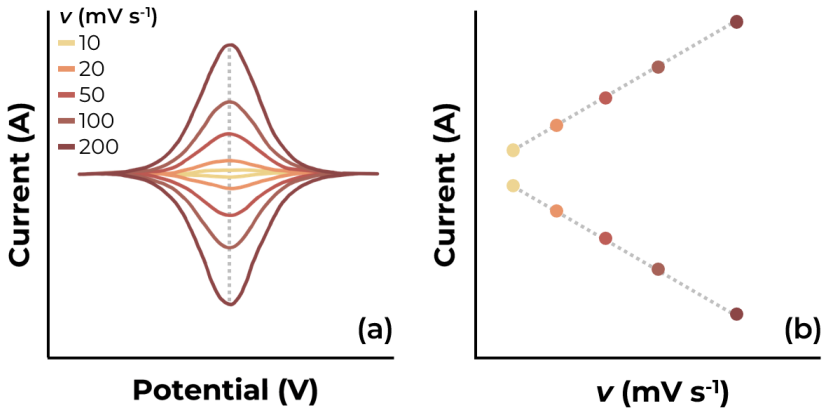

Figure 2.3 – Reversible cyclic voltammogram of redox reaction controlled by charge-transfer at (a) different sweep rates and (b) its relationship with the sweep rate when these are adsorbed to the electrode.

$j_p = -2.69\times10^5\ n^{3/2}\ D^{1/2}\ v^{1/2}\ C^*$	j_p – Current peak density (A cm^{-2}) n – Transferred number of electrons D – Diffusion coefficient (cm^2 s^{-1}) v – Sweep rate (mV s^{-1}) C^* – Bulk concentration of electroactive specie (mol cm^{-3})	**(2.1)**
$j = 232.09\ n^2\ \Gamma\ v$	j – Current density (A cm^{-2}) Γ – Surface coverage (mol cm^{-2})	**(2.2)**

Besides reversible redox reactions, other behaviors can be observed and studied with cyclic voltammetry, such as *quasi-reversible* and *irreversible* systems, as exemplified in **Figure 2.4** for soluble electroactive species. These can be distinguished empirically with the peak current ratio ($|i_p^a/i_p^c|$), their dependence on peak potential, the sweep rate and through their potential peak separation.[116]

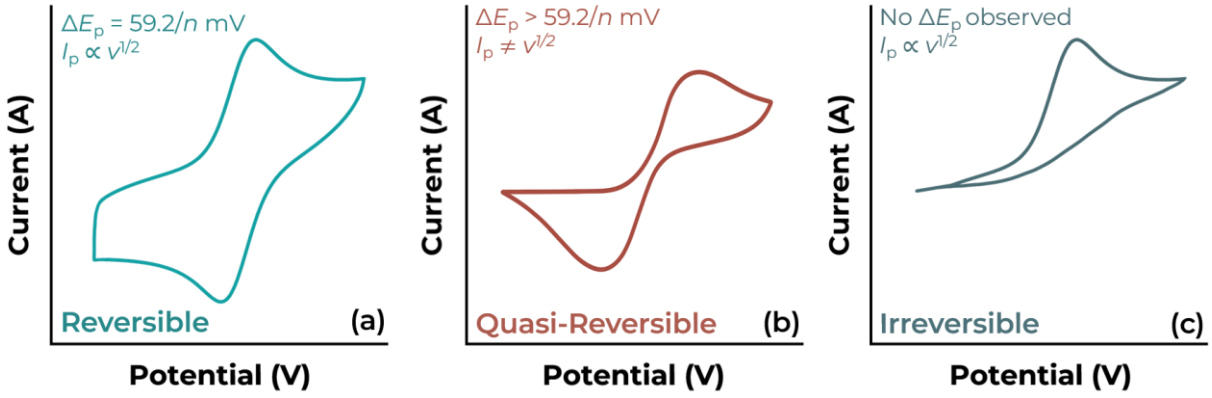

Figure 2.4 – Cyclic voltammograms observed for (a) reversible, (b) quasi-reversible and (c) irreversible electrochemical systems with their respective diagnostic empirical criteria.

2.1.1.2 Chronoamperometry

In chronoamperometry, a constant potential pulse is applied to the working electrode while the change in current is recorded over time.[119] The selected pulse (**Figure 2.5a**) starts from an initial potential (E_1) to prevent unwanted reactions and is followed by a second pulse (E_2) that drives the desired reduction or oxidation reaction. This potential step provokes an immediate perturbation on the electrochemical system, inducing a concentration gradient where the reaction rate is controlled by diffusion, generating a current response as the one observed in **Figure 2.5b,** following the behavior foreseen by the Cottrell equation (**Equation 2.3**) for planar electrodes.[115,116]

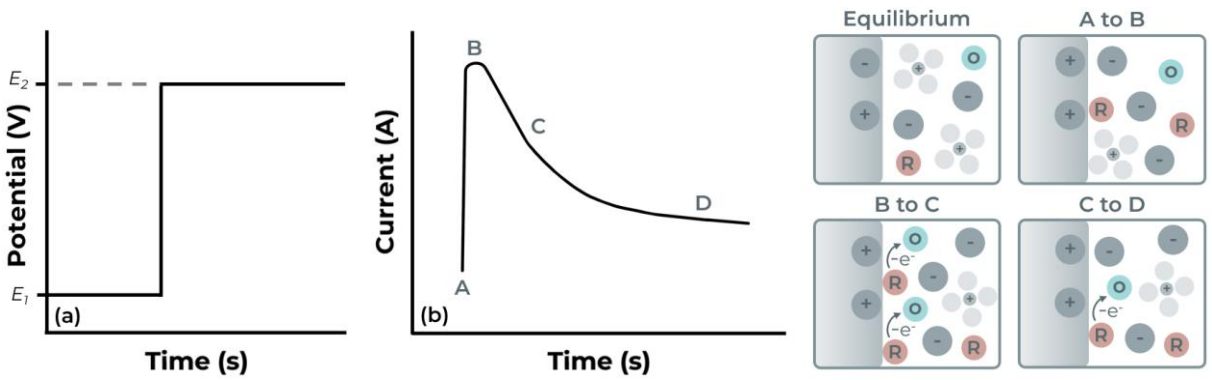

Figure 2.5 – (a) Potential pulse applied during chronoamperometry and (b) response of the system to the pulse.

$$i = -\frac{nFAC^{*}D_0^{1/2}}{\pi^{1/2}\,t^{1/2}} \quad \textbf{(2.3)}$$

i – Current (A)
F – Faraday's constant (96485 C mol^{-1})
A – Electrode area (cm^2)
D_0 – Diffusion coefficient for electroactive specie ($cm^2\ s^{-1}$)
t – Time (s)

Initially, from point A to B, a peak current is observed. This current is used to charge the double layer up to the applied potential E_2. After this current maximum, as described by the Cottrell equation, a drastic current decay proportional to $t^{-1/2}$ is recorded from point B to C. During this phase, the current not only continues to charge the double layer but also begins to drive electron transfer across the interface. This latter process faces greater resistance, making it slower than the initial capacitive charging. Finally, from C to D, the current stabilizes, indicating that all electrons are being used for redox reactions rather than charging the double layer.[118,119]

2.1.1.3 Chronopotentiometry

Contrary to chronoamperometry, chronopotentiometry consists of applying a constant current to an electrode for a defined time while recording the resulting change in potential (**Figure 2.6a**). This means that the reaction rate at the electrode is fixed, allowing the study how the potential varies with time. As represented in **Figure 2.6b**, the applied current is first used to charge the double layer and then to drive the faradaic reactions.[116,120]

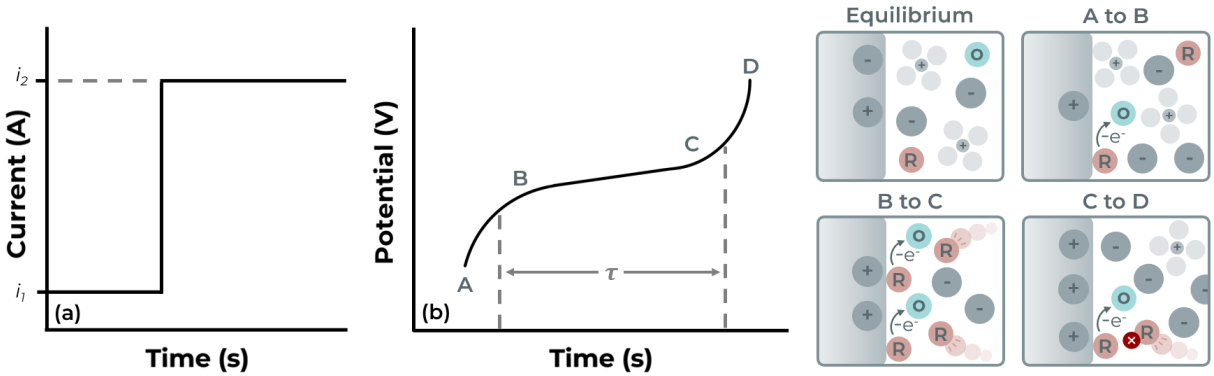

Figure 2.6 – (a) Potential pulse applied during chronopotentiometry and (b) response of the system to the pulse.

When a simple reaction of the type $R \rightleftharpoons O + ne^-$ is considered and a current pulse is applied, a sharp increase in potential is observed from A to B, corresponding to two processes. The first, dominant at shorter times, is the charging of the double layer. The second, dominant at longer times, corresponds to the charge transfer of electrons across the double layer. This transient continues until the potential required to oxidize R to O is reached. From B to C, the potential increases more slowly, controlled by the Nernst equation, until the surface concentration of R is nearly zero. From C to D, the flux of R is no longer sufficient to sustain the applied current, causing the electrode potential to rise sharply again until another electrode process occurs.[119,120]

Mathematically, this process can be described by the Sand equation (**Equation 2.4**), where τ corresponds to the transition time, as represented in **Figure 2.6b**. By considering the boundary conditions and combining the Sand equation with the Nernst equation, **Equation 2.5** is obtained. In this expression, $E_{\tau/4}$ corresponds to the quarter-wave potential, since $E=E^o$ when $t = \tau/4$ for $D_o = D_R$.[116,120]

$$|j\,\tau^{1/2}| = -\frac{nF\,D_R^{1/2}\pi^{1/2}C^*}{2}$$

τ – Transition time (s)
C^* – Bulk concentration of electroactive specie (mol cm^{-3})
D_R – Diffusion coefficient for reduced species (cm^2 s^{-1})

(2.4)

$$E_{\tau/4} = E^o + \frac{RT}{nF} ln\left(\frac{D_O}{D_R}\right)^{1/2}$$

$E_{\tau/4}$ – Quarter wave potential (V)
E^o – Standard electrode potential (V)
R – Gas constant (8.314 J mol^{-1} K^{-1})
T – Temperature (K)
D_O, D_R – Diffusion coefficient for oxidized and reduced species (cm^2 s^{-1})

(2.5)

2.1.2 Electrochemical Quartz Crystal Microbalance (EQCM)

Although voltammetric techniques are extremely versatile and powerful on their own, they are often silent to certain fluxes of solvent and other species existing at the electrode/electrolyte interface.[121,122] These fluxes of solvent/species can result in mass variations on the electrode surface, which become measurable when electrochemical methods are coupled with Quartz Crystal Microbalance (QCM). The core principle of QCM relies on the change in resonant frequency of an oscillating system, which are proportional to mass variations.[123] This oscillations are detected using piezoelectric materials that deform under an applied electric field, being quartz the most widely used. When a quartz crystal is sandwiched between two electrodes, an electric field applied perpendicularly to the crystal induces a slight mechanical deformation. By switching the electric field on and off, this deformation generates mechanical oscillation (**Figure 2.7**). This oscillation depends on the orientation of the crystal, thus one specific cut is typically used, the AT-cut.[122] This cut allows parallel oscillations in the *thickness shear mode*, having a very low temperature coefficient in the room temperature range.[122,123]

The relationship between the resonance frequency of a piezo-electric quartz crystal with the mass variation was first described by Sauerbrey in 1959 for the gas phase,[123] represented in **Equation 2.6** and valid when $\Delta f \ll f_0$. Later work of Kanazawa and Bruckenstein in 1985 validated this expression for rigid films, assuming that the electrode and the deposited material move synchronously with the crystal and thus act as an extension of the quartz resonator.[121,124]

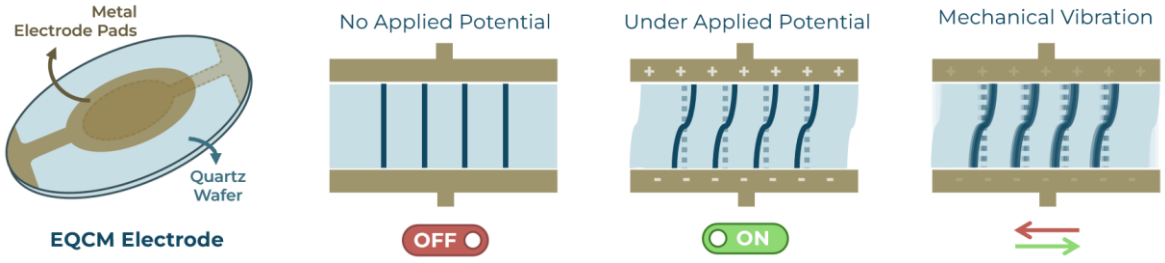

Figure 2.7 – Graphical representation of EQCM electrode and thickness shear deformation.

$$\Delta f = -\frac{2\,\Delta m\,f_0^2}{A\sqrt{\mu_q\,\rho_q}}$$

Δf – Frequency shift (Hz)
Δm – Mass change (g)
f_0 – Resonant frequency of the quartz crystal (7978181 Hz)
A – Piezoelectrically active area (cm^2)
μ_q – Shear modulus of AT-cut quartz (2.947×10^{11} dyn cm^{-2})
ρ_q – Quartz density (2.648 g cm^{-3})

(2.6)

2.1.3 Atomic Force Microscopy (AFM)

Atomic Force Microscopy is a type of Scanning Probe Microscopy (SPM) that enables high resolution and precise structural measurements of a remarkable variety of materials at the nanometer scale. Unlike conventional microscopes, AFM does not rely on focusing light or electrons, instead it renders images purely by physical interactions. One can think of AFM as sharp probe that "*feels*" the sample surface, mapping its height and surface properties.[125] This probe, mounted on a flexible cantilever, senses the surface through intermolecular forces. In the ideal case where the tip apex has a single atom, bringing the tip close to the sample triggers repulsive interactions due to the overlap of their electronic shells. However, there are additional long-range forces which are generally attractive and interact across large surface areas.[126] These short and long-range forces can be traced by reflecting a laser beam from the cantilever's apex onto a quadrant photodetector, distinguishing lateral and vertical deflections. As the sample is swept on the *x* and *y* directions, the probe continuously interacts and adjusts on the *z*-axis through a *feedback* mechanism, tracing the surface topography.[127] A schematic illustration of AFM operation is shown in **Figure 2.8a**.

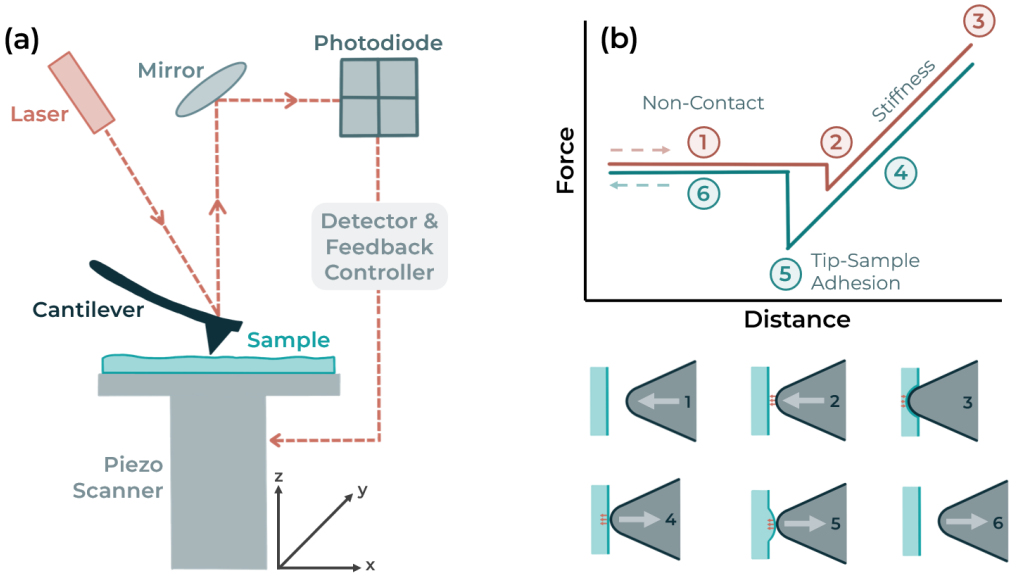

Figure 2.8 – Schematical representation of (a) AFM measurement setup and (b) force-distance adhesive curves (Adapted from ref 128 and 132).

The use of AFM evolved into numerous operational modes, carefully optimized for specific applications based on the cantilever's motion and the dominant forces during analysis. The *contact mode* relies on short-range forces, with the tip maintaining continuous physical contact with the sample during the scan. The *feedback* system keeps the cantilever at a constant deflection, ensuring that the registered force is kept constant throughout the measurement. This mode is best suited for smooth or slightly rough samples.[127]

In contrast, the *non-contact mode* is based on small oscillation amplitudes of the cantilever, keeping the tip at a slight distance from the surface so that it remains on the attractive force regime. The *feedback* system in this mode adjusts the oscillation frequency and amplitude, which is registered by the photodetector. This mode is ideal to avoid contamination and damage on the tip.[128] Finally, the *tapping mode* uses large oscillation amplitudes, allowing the tip to intermittently touch the surface and record both attractive and repulsive forces during scan. The *feedback* mechanism compares the difference between the initial applied oscillation and the recorded oscillation, measuring phase differences. This mode is ideally suited for soft or rough samples.[127]

In addition to imaging, AFM enables the measurement of a great number of different properties. For instance, as the cantilever behaves as a small spring, it is natural to measure the forces between the tip and the surface. This process can be described in the following steps and shown in **Figure 2.8b**.[125,126]

1. *Tip Above the Sample*: The tip is positioned far from the surface, experiencing zero interaction force.
2. *Approach of the Tip*: The z-piezo moves toward the sample. Initially, there are no significant forces. When the tip is close enough, attractive forces pull the cantilever downward.
3. *Contact and Repulsion*: Upon contact, the cantilever bends upwards due to repulsive forces. The deflection increases linearly with the piezo movement, following Hooke's Law.
4. *Retraction*: The piezo retracts the tip from the surface and the adhesive forces may cause the cantilever to remain bent downwards while the tip is pulled away.
5. *Tip Removal (Adhesion):* During retraction the adhesive forces are overcome, and the tip is removed from the surface. The maximum force before this removal corresponds to the adhesion force.
6. *Return Tip Above the Sample*: The cantilever goes back to its initial position, having zero interactions.

These principles can be directly applied in *Peak Force Tapping* mode, which is considered a variation of the *tapping mode*. In this case, the cantilever oscillates at low frequencies with an amplitude of 100 - 300 nm, and the *feedback* is controlled by maintaining a constant peak force during imaging. This allows the simultaneous acquisition of sample topography and additional physical properties such as adhesion and elasticity. This way, force-distance curves can be obtained with sensitivity in the order of pN, either as averages of the sample or in selected regions of interest.[128–130]

Another relevant parameter that AFM can provide is the *root mean square roughness* of a surface, obtained from the distribution of heights and valleys measured during analysis. After some mathematical treatment, automated by the AFM *software*, these values are processed into a mean squared roughness, which is simplified in **Equation 2.7**.[131,132]

$$R_q = \sqrt{\frac{\sum_{i=1}^{N}(z_i-\bar{z})^2}{N}} \qquad \begin{array}{l} R_q \text{ – Root mean square roughness of a sample} \\ N \text{ – Number of points} \\ z_i \text{ – Height of point i} \\ \bar{z} \text{ – Average Height} \end{array} \qquad \textbf{(2.7)}$$

2.1.4 Ellipsometry

Ellipsometry is a technique that allows the measurement of material's dielectric properties by analyzing the reflection of light from their surface (**Figure 2.9a**). This is possible by measuring changes in the polarization state of the light upon interaction with a surface. This is typically accomplished in reflection mode and using a linearly polarized incident beam, which becomes elliptically polarized upon reflection. The use of ellipsometry has gained growing interest due to its remarkable sensitivity to small changes in surfaces, high surface selectivity, and its ability to provide insights into film thickness, density, internal morphology, and electronic properties of thin films. Nevertheless, one of its main limitations lies in the complexity of data analysis, which is not as straightforward as other techniques.[133,134]

To comprehend the basic principles of ellipsometry, it is essential to understand how light propagates. Light can be described as an electromagnetic wave, composed of two perpendicular components: the electric field and the magnetic field. These components are commonly represented as simple sine waves, as shown in **Figure 2.9b**. According to Snell's Law (**Equation 2.8**), when an electromagnetic wave interacts with a material, its propagation is perturbed. For instance, in a transparent medium, the refractive index *n* determines the propagation of the wave (**Figure 2.9c**). As *n*

increases, propagation frequency of light increases due to its interaction with the material. However, when the film strongly absorbs light, the wave's propagation is also determined by the extinction coefficient *k*. Therefore, to account for both effects, one can define the complex refractive index *N* with **Equation 2.9**. When considering an absorbing film ($k > 0$) with a constant *n*, the amplitude of the wave should decrease progressively with increasing distance from the surface (**Figure 2.9d**). Chemists are generally more familiar with this concept through the absorption coefficient (α), which can be directly related to *k* by **Equation 2.10**.[134]

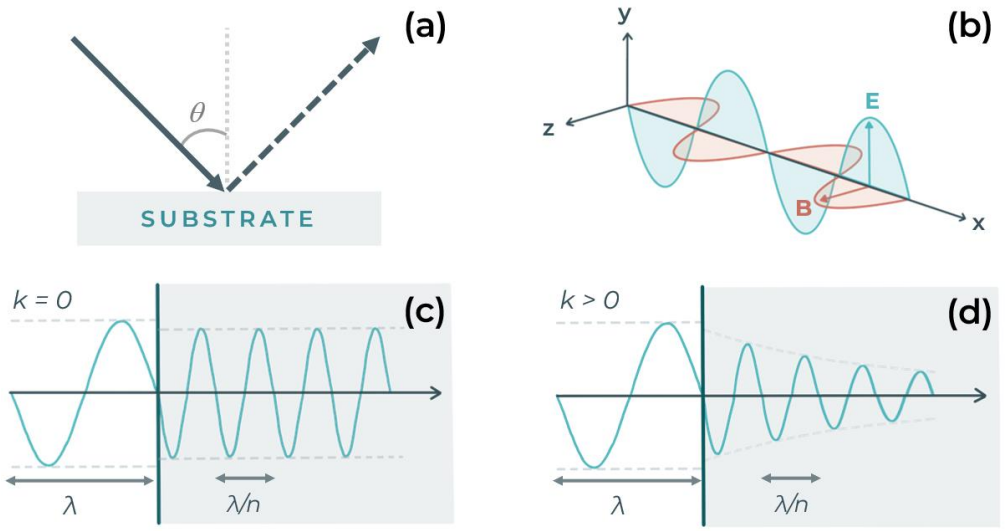

Figure 2.9 – Schematical representation of (a) reflection upon a 2-phase system, (b) propagation of an electromagnetic wave with their respective electric (E) and magnetic (B) field components, (c) propagation of electromagnetic waves on transparent substrates ($k = 0$) and (d) on a light-absorbing substrate ($k > 0$) (Adapted from ref 134).

$n_1 \sin\theta_1 = n_2 \sin\theta_2$	n_1 – Refractive index of environment n_2 – Refractive index of substrate θ_1 – Light propagation angle in the environment (º) θ_2 – Light propagation angle in the substrate (º)	**(2.8)**
$N = n - ik$	N – Complex refractive index. n – Refractive index of the material k – Extinction coefficient of the material	**(2.9)**
$\alpha = \frac{4\pi k}{\lambda}$	α – Absorption coefficient of the material λ – Light wavelength (nm)	**(2.10)**

These parameters *n*, and *k* are related to key material properties and can be experimentally determined with ellipsometry. To determine these constants, it is necessary to mathematically describe the changes in light wave propagation. As referred previously, although electromagnetic waves consist of two components, it is conventional to consider only the electric field due to the higher magnitude of this component compared with the magnetic field. This electric field vector can be decomposed into two components: the parallel component (*p*) and the perpendicular component (*s*) relative to the plane of incidence. In dielectric materials, by considering the conservation of the *p* and *s* components across the boundary during reflection and refraction, one can derive the Fresnel reflection coefficients (**Equation 2.11** and **Equation 2.12**). These mathematically describe the reflection of light as the ratio of intensity between the vectors of the incident and reflected electric field, with the angles θ_1 and θ_2 related to Snell's law. [133,134]

$$\hat{r}_p = \frac{E_{rp}}{E_{ip}} = \frac{N_2\cos\theta_1 - n_1\cos\theta_2}{N_2\cos\theta_1 + n_1\cos\theta_2}$$

$\hat{r}_p$ – Fresnel reflection coefficient of the p component
E_{rp} / E_{ip} – p component of the electric field vector of the reflected (r) and incident (i) light

(2.11)

$$\hat{r}_s = \frac{E_{rs}}{E_{is}} = \frac{n_1\cos\theta_1 - N_2\cos\theta_2}{n_1\cos\theta_1 + N_2\cos\theta_2}$$

$\hat{r}_s$ – Fresnel reflection coefficient of the s component
E_{rs} / E_{is} – s component of the electric field vector of the reflected (r) and incident (i) light

(2.12)

When ellipsometry is performed, the emitted light beam can be linearly polarized (as in the case of this work), meaning that the p and s components have a phase difference of 0º (**Figure 2.10**). Upon light interaction with the sample, these components suffer a phase shift between 0º and 90º, turning the wave elliptically polarized. These changes can be expressed through the ratio of the Fresnel reflection coefficients, which are simultaneously related to the ellipsometric angles – the phase shift (Δ) and the azimuthal angle (ψ), as shown in **Equation 2.13**. From **Equation 2.14** one can observe that, in a two-phase system (media/substrate), at a given wavelength (λ), the values of Δ and ψ are directly related to the optical parameters – the complex refraction indexes and the angle of incidence. This relationship is also valid for a three-phase system (environment/film/substrate) as represented in **Equation 2.15**.[133,134]

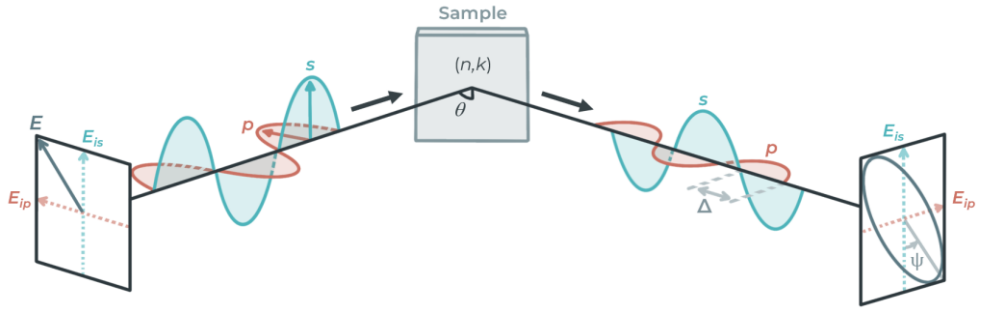

Figure 2.10 – Scheme of the measurement principle behind ellipsometry (Adapted from ref 134).

$$\rho = \frac{\hat{r}_p}{\hat{r}_s} = \tan\psi\, e^{i\Delta}$$

ρ – Complex reflectance ratio
ψ – Azimuthal angle (°)
Δ – Phase difference (°)

(2.13)

$$\Psi, \Delta = \Psi, \Delta\,[n_1(\lambda), N_2(\lambda), \theta_1]$$

ψ – Azimuthal angle (°)
Δ – Phase difference (°)

(2.14)

$$\Psi, \Delta = \Psi, \Delta\,[n_1(\lambda), N_2(\lambda), N_f(\lambda), \theta_1, \lambda, L_f]$$

ψ – Azimuthal angle (°)
Δ – Phase difference (°)
N_f – Complex refractive index of film
L_f – Film thickness (Å)

(2.15)

As such, a homogeneous, isotropic, and light absorptive ($k \neq 0$) film is optically characterized by three main parameters – n, k, and L (thickness). However, ellipsometry only provides two measurements – Δ_1 and ψ_1 – making the system mathematically undetermined, since there are three unknowns and only two variables. This limitation can be addressed by performing another measurement at a different angle of incidence, obtaining Δ_2 and ψ_2 and making the system solvable. Alternatively, one of the unknown parameters can be determined independently (such as measuring L with AFM) reducing the system to two unknowns.[133]

2.1.5 Water Contact-Angle Measurements

Wettability is an intrinsic property of solid materials that provides insights into their affinity with certain liquids at the solid-liquid interface. This characteristic is commonly assessed through the contact angle, which is the angle between the tangent to the liquid-vapor interface and the solid surface at the three-phase phase contact line, as represented in **Figure 2.11**.[135] This interaction is primarily defined by the surface energy of the solid material and the surface tension of the liquid, forming a spherical shape of the liquid over the surface controlled by the balance between adhesive (liquid-surface) and cohesive (liquid-liquid) forces.[136,137]

To measure and study the water contact angle, several basic wetting models have been proposed. However, Young's Wetting Model still remains one of the most widely used. This model considers that, for a droplet placed over an ideal surface (*i.e*, nonreactive, chemically homogeneous, nondeformable by the liquid and isotropic), the water contact angle can be determined with **Equation 2.16**.[135,136]

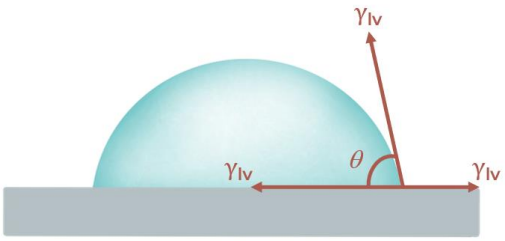

Figure 2.11 – A drop of water over an ideal substrate representing Young's wetting model (Adapted from ref 135).

$$\cos\theta = \frac{\gamma_{sv} - \gamma_{sl}}{\gamma_{lv}} \qquad \begin{array}{l} \gamma_{sv} - \text{Solid-vapor interfacial tension} \\ \gamma_{sl} - \text{Solid-liquid interfacial tension} \\ \gamma_{lv} - \text{Liquid-vapor interfacial tension} \\ \theta \ - \text{Young's contact angle (°)} \end{array} \qquad \textbf{(2.16)}$$

In the case of the measurement of Water Contact Angles (WCA), the resulting angle allows to conclude on the hydrophilicity or hydrophobicity of the material. By convention, a surface is considered hydrophilic if it presents a WCA < 90 º. Surfaces with a WCA between 90 º and 150 º are considered hydrophobic. When the contact angle exceeds 150 º, the surface is superhydrophobic.[136]

2.2 Experimental Conditions and Procedures

2.2.1 Reagents

As for the synthesis and optimization of the copolymers, the following reagents were used: dopamine hydrochloride (DA; $C_8H_{11}NO_2{\cdot}HCl$; 189.64 g mol^{-1}; 99.8 %; Sigma-Aldrich), 3,4-ethylenedioxythiophene (EDOT; $C_6H_6O_2S$; 142.18 g mol^{-1}; 98.5 %; Acros Organics), dextran sulfate sodium salt (DS; $(C_6H_7O_5)_m(C_6H_7O_5)_n$; MW *ca.* > 500.000; ThermoScientific), sodium dodecyl sulfate (SDS; $C_{12}H_{25}NaO_4S$; 288.38 g mol^{-1}; Fischer Scientific), Sodium poly(4-styrenesulfonate) (PSS; $(C_8H_7NaO_3S)_n$; MW ~1,000,000, Aldrich Chemistry), and sodium perchlorate ($NaClO_4$; 122.44 g mol^{-1}; 99%; Acros Organics). All reagents were used as received, without additional purification. To prepare all the aqueous solutions, ultrapure water from a MILLI-Q A10 gradient purification system (18.2 MΩ cm at 25 ºC) was used. For additional characterization, potassium iron cyanide ($K_3[Fe(CN)_6]$; 329.26 g mol^{-1}; 98%; Merck) was used.

Two buffers, Citrate Phosphate Buffer (CPB) and Phosphate Buffer (PB) were needed for additional studies. To prepare them, citric acid monohydrate ($C_8O_6H_7{\cdot}H_2O$; 210.14 g mol^{-1} ; 98%; Sigma-Aldrich), disodium hydrogen phosphate dodecahydrate ($Na_2HPO_4{\cdot}12H_2O$; 358,14 g mol^{-1} ; 98%; Merck), and di-

sodium dihydrogen phosphate (NaH_2PO_4; 119.98 g mol^{-1} ; 98%; Merck) were used. The concentrations for each buffer are represented in **Table 2.1**.

Table 2.1 – CPB and PB buffer composition and pH (at 25 ºC).

Buffer	Composition	pH
CPB	17 mM $C_8O_6H_7 \cdot H_2O$; 66 mM $Na_2HPO_4 \cdot 12H_2O$	7.0
PB	42 mM NaH_2PO_4 ; 58 mM $Na_2HPO_4 \cdot 12H_2O$	

For electrode cleaning procedures, sulfuric acid (H_2SO_4; 98.08 g mol^{-1}; 98%; Fischer Chemical), hydrogen peroxide (H_2O_2; 34.0147 g mol^{-1}; > 30 %; Fischer Chemical), and sodium hydroxide (NaOH; 40.00 g mol^{-1}; 99%; Chemlab) were used.

2.2.2 Electrodes and Electrochemical Cells

The electrochemical measurements were performed using a three-electrode system. A silver/silver chloride (Ag/AgCl, KCl saturated) electrode was used as a reference, while a platinum sheet served as counter electrode, as represented in **Figure 2.12a** and **2.12b**. Both electrodes were rinsed with ultrapure water before and after each assay. When necessary, the platinum electrode was briefly exposed to a flame to remove any organic residues. As for the working electrode, several gold and carbon-based substrates were needed and are represented in **Figure 2.12c** to **2.12g**.

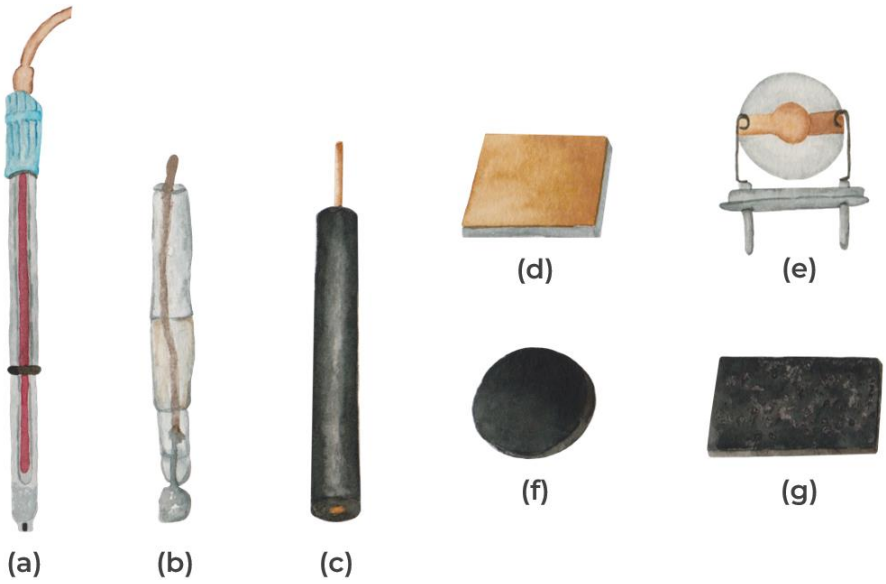

Figure 2.12 – Electrodes used for electrochemical assays: (a) Ag/AgCl reference electrode, (b) platinum counter electrode and the working electrodes of polycrystalline gold (c), (d) Arrandee™, (e) quartz crystal and of (f) glassy carbon (GC) and (g) hard graphite.

Initially, to optimize the synthesis of the copolymer films, a polycrystalline gold electrode (2 mm diameter) was used. The electrode was mechanically polished with alumina suspensions (Al_2O_3) with particles sizes of 1.0 and 0.3 µm (Buehler) using a synthetic fiber cloth (Buehler Microcloth) for approximately 10 minutes. After this, the electrode was electrochemically activated in H_2SO_4 (0.1 M) by sweeping the potential between 0 to 1500 mV (*vs.* Ag/AgCl) for 10 cycles at a scan rate of 200 mV s^{-1}. Between each step and before the assays, the electrode was always thoroughly rinsed with ultrapure water.

After optimizing the synthesis of the intended polymers, these were characterized with gold Arrandee™ electrodes (for AFM, ellipsometry, WCA, *in-situ* UV-vis, Fourier Transform Infrared

Spectroscopy (FTIR) and Raman) and quartz crystal electrodes for EQCM. The Arrandee™ electrodes consist of a 200 nm gold layer deposited over borosilicate glass. In the case of the EQCM electrodes, an 8 MHz AT-cut quartz crystal coated with a 100 nm gold thin film on both sides was used. Both of these electrodes present a pre-layer of chromium (2 - 5 nm) to enhance gold adhesion to the substrates. Prior to use, the electrodes were cleaned by exposing the gold surface to piranha solution (1:3 (v/v) hydrogen peroxide/sulfuric acid) for 10 minutes to remove any organic residues and rinsed with ultrapure water and ethanol.

To further apply these polymers on sustainable and low-cost substrates, initial studies were performed on a glassy carbon electrode. The electrode was mechanically polished with alumina suspensions (Al_2O_3) with particles sizes of 1.0 and 0.3 μm (Buehler) approximately 10 minutes. Following this, it was electrochemically activated in NaOH (0.2 M) by cycling the potential between -500 to 900 mV (*vs.* Ag/AgCl) for 10 cycles at a scan rate of 200 mV s^{-1}. Between each step and before the assays, the electrode was always thoroughly rinsed with ultrapure water.

Finally, for their application as cathode materials, the copolymers were studied on polycrystalline graphite plate electrodes. The surface was mechanically polished using sandpaper of varying granulometries (p180, p320, and p1200) to obtain a uniform polishing. Afterward, these were immersed in ultrapure water and subjected to ultrasonic cleaning for 10 minutes to remove dispersed carbon powder.

Considering the different types and geometries of working electrodes, different electrochemical cells were used during this work. For the polycrystalline gold electrode, a two-compartment glass cell was used (**Figure 2.13a**). As for the Arrandee™, glassy carbon, and the hard graphite plate electrodes, a Teflon cell (**Figure 2.13b**) was used, where the electrochemically active area was defined by the diameter of the cell base, while the electrical contact was made through a strip of aluminum foil. In the case of quartz crystal electrodes, a specially designed Teflon cell for EQCM was used (**Figure 2.13c**).

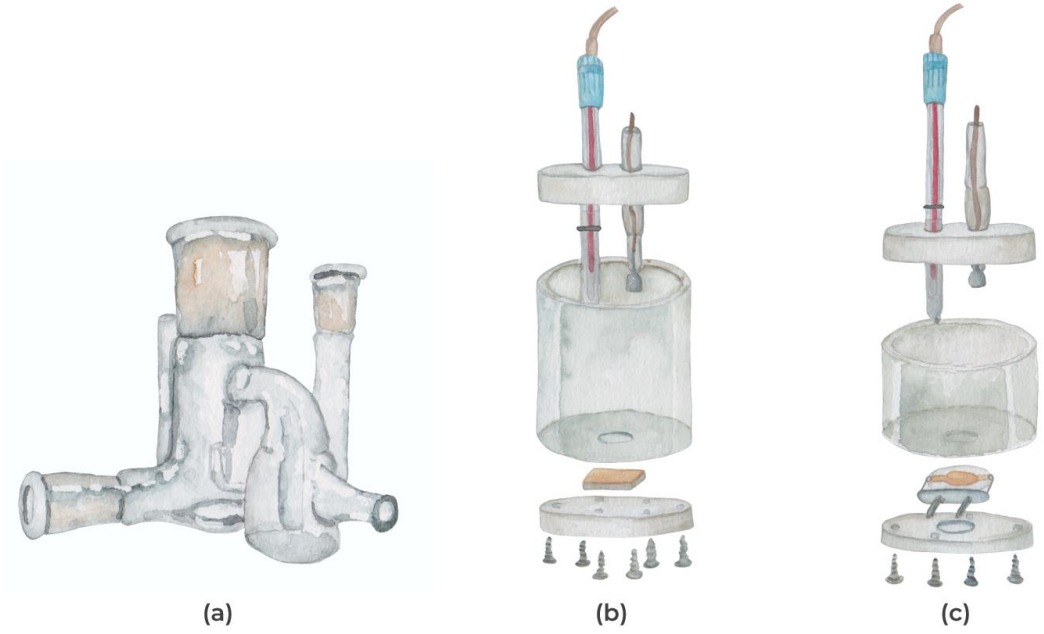

Figure 2.13 – Schematical representation of (a) two-compartment glass cell and Teflon cells for (b) larger electrodes and (c) EQCM electrodes.

2.2.3 Instrumentation Methods

2.2.3.1 Electrochemical and Electrogravimetric Measurements

The electrode modification with polymeric films and their characterization were performed using a PARSTAT 2263 produced by AMETEK (Princeton Applied Research, Pennsylvania, USA) or a CHI600A Electrochemical Analyzer (CH Instruments, Inc., Texas, USA). In the case of the EQCM assays, these were synthesized and characterized with a CHI420 Electrochemical Analyzer (CH Instruments, Inc., Texas, USA) coupled to an oscillator.

For the preparation of monomeric solutions, 10 mM of EDOT and the selected electrolyte were previously prepared and stirred for approximately 6 h, presenting a pH of 6.7. With this EDOT/DS solution, all the mixtures of DA/EDOT/DS were freshly prepared and used. Before the potentiostatic synthesis, all solutions were deoxygenated for 10 minutes with pure N_2. In the case of potentiodynamic growth or characterization of the electrode surface, the solutions were deoxygenated for 20 minutes, also with pure N_2. For the characterization of the polymer films after their synthesis, these were characterized in 50 mM DS from -800 to 800 mV (*vs.* Ag/AgCl) for 10 cycles at 50 mV s^{-1}, unless stated otherwise.

2.2.3.2 Atomic Force Microscopy (AFM)

The morphology of modified gold Arrandee™ electrodes was characterized using *ex-situ* AFM measurements. These were performed in air (22 ± 1 °C) with a Multimode 8 HR microscope coupled to a Nanoscope V (Bruker, Massachusetts, USA). *Peak Force Tapping* mode was employed using silicon nitride ScanAsyst-Air probes (Bruker) with a spring constant of approximately 0.4 N m^{-1} and a resonance frequency of 300 kHz. Prior to imaging, the probes were calibrated on a mica substrate to determine deflection sensitivity, and the spring constant was obtained via thermal tuning. Topography was recorded at a scan rate of ~1.0 Hz while the probe oscillated at a frequency of 2 kHz in ScanAsyst mode. To assess film thickness, the film was scratched using the edge of a paper sheet to expose the underlying gold surface, allowing the measurement of the height profile.

2.2.3.3 Ellipsometric Measurements

To determine the optical parameters of the synthesized films (refractive index (n), extinction coefficient (k), and film thickness (L)) *ex-situ* ellipsometric experiments were performed. The measurements were obtained using a SE400 single-wavelength ellipsometer (SENTECH Instruments GmbH) equipped with a He-Ne laser ($\lambda = 632.8$ nm) in a PSA (polarizer-sample-analyzer) configuration. A total of 10 analyzer rotations were recorded at each of the two selected angles of incidence (65° and 70°). The experimental data were interpreted using a three-phase optical model consisting of a semi-infinite gold substrate (Arrandee™), coated with a homogeneous and isotropic polymer layer, and exposed to air.

2.2.3.4 Water Contact-Angle Measurements

WCA analysis was used to evaluate the wettability of the modified gold Arrandee™ surfaces. Measurements were performed using a Krüss DSA30 goniometer by dispensing a 1 µL droplet of ultrapure water onto the sample surface. The resulting contact angle was determined using Krüss Drop Analysis software. For each polymer, three independent samples were analyzed to ensure reproducibility.

2.2.3.5 UV-vis Reflectance Spectroscopy

In-situ UV-vis reflectance spectroscopy measurements were performed using a FLEX spectrometer (Sarspec) equipped with a specular and diffuse reflectance probe. Data was acquired using Light Scan software at fixed potentials during both film deposition and characterization. For the latter,

measurements were carried out on a modified electrode in a 0.1 M sodium perchlorate solution free of monomer.

2.2.3.6 FTIR and Raman Spectroscopy

FTIR spectra was obtained with an INVENIO-S FTIR spectrometer (Bruker) in the reflectance mode with an incident angle of 80 º. During spectra acquisition, 512 scans were collected for each sample with a 4 cm^{-1} resolution.

Raman spectroscopy measurements were performed at Instituto Superior Técnico by Dr. Luis Santos using a confocal LabRAM HR 800 Evolution micro-Raman spectrometer. Data was acquired in the range of 100 - 1800 nm, using an external diode laser with a wavelength of 532 nm to excite the sample, a 100× objective and ~ 10 mW laser power at the samples.

2.2.3.7 Battery Half-Cell Charge/Discharge Tests

For potentiostatic charge and discharge cycles, the synthesized electrode films were tested in 0.1 M $NaClO_4$ applying 700 and -600 mV (*vs.* Ag/AgCl) for 5 s per pulse. These tests were performed using a CHI420 Electrochemical Analyzer (CH Instruments, Inc., Texas, USA).

The galvanostatic charge and discharge cycles were also tested in 0.1 M $NaClO_4$ applying the estimated oxidation and reduction current of each corresponding C-rate. These tests were performed using a VoltaLab PGZ100 potentiostat/galvanostat (Radiometer Analytical).

Chapter 3

Synthesis and Characterization of PEDOT/PDA Copolymers

"…*The electrode is the stage; the solution is the theater and the audience. It is also the place that supplies the players—ions and solvent—while electrons are clearly supplied from resources in the wings."*

John Bockris in *Modern Electrochemistry* (Volume 1; 2nd Edition)

3. Synthesis and Characterization of PDA/PEDOT Copolymers

3.1 Synthesis and Optimization of PDA/PEDOT Copolymers

The main goal of this thesis is to synthesize hybrid PDA/PEDOT copolymers, where the electronic conductivity of PDA and the sodium-ion intake observed in PEDOT are improved. The resulting material should preserve their most prominent properties, enhancing stability and performance as cathode material for sodium-ion batteries. Therefore, it is necessary to select an ideal synthesis method and optimize synthesis conditions to obtain the desired properties of the material.

As for the synthesis method, the direct electropolymerization of the monomers was preferred due to its simplicity, reproducibility, and uniformity during film deposition.[138] Compared to previously electrosynthesized PDA/PEDOT materials, this approach aims to decrease synthesis times and improve the resulting copolymer by incorporating a surfactant into the monomeric solution, also serving as a dopant to assist ion incorporation in order to impart pseudocationic character to the copolymer. When one intends to electrochemically synthesize a certain polymer, the starting point is to identify a set of conditions and parameters where its polymerization is favorable. As such, if the target is to synthesize a copolymer material, one must meet intermediate conditions that favor the polymerization of both monomeric forms.

As referred in Chapter 1, although PDA is widely known for its chemical polymerization, the electrochemical synthesis of this polymer has significant advantages.[139] The electropolymerization of PDA is commonly performed potentiodynamically in the presence of buffer electrolytes (*e.g.*, Citrate-Phosphate Buffer, Tris-Buffered Saline, Phosphate Buffered Saline) under a potential window typically around -600 to 800 mV at a varied range of sweep rates (20 - 200 mV s^{-1}) and number of cycles, dependent on the intended thickness and application.[87,140,141]

On the other hand, conventional electrosynthesis of PEDOT was initially performed in acetonitrile due to its hydrophobic nature.[142,143] Nevertheless, in recent years, the use of aqueous dispersions with sodium dodecyl sulfate (SDS), dextran sulfate sodium (DS), or poly(4-styrenesulfonate) (PSS), has been reported for aqueous syntheses that allow pseudocationic doping.[144–146] Over time, several studies have proven that the electropolymerization conditions of PEDOT highly influence the properties of the polymeric film. Therefore, the mode and conditions under which PEDOT is grown also depend on the application.[144,147]

Considering this, the PDA/PEDOT copolymer was synthesized potentiodynamically and potentiostatically to evaluate which conditions favor the film growth. During the initial tests, DS was chosen due to its hydrophilic nature and biocompatibility, possibly promoting its simultaneous affinity with DA.[148,149] Hence, to assess the synthesis of the copolymer films, it was expected to find intermediate properties of both chemical species. During all the tested conditions, the films were evaluated based on their voltammetric response on a monomer-free solution (50 mM of DS). Thus, an ideal copolymer film should present the typical pseudocapacity of PEDOT and the redox conversion of the quinones in PDA.

3.1.1 Potentiodynamic Growth of PDA/PEDOT Copolymer Films

In the first analysis, the monomers were individually polymerized and copolymerized potentiodynamically on a gold polycrystalline electrode to explore their redox behavior and oxidation potential (**Figure 3.1**). In the case of EDOT (**Figure 3.1a**), the monomer oxidation starts *ca.* 700 mV *vs.* Ag/AgCl (I_{ox}). This oxidation corresponds to the activation of the monomer in the form of a radical cation, which then reacts with other EDOT monomers at the interface (**Figure 3.2**).[42] These addition reactions form oligomeric species that, upon oxidization, will form oligomeric cations. Finally, further oxidation and addition of oligomeric species, eventually lead to the deposition of an insoluble polymeric film of PEDOT on the electrode surface. This process is evidenced by the overlap of current density lines in **Figure 3.1a**, which reflects the nucleation of a new phase over the working electrode. After 10 voltammetric cycles, the oxidation current increases and the pseudocapacity increases progressively, indicating the formation of a conductive material over the electrode surface.

The polymerization of DA involves a more complex mechanism, originating from monomer cycling and isomerization (**Figure 3.1b**). During the first cycle, the oxidation of DA is recorded *ca.* 720 mV (I_{ox}) while the reduction occurs *ca.* 195 mV *vs.* Ag/AgCl (I_{red}). These peaks correspond to the redox conversion of the pair quinone/catechol in the open form of the monomer. On the first cycle, another reduction peak is observed at 40 mV *vs.* Ag/AgCl (II_{red}). This peak can be attributed to the conversion of indolic moieties and other substituted species (originated from the chemical oxidation of dopaminequinone), whose oxidation to quinone is noticed in later cycles *ca.* 210 mV *vs.* Ag/AgCl (II_{ox}). The oxidation of these monomeric species to quinone makes them more reactive and prone to suffer 1,4-Michael additions, which leads to the polymerization of PDA (**Figure 3.3**).[87] A more detailed and comprehensive explanation of the polymerization mechanism of PDA and other catecholamines can be found in existing literature.[82,87]

After 10 potential cycles, one can observe a decrease in the oxidation and reduction currents, indicating the deposition or adsorption of insulating species over the electrode. Moreover, the redox potential suffers a positive potential shift, corresponding to a difficulted electron transfer. Assuming this behavior corresponds to polymer deposition, one would expect the formation of a PDA film that incorporates the different building blocks generated from the chemical conversion of DA monomers, whether in its open, cyclized, or isomerized forms, building a heteropolymer as represented in **Figure 3.3**.[81]

When both monomers (EDOT and DA) are copolymerized under potentiodynamic control (**Figure 3.1c**), one can observe that the redox currents of EDOT are overshadowed by the current response of DA in solution. Hence, the response strongly resembles the voltammogram recorded with DA. Nevertheless, a slight difference can be noticed – the oxidation potentials of DA suffer a negative shift after 10 cycles, which indicates a facilitated charge transfer. However, after the electrode characterization in monomer-free solution, it was confirmed that little deposition of copolymer film had occurred (**Figure 3.1d**), when comparing to the response of bare gold. Considering this, to improve and study the deposition of the film, a higher number of polymerization cycles were tested and followed with EQCM to monitor the mass increase during the electropolymerization process.

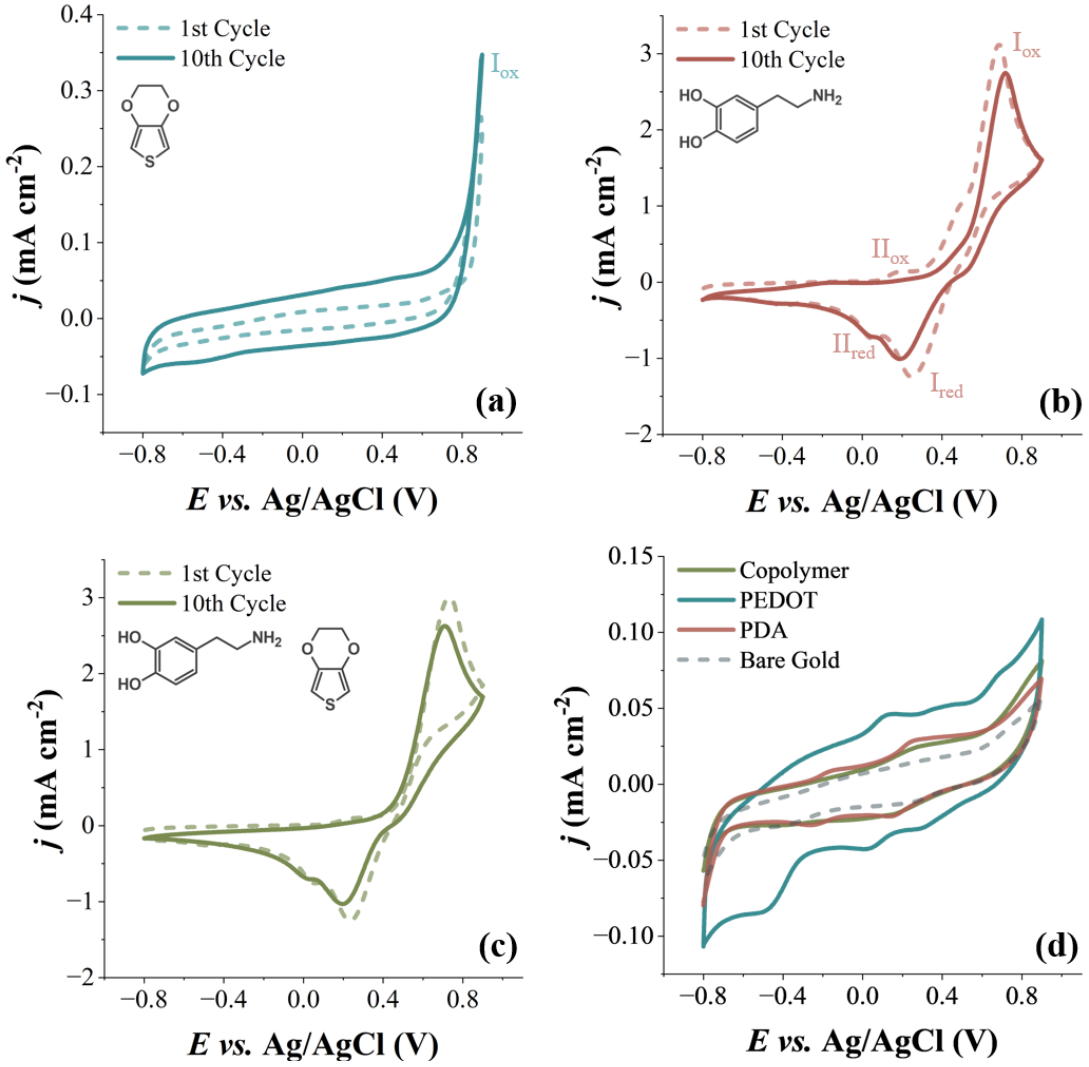

Figure 3.1 – Potentiodynamic growth of (a) EDOT (10 mM), (b) DA (20 mM), and (c) copolymer (20 mM DA and 10 mM EDOT) at 50 mV s^{-1} from -800 to 900 mV (*vs.* Ag/AgCl) for 10 cycles in deoxygenated 50 mM DS solution. (d) 10th characterization cycle of the synthesized polymeric materials in 50 mM DS at 50 mV s^{-1}.

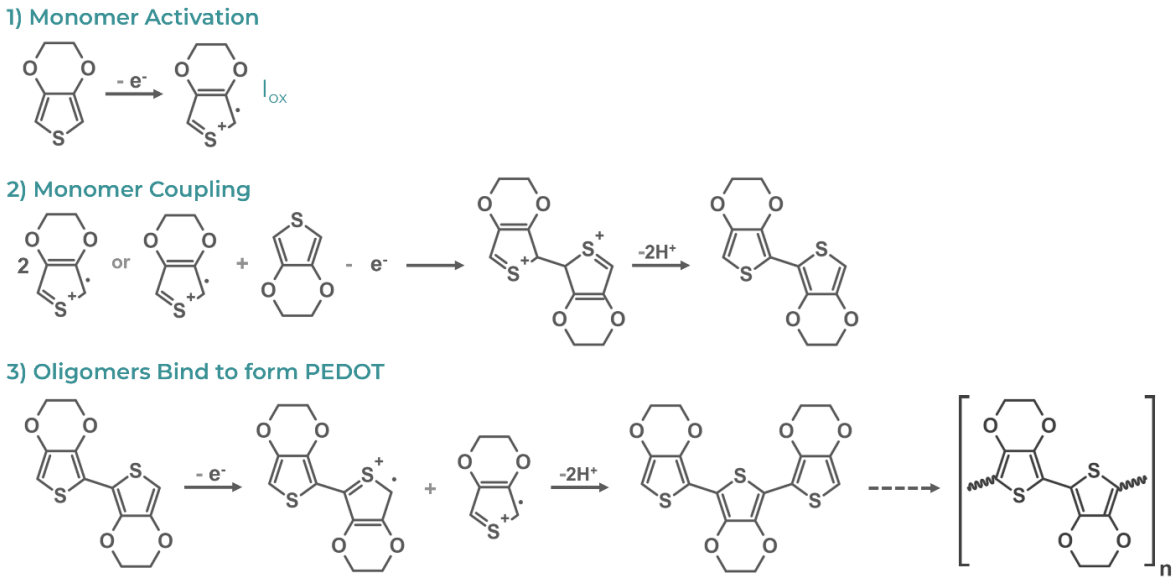

Figure 3.2 – Stepwise polymerization mechanism of PEDOT.

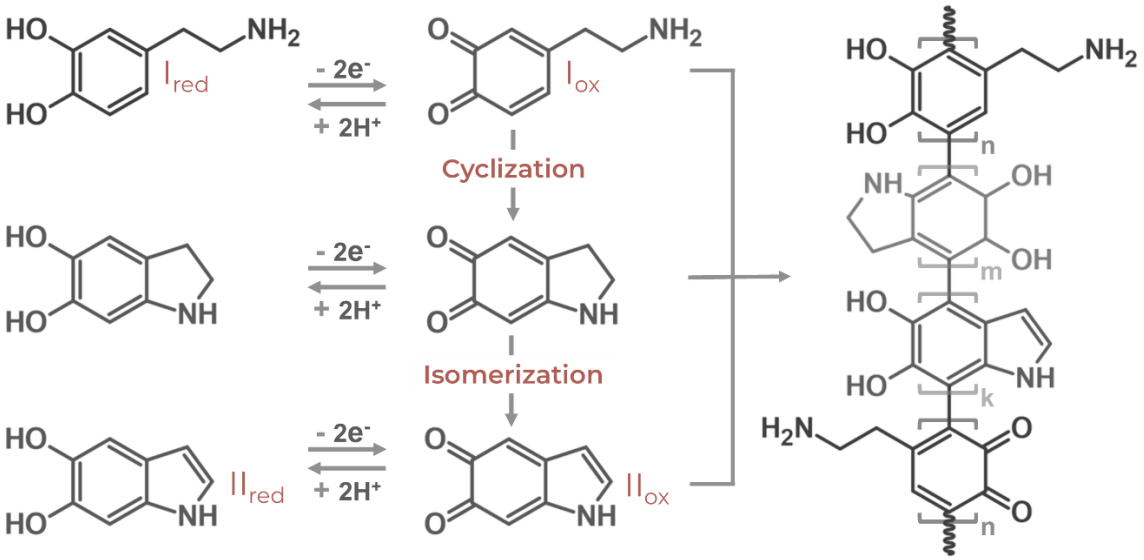

Figure 3.3 – Stepwise polymerization mechanism of PDA.

The copolymer growth using EQCM was performed from -800 to 950 mV (*vs.* Ag/AgCl) during 50 cycles to promote copolymer deposition. The voltammetric response and the corresponding mass changes during the synthesis of each system are shown in **Figure 3.4** and **Figure 3.5**, respectively. The current profile of PEDOT (**Figure 3.4a**) exhibited an increase in pseudocapacity, indicating considerable polymer deposition, whereas PDA (**Figure 3.4b**) maintained a similar voltametric profile between the 1st and 50th cycles.

In the case of copolymer deposition (**Figure 3.4c**), a noticeable change is observed in the voltammogram, resembling the profile reported for the copolymerization of DA with pyrrole (Py) where a significant shift of the oxidation potentials of DA monomers is observed.[107] However, in this case, there is a progressive decrease in both oxidation and reduction currents. Despite this, the oxidation and reduction peaks of dopamine can still be identified at approximately 911 and 110 mV (*vs.* Ag/AgCl), respectively. During the electrodeposition, the recorded frequency variation of the copolymer shows an interesting mass inflection (**Figure 3.5a**), also observed in the copolymerization of PDA/PPy films. This small mass increments progressively increases with the number of polymerization cycles in the potential range from -500 to 800 mV *vs.* Ag/AgCl (**Figure 3.5b**). Although it remains unclear, this response might correspond to the adsorption and desorption of dopamine-related species, whose incorporation increases proportionally with the number of cycles due to the active surface area during polymer deposition.[142]

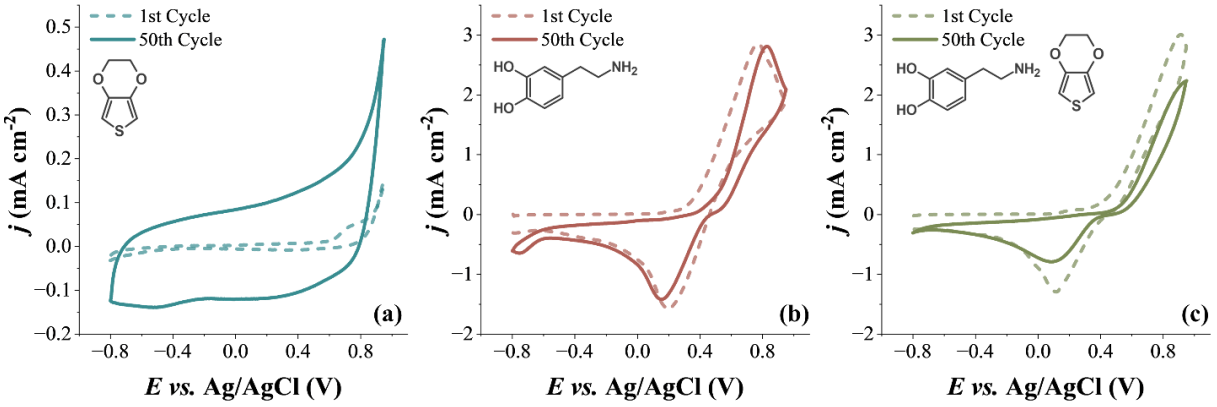

Figure 3.4 – Potentiodynamic growth by EQCM of (a) EDOT (10 mM), (b) DA (20 mM), and (c) copolymer (20 mM DA and 10 mM EDOT) from -800 to 950 mV (*vs.* Ag/AgCl) for 50 cycles in deoxygenated 50 mM DS solution at 50 mV s^{-1}.

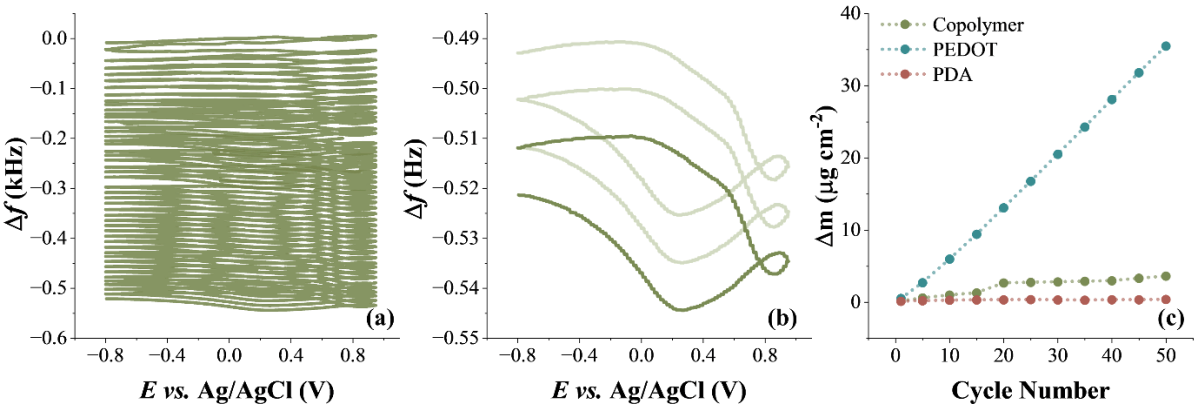

Figure 3.5 – (a) Frequency variation during 50 cycles of potentiodynamic growth of the copolymer (20 mM DA and 10 mM EDOT) in 50 mM DS at 50 mV^{-1} from -800 to 900 mV *vs.* Ag/AgCl. (b) Zoomed-in frequency variation during the last 3 cycles of potentiodynamic growth of the copolymer. (c) Mass change during the cycles of potentiodynamic growth of each system.

Considering the validity of the Sauerbrey equation for thin and rigid films,[121] the mass depositions for each system was compared (**Figure 3.5c**) revealing significantly different deposition kinetics. While PDA exhibited almost no mass deposition, PEDOT reached a final mass of 35.5 μg cm^{-2} and the copolymer 3.6 μg cm^{-2}, meaning that PEDOT deposited ten times faster. Despite these differences, the variation in deposition kinetics points to the synthesis of a novel material distinct from pristine PDA and PEDOT polymers. Although this method demonstrated the potential to synthesize a new material, it was time-consuming and inefficient. Therefore, potentiostatic film growth was explored as an alternative synthesis approach.

3.1.2 Potentiostatic Growth of PDA/PEDOT Copolymer Films

Considering the polymerization potentials recorded during the potentiodynamic growth, the adequate potential window tested for copolymerization ranged from 800 to 950 mV (*vs.* Ag/AgCl). On that count, different potentials (800, 850, 900, and 950 mV *vs.* Ag/AgCl) were applied to the gold polycrystaline electrode for 320 s in the solution containing the monomer (20 mM DA and 10 mM EDOT) and the electrolyte (50 mM DS). This potentiostatic polymerization was also tested for pristine PEDOT and PDA synthesis (**Figure B1 –** Appendix B). While, in the case of PEDOT, an increase in pseudocapacity is observed with increasing potential, for PDA no significant deposition is recorded.

In the case of the potentiostatic deposition of PDA/PEDOT films (**Figure 3.6a**), a transient that follows the Cottrell equation is observed, rather than the typical response seen for PEDOT, where a progressive increase in current is observed after nucleation.[107] After synthesizing the copolymers at different applied potentials, all characterization voltammetric profiles (**Figure 3.6b**) confirmed the successful incorporation of hybrid PDA/PEDOT properties, presenting the typical pseudocapacityresponse of PEDOT together with the characteristic open form of quinone/catechol redox pair of PDA (Process I_{ox}/ I_{red}, **Figure 3.3**).

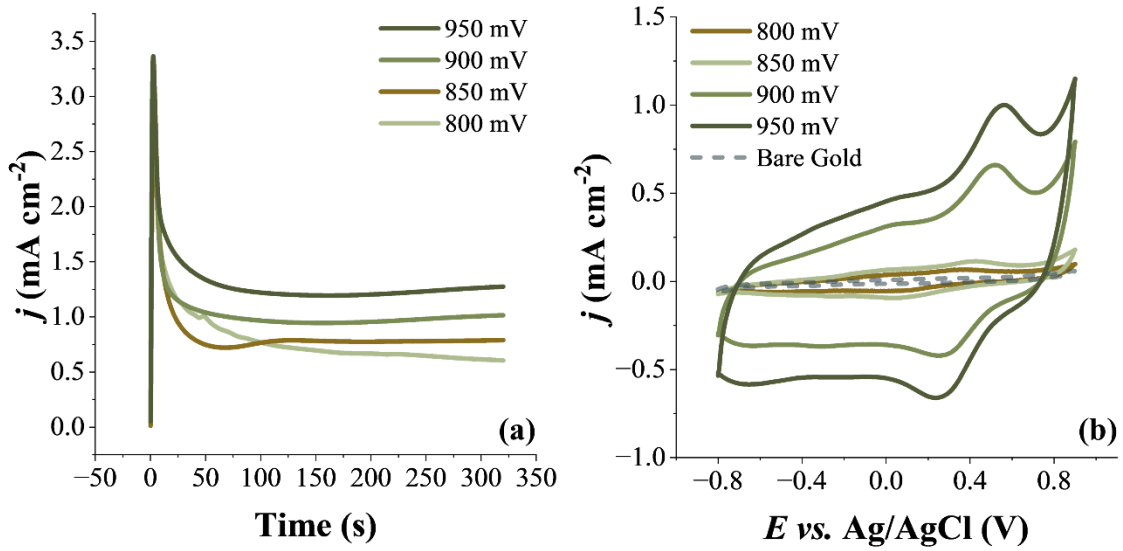

Figure 3.6 – (a) Potentiostatic growth of the copolymer film in 20 mM DA, 10 mM EDOT, and 50 mM DS at different potentials (800 to 950 mV *vs.* Ag/AgCl) for 320 s and (b) 10th characterization cycle of the polymerized film in deoxygenated 50 mM of DS at 50 mV s^{-1}.

From the cyclic voltammograms recorded in monomer-free electrolyte solution in **Figure 3.6b** and **Table 3.1**, an increase in synthesis potential was accompanied by a simultaneous increment in the total charge and a higher presence of quinone species. Additionally, a potential shift in the redox quinone/catechol response was recorded. This indicates the formation of a progressively thicker film, which was also verified visually during the experiment by changes of color over the electrode surface (**Figure B2** – Appendix B). Hence, because of the higher pseudocapacity and surface coverage of quinones (Γ_{cat}^{ox}), the chosen potential for synthesis was 950 mV *vs.* Ag/AgCl.

Additionally, to evaluate whether the redox species observed in the electrochemical characterization are immobilized within the copolymer, the film was characterized at different sweep rates. As represented in **Figure 3.7**, the dependence of anodic and cathodic peak currents of the quinone/catechol redox pair ($E_{1/2} \approx 420$ mV *vs.* Ag/AgCl) on the scan rate confirm their immobilization in the electrode material.

Table 3.1 – Electrochemical parameters: oxidation peak potential of catechol species (E^{ox}), reduction peak potential of quinone species (E^{red}), total charge from the catechol oxidation (Q_{cat}) and surface coverage of quinone species (Γ_{cat}^{ox}) of the copolymers deposited potentiostatically in 20 mM DA, 10 mM EDOT, and 50 mM DS at different potentials (800 to 950 mV *vs.* Ag/AgCl) for 320 s.

Potential (mV)	E^{ox} **(mV *vs.* Ag/AgCl)**	E^{red} **(mV *vs.* Ag/AgCl)**	Q_{cat} **(mC cm^{-2})**	Γ_{cat}^{ox} **(×10^{-9} mol cm^{-2})**
950	555	285	1.50	7.80
900	515	270	1.10	5.71
850	430	75	0.12	0.61
800	365	53	0.10	0.52

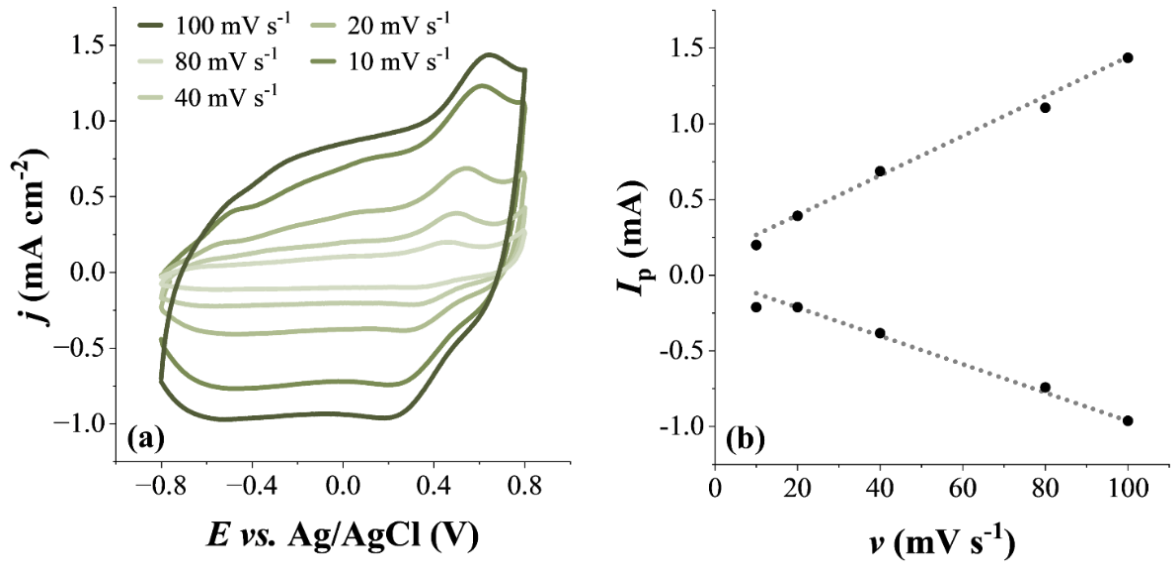

Figure 3.7 – (a) Voltammetric response at different scan rates of the copolymer film grown in 20 mM DA and 10 mM EDOT in 50 mM DS at 950 mV (*vs.* Ag/AgCl) for 320 s. (b) Current dependence of the scan rate on the anodic and cathodic of PDA/PEDOT copolymers in a deoxygenated solution of 50 mM DS (pH = 6.7).

Other conditions were also tested to optimize the electropolymerization of the copolymer and its electrochemical properties. To assess if an increase in DA concentration would proportionally provide a higher incorporation of quinone species, 40 mM of DA was tested and compared with 20 mM (**Figure 3.8a** and **Figure 3.8c**). Results of characterization showed that, despite presenting a higher current on the transient, a higher concentration of DA maintained a similar redox response of the quinone/catechol pair and lowered the pseudocapacity. Thus, the considered concentration of DA for the electrosynthesis of the copolymer was 20 mM.

On the other hand, a different concentration of DS (10 mM) and different electrolytes (50 mM SDS and PSS) were tested to evaluate their influence on copolymer properties (**Figure 3.8b** and **Figure 3.8d**). In all cases, the redox response of the quinone/catechol couple and the pseudocapacity were lower than in the copolymer synthesized with 50 mM DS. The films obtained with SDS and PSS showed additional well-defined redox peaks corresponding to PEDOT, suggesting that these electrolytes have a good interaction with EDOT and may promote the formation of a better conducting polymer. This effect is possibly related to the more hydrophobic nature of these electrolytes compared to DS. However, the PDA component decreased significantly, even observing a difficulted electron transfer in the oxidation of the SDS copolymer film. These results suggest that the hydrophilicity and biocompatibility of DS may favor the incorporation of DA into the copolymer material.

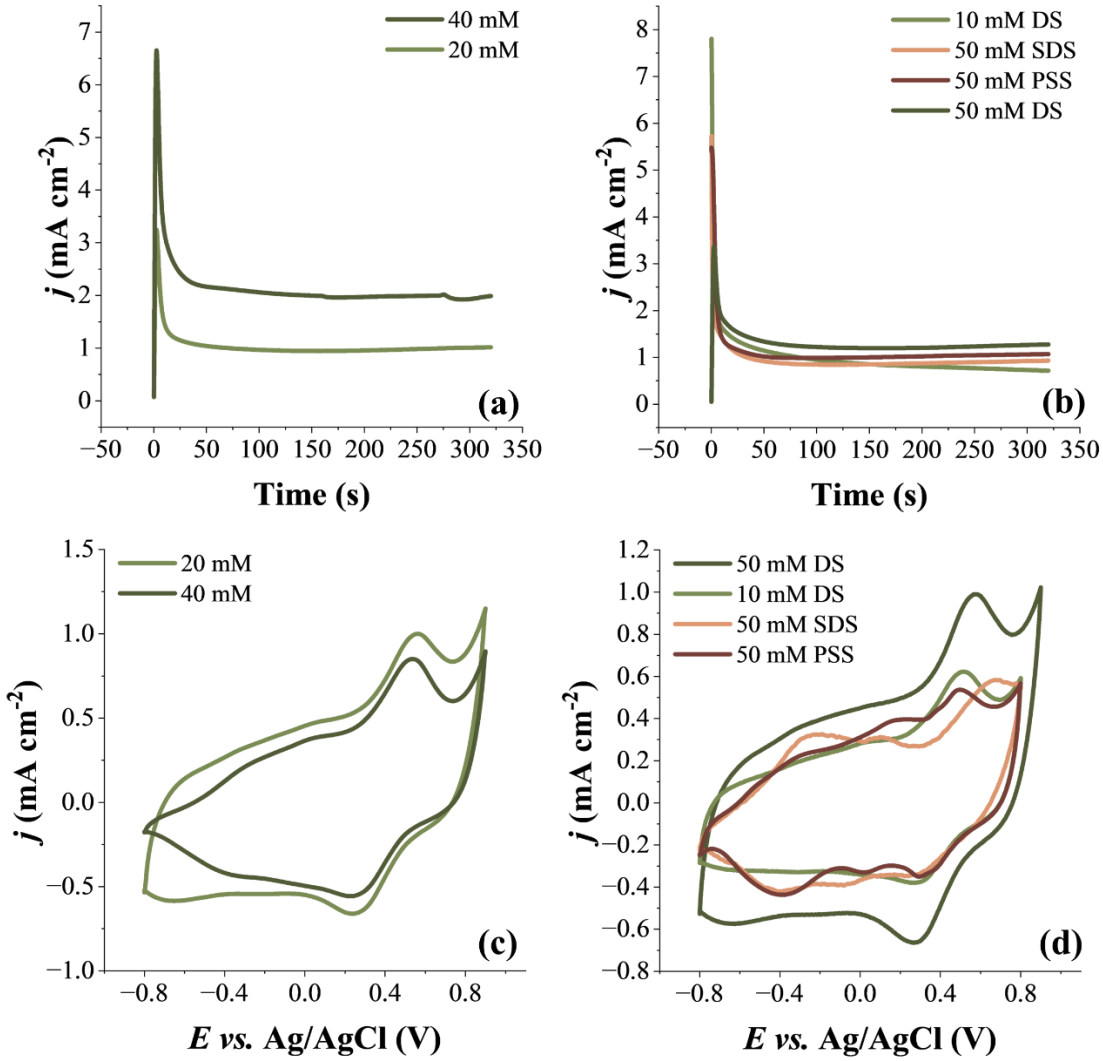

Figure 3.8 – (a) Potentiostatic growth of the copolymer with 40 mM and 20 mM of DA at 950 mV (*vs.* Ag/AgCl) for 320 s in the presence of 10 mM EDOT and 50 mM DS. (b) Potentiostatic growth of the copolymer in 50 mM DS, 50 mM SDS, 50 mM PSS, and 10 mM DS at 950 mV (*vs.* Ag/AgCl) for 320 s in the presence of 20 mM DA and 10 mM EDOT. (c) and (d) 10th characterization cycle of the modified electrodes in 50 mM of DS at 50 mV s^{-1}.

With the previous results, it was possible to conclude that the best tested conditions for the copolymerization of PDA/PEDOT films are a monomeric solution containing 20 mM DA and 10 mM EDOT in 50 mM DS, with an applied potential of 950 mV (*vs.* Ag/AgCl) for 320 s. Once a synthesis method was established, DA and EDOT monomers were individually studied under these conditions and compared to the resulting copolymer (**Figure 3.9**). In the case of pure PDA and the copolymer, a typical transient originating from the oxidation of DA in solution is observed (**Figure 3.9a**), as explained previously. Conversely, the transient obtained from PEDOT reveals the expected profile for its synthesis in an aqueous medium. The initial increase in current corresponds to the nucleation and oxidation stages near the electrode, followed by a progressive growth in current that corresponds to the deposition of a conducting polymer.[149]

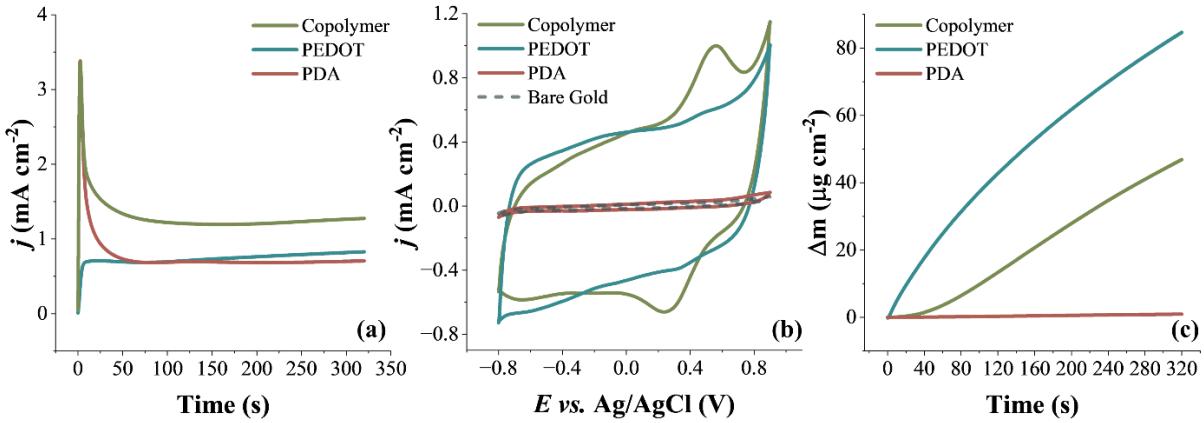

Figure 3.9 – (a) Potentiostatic response of 20 mM DA (PDA), 10 mM EDOT (PEDOT) and 20 mM of DA with 10 mM of EDOT (copolymer) in 50 mM of DS at 950 mV (*vs.* Ag/AgCl) for 320 s. (b) 10th characterization cycle of the electrode surface in deoxygenated 50 mM of DS at 50 mV s^{-1}. (c) EQCM response of copolymer, PEDOT and PDA during potentiostatic deposition.

As for their electrochemical characterization (**Figure 3.9b**), PDA presents a voltammetric profile similar to bare gold, indicating no (or scarce) deposition of polymeric film, later confirmed with EQCM results (**Figure 3.9c**). In contrast, the two additional faradaic peaks observed in the electrochemical response of the copolymer correspond to the redox of the quinone/catechol moieties, indicating the successful incorporation of PDA into the hybrid material. Under the same conditions, PEDOT and the copolymer exhibit very similar pseudo-capacitive charges (1.388 and 1.331 mC cm^{-2}, respectively), indicating that a hybrid PDA/PEDOT copolymer has been successfully synthesized without compromising their electrochemical behavior, as initially intended. Considering the validity of the Sauerbrey equation for thin and rigid films,[121] at the end of the syntheses followed with EQCM, PEDOT presented a final mass of 84.7 μg cm^{-2}, while the copolymer deposited roughly 46.8 μg cm^{-2}. This final mass counts for the weight of the polymer and solvent incorporated during film deposition. Yet, despite this great mass difference, it is curious to find that both materials have a comparable electroactivity.

Even though electrochemical characterization and EQCM results point to the successful synthesis of a new hybrid material, we are still blind to other physicochemical properties it may possess, as well as to how much the individual polymeric features of PEDOT and PDA have been altered. Therefore, Chapter 3.2 will explore these aspects in greater detail using AFM and other spectroscopic techniques.

3.2 Physicochemical Characterization of PDA/PEDOT Copolymers

Ideally, to understand the properties of a copolymer, one should compare its properties with those of its pristine polymers under the same synthesis conditions. However, several limitations can restrict this approach, as will be discussed in this chapter. Common issues include difficulty in synthesizing a pristine polymer with representative properties or the inability to synthesize the material under the chosen conditions, as is the case with PDA.

Considering this and given the striking difference in the synthesis of PEDOT and the copolymer under the same conditions, the polymerization of these materials was analyzed through a comparative study of their deposition kinetics, electrochemical characterization, and morphological changes. Subsequently, the most prominent copolymers were characterized and compared to pristine PEDOT and PDA through compositional analysis, *in-situ* UV-vis spectroscopy, and ellipsometry.

3.2.1 Comparative Analysis on the Electrodeposition of Copolymer and PEDOT Films

Inspired by previous studies on the polymerization mechanism of PEDOT,[142] a similar approach was used to evaluate changes in the polymerization mechanism. As such, the copolymer and PEDOT films were synthesized potentiostatically under 950 mV (*vs.* Ag/AgCl) at different times (40, 160, 240, and 320 s – **Figure 3.10**) following the analysis of their mass deposition during their growth, electroactivity, morphology, and thickness.

As referred to in Chapter 3.1 (during the polymers potentiodynamic growth – **Figure 3.5b**), and represented in **Figure 3.10b**, when compared to the copolymer film, it is evident that PEDOT deposits over the working electrode at a faster rate (disregarding solvent incorporation during deposition, which also influences the recorded mass variation). Nevertheless, the copolymer films presented a comparable electroactivity to PEDOT throughout all deposition times (**Figure 3.10c** and **3.10d**). For a simple and comprehensive interpretation of the deposition times, different regions were lettered from A to D, as described in the following text.

Region A

Region A (0 - 40 s) was considered due to the initial inflection observed during EQCM studies, where the polymer has slower growth and presents a deposited mass of 1.45 μg cm^{-2}. By observing the electrochemical characterization in monomer-free solution, one can effectively identify the predominant characteristics of PDA in the copolymer film. The redox potential of oxidized species registered in **Table 3.2** indicates the presence of quinone/catechol species. Moreover, by integrating the redox peaks corresponding to the catechol/quinone conversion and determining the surface coverage (Equation 2.2, Chapter 2), it presents a considerably high surface coverage of 0.49×10^{-9} mol cm^{-2} when compared to pristine PDA films (in the order of 10^{-11} mol cm^{-2}).[82] This information complements AFM studies **(Figure 3.11)**, which reveal striking differences between the morphology of copolymer film and PEDOT. In **Figure 3.11** (Region A), it can be observed that the copolymer exhibits a uniform and granular topography, similar to the commonly recorded structures for PDA films.[87] Indeed, this granular topography has also been reported for PEDOT with much less uniformity under other synthesis methods.[47,148] Conversely, the PEDOT film in these conditions shows the formation of uneven coils with fiber-like structures.

Another significant difference between these films is their thickness and roughness, as registered in **Table 3.3**. During the deposition time of 40 s, the copolymer and PEDOT films present an approximate thickness difference of 13 nm. This statement reinforces the different deposition rates observed in EQCM. Regarding their roughness, the copolymer film presents an *R*q of 2.7 nm, close to PDA pristine films (*R*q ≈ 3.6 nm).[87] In contrast, the PEDOT film presents much higher values, which are typical for thin films (8.5 nm).[142] Although most of the evidence reveals a strong resemblance to PDA behavior, some traces of PEDOT can be observed in the electroactivity of the film. One can observe a comparable pseudocapacity to pristine PEDOT films and two redox peaks centered at negative potentials *ca.* -211 mV *vs.* Ag/AgCl that can also be attributed to PEDOT.[47]

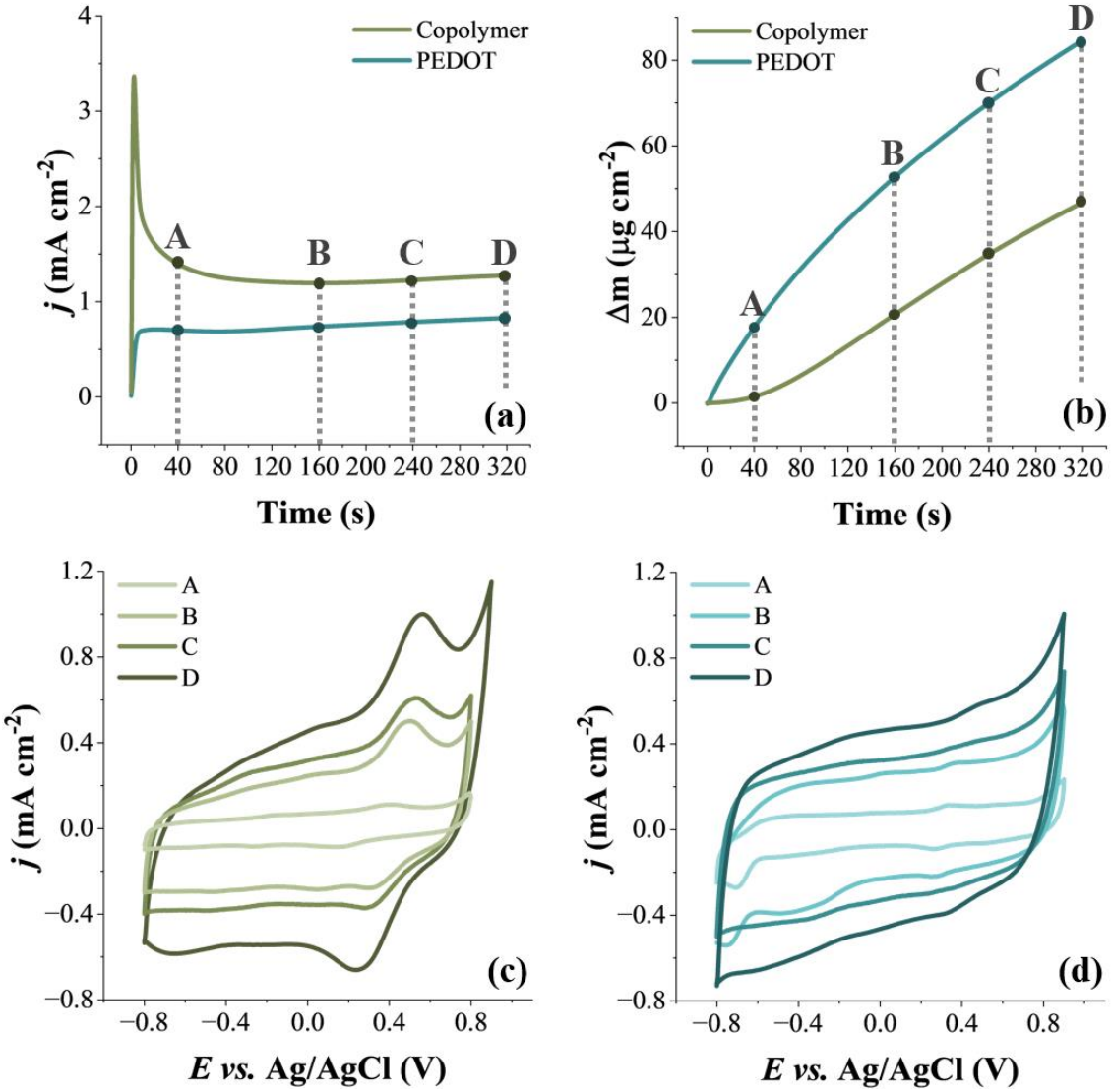

Figure 3.10 – (a) Potentiostatic growth of the copolymer (10 mM DA and 10 mM EDOT) and PEDOT (10 mM) in 50 mM DS at 950 mV (*vs.* Ag/AgCl) for 320 s. (b) EQCM response of copolymer and PEDOT electrodeposition. (c) and (d) 10th characterization cycle of the electrode surface in deoxygenated 50 mM of DS at 50 mV s^{-1} for the deposition of copolymer film and PEDOT, respectively, at 40 s (A), 160 s (B), 240 s (C) and 320 s (D).

Table 3.2 – Electrochemical parameters of the copolymer films (20 mM DA and 10 mM EDOT in 50 mM DS at 950 mV *vs.* Ag/AgCl) deposited with different times with their respective half peak potential of quinone/catechol species ($E_{1/2}$), total charge from the catechol oxidation ($Q_{c/q}$) and corresponding surface coverage of catechol species (Γ_{ox}).

Region	Deposition Time (s)	$E_{1/2}$ (mV *vs.* Ag/AgCl)	$Q_{c/q}$ (mC cm^{-2})	Γ_{ox} ($\times 10^{-9}$ mol cm^{-2})
A	40	275	0.21	0.49
B	160	400	0.67	3.46
C	240	406	0.73	3.79
D	320	420	1.50	7.80

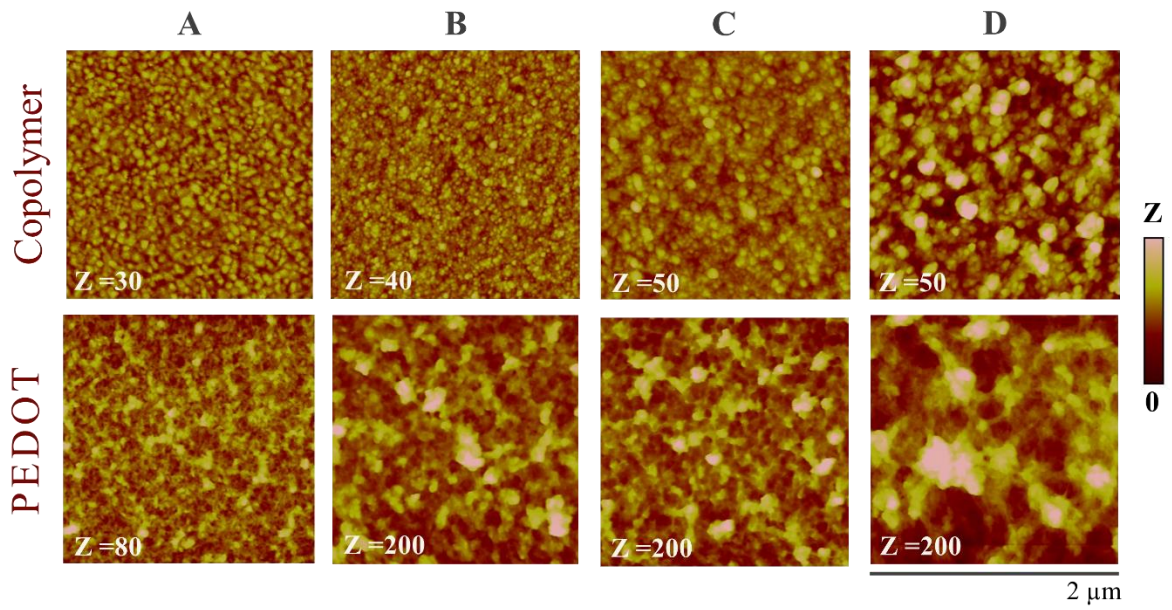

Figure 3.11 – *Ex-situ* AFM morphologic images on the progressive potentiostatic deposition of the copolymer film (20 mM DA and 10 mM EDOT) and PEDOT (10 Mm EDOT) in 50 mM of DS at 950 mV (*vs.* Ag/AgCl) in regions A (40 s), B (160 s), C (240 s) and D (320 s).

Table 3.3 – Roughness (R_q) and thickness (**Figure B3** and **B4** – Appendix B) of the copolymer film (20 mM DA and 10 mM EDOT) and PEDOT (10 Mm EDOT) in 50 mM of DS at 950 mV (*vs.* Ag/AgCl) in regions A (40 s), B (160 s), C (240 s) and D (320 s), estimated by AFM.

Region	Deposition Time (s)	Copolymer		PEDOT	
		R_q (nm)*	Thickness (nm)	R_q (nm)	Thickness (nm)
A	40	2.7	13	8.5	26
B	160	3.3	19	26.8	114
C	240	4.3	24	25.9	136
D	320	12.8	65	36.2	224

* The roughness of the films was estimated with the same films analyzed on Figure 3.11 (2 x 2 µm²)

Region B

After half of the polymerization time (160 s), the hybrid properties of PDA and PEDOT become more evident on the copolymer film. The electroactivity of the PDA/PEDOT copolymer shows not only the quinone/catechol response (**Figure 3.10c** and **Table 3.2**), but also two additional redox processes *ca.* -368 and 53 mV (*vs.* Ag/AgCl). When compared with the response of pristine PEDOT during the same deposition time, one can conclude that these peaks are related to the PEDOT component on the copolymer.

Regarding film morphology, the copolymer keeps a similar granular morphology observed in the initial stages. A slight increase in *R*q is observed, but the film is still alike pristine PDA.[87] In the case of pristine PEDOT films, coalescence occurs, resulting in an increase in globules and thicker fiber-like structures. This is naturally followed by an increase in *R*q. The most surprising difference in this region is the variation in film thickness, where the PEDOT film is about 95 nm thicker than the copolymer.

Region C to D

In the last two regions, the copolymer film exhibits a stronger resemblance to PEDOT. Regarding their electroactivity, both regions originate films with a constant signature – the pseudocapacity and the redox conversion of quinone/catechol species. Even so, the previous redox peaks attributed to PEDOT are attenuated, either in the copolymer or pristine PEDOT films. From the characterization and the analysis on **Table 3.2**, a significant increase in electroactivity is observed from region C to D. In fact, one can conclude that the deposition time that presented the overall highest charge and surface coverage of oxidized hydroquinone species corresponds to 320 s (region D).

The AFM data show significant differences between these two regions. The copolymer morphologies recorded in **Figure 3.11** reveal a decrease in uniformity in the granular film from region B to C. From region C to D, there is an increase and coalescence on the globules, forming a much porous film that resembles pristine PEDOT in region C. These results suggest that, during initial electrodeposition stages, a more compact film is deposited, which progressively becomes more porous. This may relate to the 3D growth of PEDOT, though in a more controlled manner. The initial nucleation processes are followed by the coalescence of nuclei, and then growth in three dimensions. This is supported by the drastic difference observed in *R*q and thicknesses from regions C to D in the copolymer. In fact, this effect is more pronounced in PEDOT films, which show greater differences in morphology, thickness, and *R*q from regions C to D.

By the end of 320 s (point D), the PEDOT film is about 159 nm thicker and has the double of the deposited mass of the copolymer. Nevertheless, their comparable electroactivity cannot be explained by morphological effects. As an initial and straightforward approach to understanding this behavior, the films were evaluated by Electrochemical Impedance Spectroscopy (EIS) in a deoxygenated solution of 1mM $K_3Fe(CN)_6$ and 0.25 M KNO_3. However, the great pseudocapacity of the synthesized films (**Figure B5 –** Appendix B) interfered with the EIS measurements. Consequently, further studies could consider either EIS with a different electrolyte or perform *in-situ* conductivity measurements.

3.2.2 Physicochemical Characterization of Selected Copolymer Films

Given the changing electrochemical and morphological properties of the copolymer during film synthesis, two different copolymers were chosen to assess their physicochemical properties and understand how they differ from each other and from pristine PEDOT and PDA.

Based on the presented results, the characterization of the films focused on two main aspects: the possibility of depositing a film with varying composition and the monitoring of morphological changes over different synthesis times. Notwithstanding, their hybrid properties in relation to pristine polymers require further approaches using additional characterization techniques. For these studies, two copolymers were selected: the 160 s film (region B), due to its similarity to PDA, and the 320 s film (region D), because of its resemblance to PEDOT.

3.2.2.1 Chemical Composition Studies

The selected copolymer films were first analyzed by FTIR to evaluate the presence of specific chemical structural groups. Additionally, pristine PDA and PEDOT films were synthesized for comparative effects. In the case of PEDOT, the film was electropolymerized potentiostatically with 10 mM EDOT in 50 mM DS at 950 mV (*vs.* Ag/AgCl) for 320 s. As for the pristine PDA polymer, it was synthesized through a potentiodynamic synthesis in 5 mM DA (from -600 to 800 mV *vs.* Ag/AgCl) during 50 cycles

in CPB (pH = 7), obtaining a film with about 20 nm.[87] After their synthesis and analysis, these were compared and represented in **Figure 3.12**.

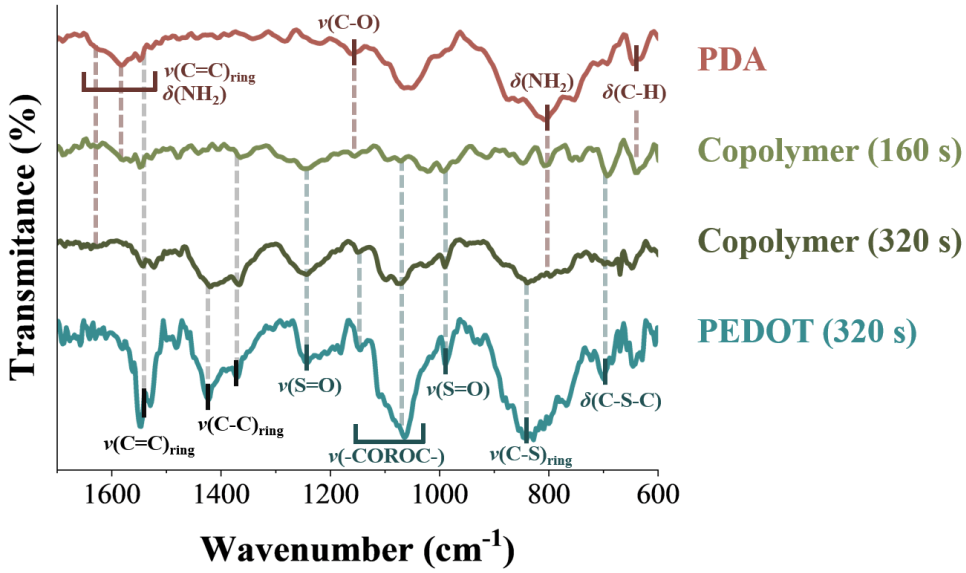

Figure 3.12 – FTIR reflectance spectra of gold Arrandee surfaces modified with PDA(potentiodynamic synthesis in 5 mM DA from -600 to 800 mV (*vs.* Ag/AgCl) through 50 cycles in CPB, pH = 7)[87], PEDOT (10 mM EDOT) and copolymer films (20 mM DA and 10 mM EDOT) in 50 mM DS at 950 mV for 160 and 320 s of electrochemical deposition. The *ν* and *δ* stand for their bending and stretching vibration modes, respectively.

Despite the complexity of the fingerprint region and the lower resolution achieved for the copolymers using the FTIR reflectance mode, the peaks from the copolymers were assigned based on their compatibility with the pristine PDA and PEDOT peaks (**Table B1** and **B2 –** Appendix B).[87,150–153] In the first analysis, slight differences are noticeable between PDA and PEDOT pristine films, while the copolymer films exhibit both chemical functionalities. Although the spectrum confirms the formation of a hybrid material in both cases, the 160 s copolymer is more compatible with the PDA spectrum, while the PEDOT traces appear with relatively lower transmittance (when compared to the copolymer with 320 s). Conversely, the copolymer grown with 320 s reveals a stronger relationship with PEDOT spectrum and lower transmittance of PDA characteristic bands.

When one looks closely into the aromatic vibrations, from 1650 to 1550 cm^{-1}, interesting differences are observed in all polymers. Pristine PDA and the copolymer (160 s) present higher wavenumbers related to a doubly generated asymmetric C=C stretching and NH_2 bending.[82,87] However, at lower wavenumbers one can observe the C=C stretching of the thiophene ring in the spectrum of PEDOT and the copolymer (320 s).[152] These results prove changes in the aromaticity during copolymer deposition and agree with the previous step-wise analysis of the film synthesis.

Because of the difficulties in identifying signals within the fingerprint region, Raman spectroscopy was employed as an alternative to improve the differentiation of signals associated with the most characteristic functional groups. Furthermore, Raman has been reported in the literature as interesting spectroscopic technique for *in-situ* analysis to track structural changes in PEDOT during reduction and oxidation.[152,154–156] The spectra obtained for pristine and copolymer films are represented in **Figure 3.13**. Additionally, the most representative PEDOT signals, also found in the copolymer films, are listed in **Table 3.4**.

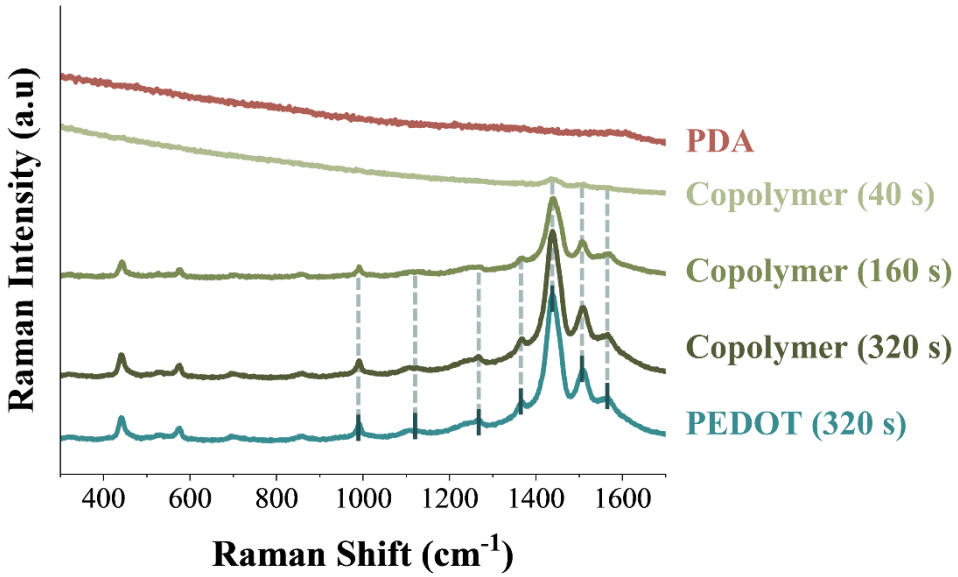

Figure 3.13 – Raman spectra of gold Arrandee surfaces modified with (potentiodynamic synthesis in 5 mM DA from -600 to 800 mV (*vs.* Ag/AgCl) through 50 cycles in CPB,pH = 7)[87], PEDOT (10 mM EDOT) and copolymer films (20 mM DA and 10 mM EDOT) in 50 mM DS at 950 mV for 40, 160 and 320 s of electrochemical deposition.

Table 3.4 – Band assignments for the main vibrations in the Raman spectra of electrodeposited PEDOT and copolymers.[152]

Raman Shift (cm^{-1})	Assignments
991	Oxyethylene ring deformation
1111	C–O–C deformation
1266	C_{α}– $C_{\alpha'}$ stretching
1369	C_{β}– C_{β} stretching
1438	Symmetric C=C stretching
1510	Asymmetric C=C stretching
1568	Bipolaron structure

As observed, the copolymer films of 160 and 320 s show a significant overlap with the pristine PEDOT film. However, these results are difficult to compare with the Raman spectra of PDA, since its spectrum exhibits strong fluorescence interference, as previously studied in our group.[157] To account for this effect, thinner copolymer films (40 s) were synthesized to evaluate whether the interference was also present. Indeed, when the film is deposited at shorter times, both fluorescence interference and PEDOT contributions can be observed in the bands at 1438, 1510, and 1568 cm^{-1}. This outcome may suggest that PDA is mainly located in the innermost layers of the film, which is not supported by the electrochemical studies, where the coverage of catechol moieties increase with deposition time. Nevertheless, these results are only qualitative, and one must also consider the contribution of the Raman signal from the electrode surface. Therefore, further studies on film composition are necessary. One possible alternative for this purpose is XPS.

Water contact angle measurements were also performed to provide more information about the chemical environment at the interface of the modified electrodes. Although one might expect a hydrophobic character from PEDOT, results showed a θ_{WCA} of 40.60 ± 1.42º (thickness 224 nm). This result is related to the influence of polymer doping with DS, whose chemical structure favors molecular interactions with water, as previously demonstrated with PSS (*e.g.* PEDOT:PSS – 33º and PEDOT:PSS/PEDOT (20mC) – 73º).[158] For the copolymer films, a water contact angle of 36.93 ± 0.55º was observed for the film deposited after 160 s (thickness 19 nm) and 27.04 ± 0.85º for the one synthesized with 320 s (thickness 65 nm). Considering the thickness and the quinone/catechol surface coverage estimated for copolymers, (**Table 3.2 and 3.3)**, it is logical to expect that a higher quantity of PDA-related species in the film is reflected in a lower contact angle. Thus, in addition to the effect of the incorporated electrolyte, this suggests that, although PDA may be more concentrated in the first layers, DA moieties are also present in the outermost layers of the film.

3.2.2.2 Optoelectronic and Dielectric Properties

The spectrochemical analysis of conjugated polymers provides valuable information about their electronic structure.[159] Indeed, it has been proven that conducting polymers suffer meaningful optical changes during doping in the UV-vis and Near-IR regions (UV-Vis-Near-Infrared Region) originating from changes in their electronic structure.[160] One of the polymers that is frequently studied in the literature because of its interesting spectrochemical behavior is PEDOT. [152,161] Considering how relevant this feature is in PEDOT, we explored the resulting properties observed on the copolymer.

The polymerization process of the films was also followed by *in-situ* reflectance UV-vis spectroscopy to provide insights into their synthesis. In the case of PDA, it was polymerized following the same synthesis method referred to in FTIR analysis.[87] As represented in **Figure 3.14a**, the potentiodynamic synthesis was progressively followed after each three cycles. The most representative shoulder can be observed initially at 470 nm, which later suffers a blue shift to 450 nm, attributed to the formation of indoline species near the electrode surface. [82,87]An additional signal at lower wavelengths than 300 nm is related to aromatic rings in PDA. Both signals progressively decrease in reflectance with potential cycling, indicating the deposition of the polymeric material.

The potentiostatic synthesis of PEDOT and the copolymer films were followed every 20 s, applying a potential of 950 mV (*vs.* Ag/AgCl) as represented in **Figures 3.14b** and **3.14c**, respectively. In the case of PEDOT (**Figure 3.14b**), a decrease in reflectance is observed from 455 to 700 nm. This deposition profile has been understood in the literature as conjugation breaks in the PEDOT chains during its progressive doping process.[160] In the copolymer deposition (**Figure 3.14c**), one can find a hybrid spectrum with characteristics from PDA and PEDOT. A reflectance peak is observed around 400 nm, presenting a similar profile to the one observed in PDA with a slight blue shift. On the other hand, a small reflectance shoulder can be observed at around 550 nm and attributed to PEDOT. Additionally, a lower decrease in reflectance is recorded in the copolymer when compared to PEDOT, which might correspond to a lower doping degree. The spectroscopic differences during the electrosynthesis of the PDA/PEDOT copolymer suggest that changes in the chemical environment influence the polymerization process, leading to the formation of different oligomeric forms that could arise from the chemical binding between the two monomers. However, further studies are needed to understand and confirm this effect.

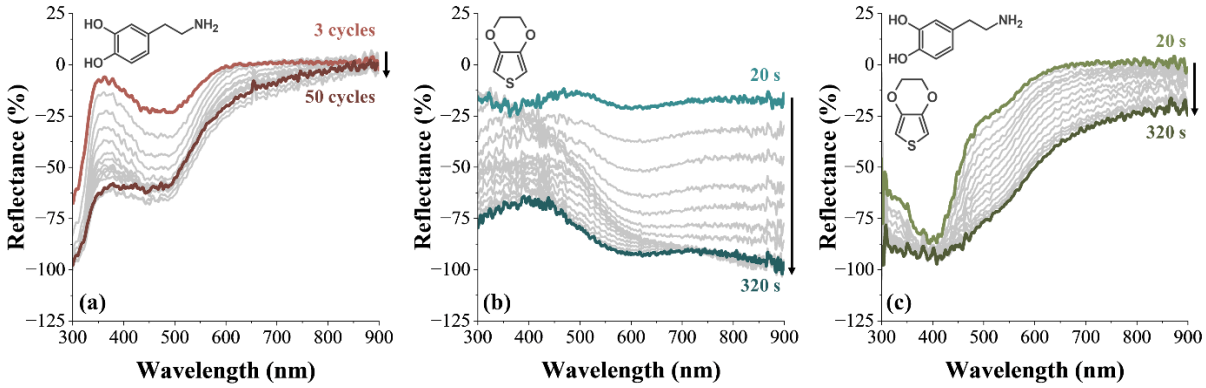

Figure 3.14 – *In-situ* reflectance spectra during the electrosynthesis of (a) PDA (potentiodynamic synthesis in 5 mM DA from -600 to 800 mV (*vs.* Ag/AgCl) through 50 cycles in CPB, pH = 7)[87], (b) PEDOT (10 mM EDOT) and (c) copolymer film (20 mM DA and 10 mM EDOT) in 50 mM DS at 950 mV *vs.* Ag/AgCl.

After the electrochemical deposition, the films were characterized in 0.1 M $NaClO_4$ by applying potentiostatic pulses ranging from -800 to 800 mV (*vs.* Ag/AgCl) (**Figure 3.15**). The pure PDA film exhibits minimal spectral variations, with the applied potentials (**Figure 3.15a**). Nevertheless, a slight peak around 569 and 599 nm can be recorded and assigned to the response of the PDA backbone.[162] In the case of the PEDOT film, a typical spectrum variation can be seen (**Figure 3.15b**).[163] When the polymer is reduced, a wide reflectance band can be recorded from 390 to 700 nm. This band is referred to in the literature as π-π* transitions of neutral PEDOT fragments.[154,156] With the oxidation of the film, this band suffers progressive small shifts and decreases in intensity. Simultaneously, an emerging band increases significantly upon oxidation at higher wavelengths (> 600 nm). This band is usually associated with the charge carrier bands and their evolution to the polaron and bipolaronic bands.[159] Finally, at approximately 100 mV (*vs.* Ag/AgCl), the isosbestic point is observed at 722 nm, confirming the gradual transformation of the neutral PEDOT polymer into the conductive one for higher potentials.[155]

In the case of copolymer films (**Figure 3.15c** and **3.15d**), evident characteristics resembling PEDOT behavior can be seen. During their reduced state, a similar reflectance peak to PEDOT can be observed in both spectrums from 450 nm to 750 nm, although with different intensities. Evident changes emerge in the peak profile when the PDA/PEDOT copolymers are oxidized. Changes in PEDOT spectrum – blue shifts, band broadenings, and intensity changes in oxidation transitions – generally suggest changes in the conducting polymer regarding its conjugation and structure. As reported in the literature, this indicates that the average conjugation length of PEDOT has been affected, presenting shorter π-conjugations.[156,164] In this case, this possibly corresponds to polymeric chains of alternating DA and EDOT monomers, where the presence of PDA chains disrupts the conjugation of PEDOT.

There are remarkable spectral differences when copolymers prepared with distinct deposition times (160 and 320 s) are compared. Although the hybrid behavior of PDA and PEDOT is observed in both copolymer films, their different characteristics are reflected in their oxidation state. In the 160 s deposition, one can observe a broader peak with lower intensity and a blue-shifted oxidation peak, with the band starting from 565 nm. This can be attributed to the higher contribution of the PDA character to the film, forming a significantly less conductive material. On the other hand, the copolymer deposited for 320 s has a reflectance spectrum with a similar PEDOT behavior. Even so, higher intensities, peak broadening, and a blue shift starting at 525 nm confirm the influence of PDA in the copolymer film. In both copolymers, the isosbestic point is recorded after 200 mV *vs.* Ag/AgCl. In the copolymer with 160 s of deposition, the isosbestic point starts *ca.* 655 and shifts to 595 nm. For the copolymer with 320 s, it appears at approximately 660 nm and shifts to 630 nm. This behavior confirms the gradual transformation of the copolymer from the neutral phase to the conductive one, as observed in PEDOT.

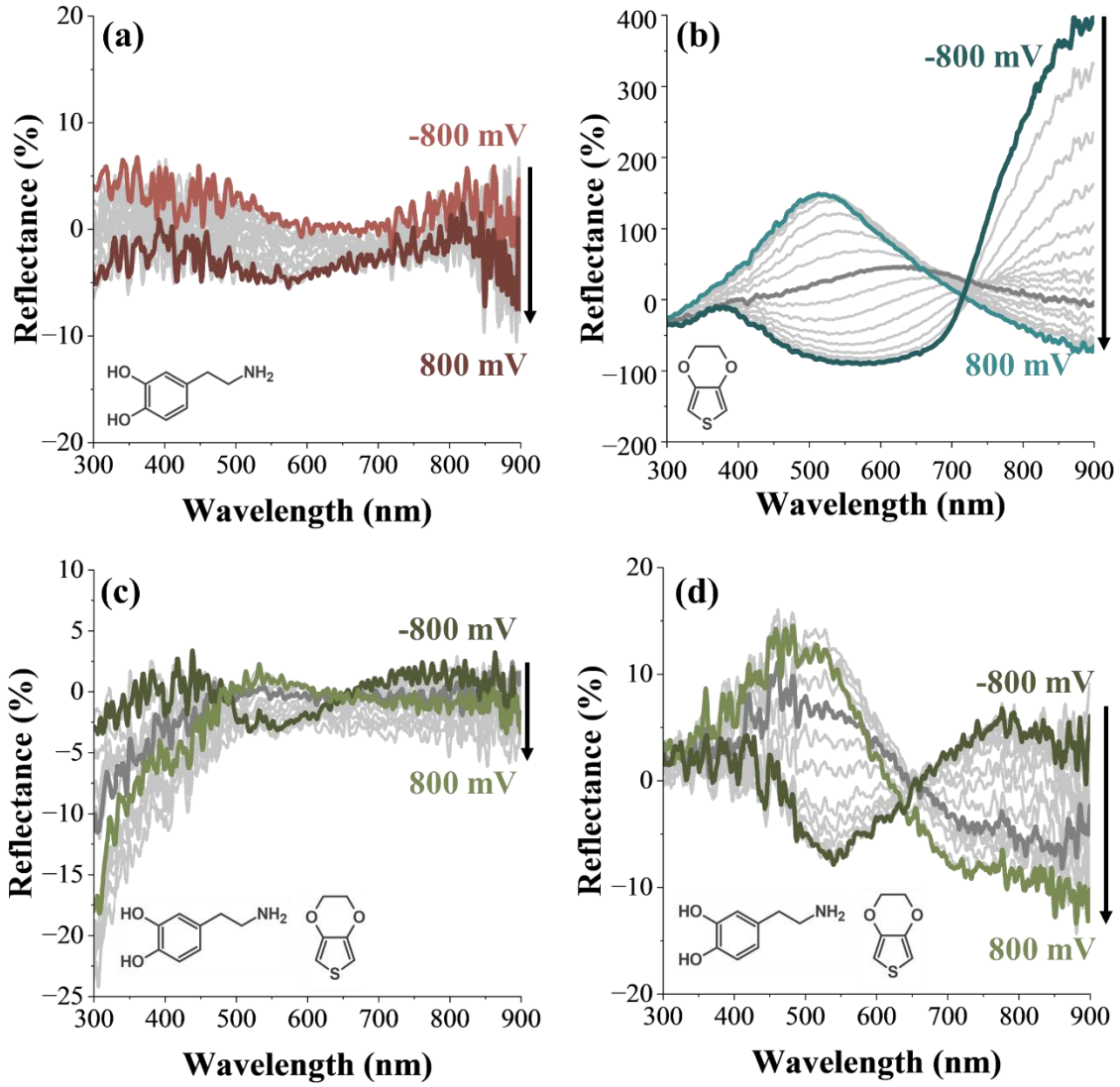

Figure 3.15 – *In-situ* UV-vis reflectance spectrum of (a) PDA (potentiodynamic synthesis in 5 mM DA (from -600 to 800 mV *vs.* Ag/AgCl) during 50 cycles in CPB ,pH = 7)[87], (b) PEDOT (10 mM EDOT) and copolymer films (20 mM DA and 10 mM EDOT) for (c) 160 and (d) 320 s at different chronoamperometric potentials (from -800 to 800 mV *vs.* Ag/AgCl) in 0.1 M $NaClO_4$.

After the spectroscopic analysis of the polymeric films, these were analyzed based on their ellipsometric parameters. It is well known that, at the working wavelength of the ellipsometer (632.8 nm), the extinction coefficient (k) of PEDOT changes as a function of potential.[165] This can also be observed during the characterization of the polymer in **Figure 3.15b**. However, for the copolymers, the isosbestic point occurs near the same wavelength as the ellipsometer. Therefore, slight variation of k is observed in the potential window. Considering that the conductivity of the copolymers was not compromised with the applied potential, these were studied with *ex-situ* ellipsometry. Thus, the measured and estimated values are represented in **Table 3.5**.[c]

[c] Note that the thickness value estimated for PEDOT films with ellipsometry presents a difference of about 55 nm when compared with AFM. This difference and the higher error recorded in Table 4.5 is related to the dispersion of the recorded experimental ellipsometric parameters, commonly observed in thicker and non-uniform films.[166]

Table 3.5 – *Ex-situ* ellipsometry of the modified electrodes with the potentiostatic (950 mV *vs.* Ag/AgCl) deposition of PEDOT (10 mM EDOT) and copolymers (20 mM DA and 10 mM EDOT) and their respective refractive index (n), extinction coefficient (k) and thickness (L). The values are represented as mean ± standard deviation.

Film	n	k	L (nm)
PEDOT (320 s)	1.36 ± 0.02	0.229 ± 0.001	279 ± 27
Copolymer (160 s)	1.50 ± 0.01	0.077 ± 0.005	24 ± 1
Copolymer (320 s)	1.45 ± 0.01	0.171 ± 0.007	64 ± 1

The refractive index of the copolymer films confirms the formation of more compact matrices compared to the conducting polymer. However, when the refractive index of a PDA film with *ca.* 20 nm is considered (n = 1.75),[87] the influence of PEDOT can be recognized in the copolymer. On the other hand, when the copolymers are compared with each other, a slightly higher index is observed for the deposition of 160 s, which indicates a greater influence of PDA. Additionally, the increase in the refractive index from 160 to 320 s further confirms the initial deposition of a more compact film and its progressive change to a less compact material.

The extinction coefficient is considerably superior in the PEDOT film than in the copolymers, indicating greater aromaticity and conductivity. Nevertheless, these values are still significantly superior when compared to the ones recorded in the literature for pure PDA films ($k \leq 0.05$).[87] Between the copolymers, higher values of k were recorded for the deposition of 320 s, corresponding to a polymer with a greater PEDOT composition. Finally, the thickness of the films was estimated. These results are in agreement with AFM images, which show a significant difference in thickness between the copolymer and PEDOT when both materials are electrosynthesized under the same conditions.

Overall, *in-situ* UV-vis reflectance spectroscopy and ellipsometry were fundamental techniques to gain deeper insight into the polymerization process and the hybrid properties of the copolymers. These studies confirmed that both copolymers behave as conducting polymers, showing that the insulating character of PDA does not compromise their conductivity. At the same time, the reflectance spectra recorded during film deposition pointed toward the formation of intermediate DA-EDOT oligomeric species that later give place to the copolymer. Finally, the analysis of the ellipsometric parameters indicated the deposition of a more compact film with lower PEDOT content at shorter times, which evolves into a more porous film with progressively higher PEDOT contribution. All these results are consistent with electrochemical characterization, EQCM, AFM, and compositional studies.

Chapter 4

Potentiostatic and Galvanostatic Charge and Discharge Tests

"Electrochemistry is the science whereby electricity makes things and things make electricity"

John O'M. Bockris

4. Potentiostatic and Galvanostatic Charge and Discharge Tests

After the development and characterization of the PDA/PEDOT copolymer, the material was tested for its intended purpose: as a cathode material for sodium-ion batteries. Electrochemical methods are the common choice for battery testing, as they allow the direct collection of fundamental parameters such as voltage, capacity, and cycling stability. Among these, cyclic voltammetry and galvanostatic cycling are the most widely used, since they provide information on the voltage and energy profiles of the materials under quasi-steady state conditions. Other electrochemical techniques, such as potentiostatic cycling and EIS, are less common but are also employed to fully characterize electrode materials as they serve to provide mechanistic insights on ion diffusion and electrode degradation.[167,168]

During this dissertation, galvanostatic and potentiostatic charge/discharge were used to evaluate the performance and cycling stability of the copolymer. Initially, thin PDA/PEDOT copolymer and pure PEDOT films were tested under potentiostatic cycling coupled with EQCM to gain insights into the kinetics and possible degradation of the films. Later, thicker films were grown and characterized on graphite electrodes to provide a more sustainable and scalable approach. Finally, the materials were tested for charging/discharge cycles under potentiostatic and galvanostatic control, which allowed the evaluation of their charge retention and other relevant parameters.

4.1 Half-Cell Potentiostatic Tests

When cycles of potentiostatic charge/discharge trials are performed, two constant potential values that provoke the respective insertion and removal of the ion are selected and applied under an appropriate time. The response to this perturbation is given by the recorded current response, producing a profile as the one represented in **Figure 4.1a**. When these potential pulses are coupled with EQCM, a frequency variation is observed, as shown in **Figure 4.1b**. These studies are relevant to track variations in frequency that can suggest an extent of a possible degradation of the material during potentiostatic cycling.

In the case of the copolymer and PEDOT, when the film is oxidized, a positive current is recorded, indicating that PDA presents its quinone moieties and that PEDOT carries a positive charge, compensated by the immobilized anion, in this case DS. This process is accompanied by a decrease in frequency (or increase in mass) due to the incorporation of anions (and/or expulsion of cations), which also compensate the charge of PEDOT, and the solvent, which enters the polymeric matrix. The insertion of these species leads to mechanical changes within the polymer.

When the film is reduced, a negative current is recorded, PDA can coordinate with sodium ions, and the PEDOT backbone becomes neutral, meaning that the immobilized dopant can balance its charge with the incorporated sodium ions. During this process, an increase in frequency (or decrease in mass) is observed, indicating that cations are inserted and/or anions are expelled along with the solvent, causing the polymer to experience mechanical changes. It is important to note that this description is a simplification to explain the cycling of polymeric films and does not necessarily reflect the exact sequence of processes.[45,123]

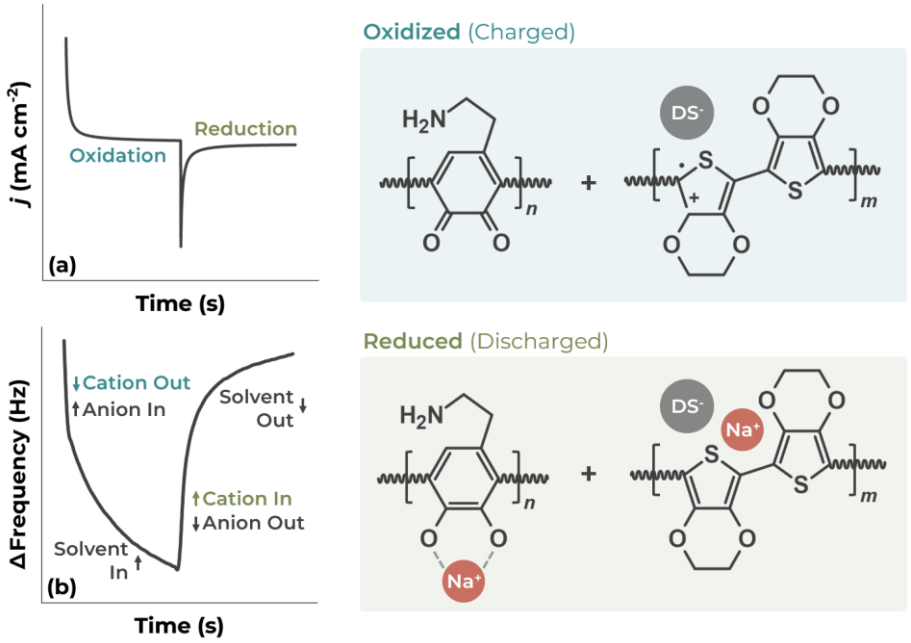

Figure 4.1 – Representation of (a) potentiostatic pulses response during a charge/discharge cycle and (b) the corresponding flux when coupled with EQCM, with a tentative illustration of the ion interaction between oxidation and reduction of the polymeric films.

Given the low molecular weight of sodium ions incorporated compared to the molecular weight of the selected anion and the solvent flux, no direct conclusions on the incorporation of the sodium ion can be made only from mass changes. For this type of approach, more complex techniques such as Probe Beam Deflection (PBD) should be considered to understand and attribute the fluxes at the interface to each corresponding species (*i.e.,* anion, ion, solvent).

To select appropriate potentials for battery charge/discharge trials, the chosen potentials should avoid parasitic reactions while allowing the full redox conversion of the polymeric material. As shown in **Figure 4.2**, the potentials selected for potentiostatic cycling were -600 mV and 700 mV (*vs.* Ag/AgCl). The red-shaded zones were excluded due to the risk of side reactions that could degrade the material during battery cycling.

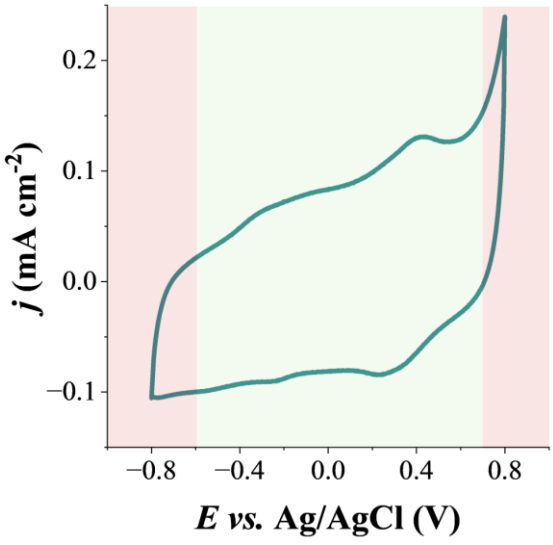

Figure 4.2 – Cyclic voltammogram in $NaClO_4$ (0.1 M) at 10 mV s^{-1} of the copolymer synthesized under 950 mV (*vs.* Ag/AgCl) for 320 s in 50 mM DS.

4.1.1 Thin Film Charge/Discharge Cycles Coupled with EQCM

For the first cycling tests, the films were synthesized over a gold EQCM electrode. Due to experimental limitations, both the copolymer and PEDOT films were grown with a mass of 10.43 µg cm^{-2} (assuming the applicability of the Sauerbrey equation) to ensure equivalent deposited masses and proper vibration of the microbalance during battery cycling.[d] This required the films to grow under 950 mV (*vs.* Ag/AgCl) in 50 mM DS, with deposition times of 95 s for the copolymer and 20 s for PEDOT. After synthesis, the films were cycled in 0.1 M $NaClO_4$, applying -600 mV and 700 mV (*vs.* Ag/AgCl) for 5 s per pulse over 1000 cycles.

The charge and discharge pulses (50 to 100 cycles) of the potentiostatic cycles for PEDOT and the copolymer are represented in **Figure 4.3**. As observed, both films in **Figures 4.3a** and **4.3b** show a regular current response during these cycles. On the other hand, the frequency variations recorded with EQCM are presented in **Figures 4.3c** to **4.3f** for the initial cycles (50 to 100) and for the final cycles (950 to 1000), corresponding respectively to PEDOT and the copolymer. In all presented cases, a drift can be observed, which corresponds to the response of the microbalance, likely related to local thermal oscillations caused by the elevated flux of charge required for these assays.

In **Figure 4.4a** and **4.4b**, a zoomed-in transient of the oxidation of the PEDOT and copolymer films, respectively during the 50th and 1000th cycle, is represented. It can be observed that in both films the charge and discharge reach nearly 100% within a very short time. For PEDOT, this process takes about 0.15 s, while for the PDA/PEDOT copolymer it takes 0.25 s, reflecting the higher density of the copolymer film (increased diffusion constraints). Regarding their mass variation, **Figure 4.4c** and **4.4d** show the expected mass response after 1000 cycles, although the frequency oscillations observed in the copolymer film may indicate that the material is not yet fully stabilized.

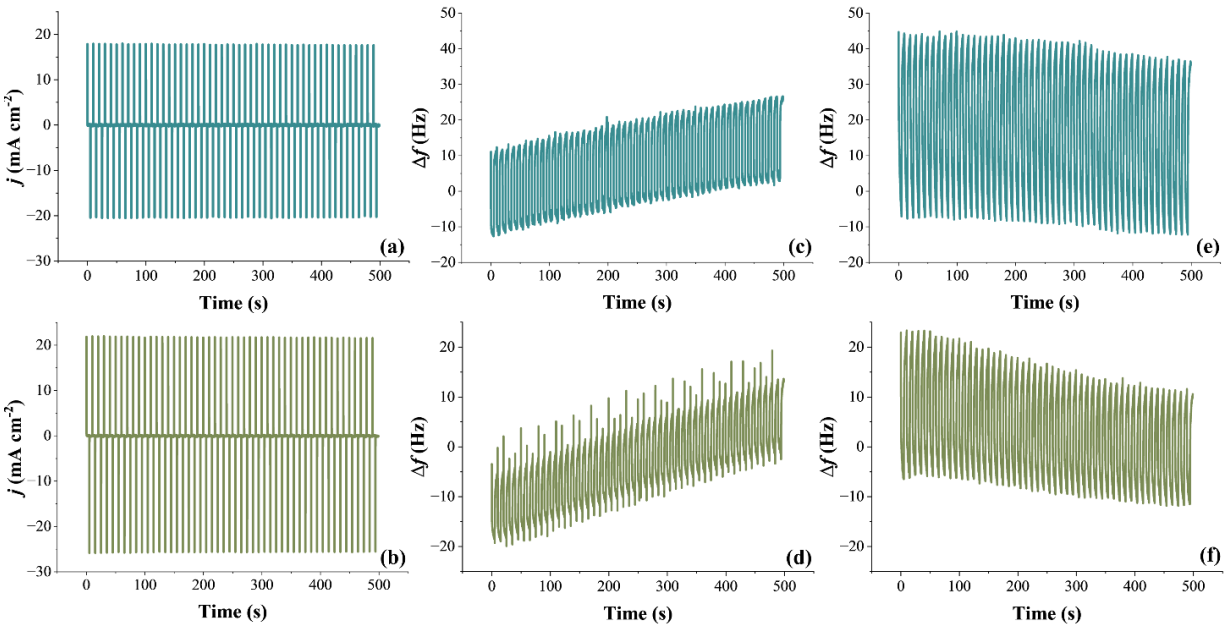

Figure 4.3 – (a) and (b) Variation of current density film during of the potentiostatic charge and discharge (from 50 to 100 cycles) under 700 mV and -600 mV (*vs.* Ag/AgCl) for 5 second pulses. (c) and (d) Frequency variation from 50 to 100 cycles and (e) and (f) from 950 to 1000 cycles of PEDOT and copolymer films, respectively.

[d] For thick films the EQCM quartz crystal stops vibrating during the long potential cyclic assays. Thus, the films were grown within an adequate mass range to follow frequency variations during charge and discharge cycles.

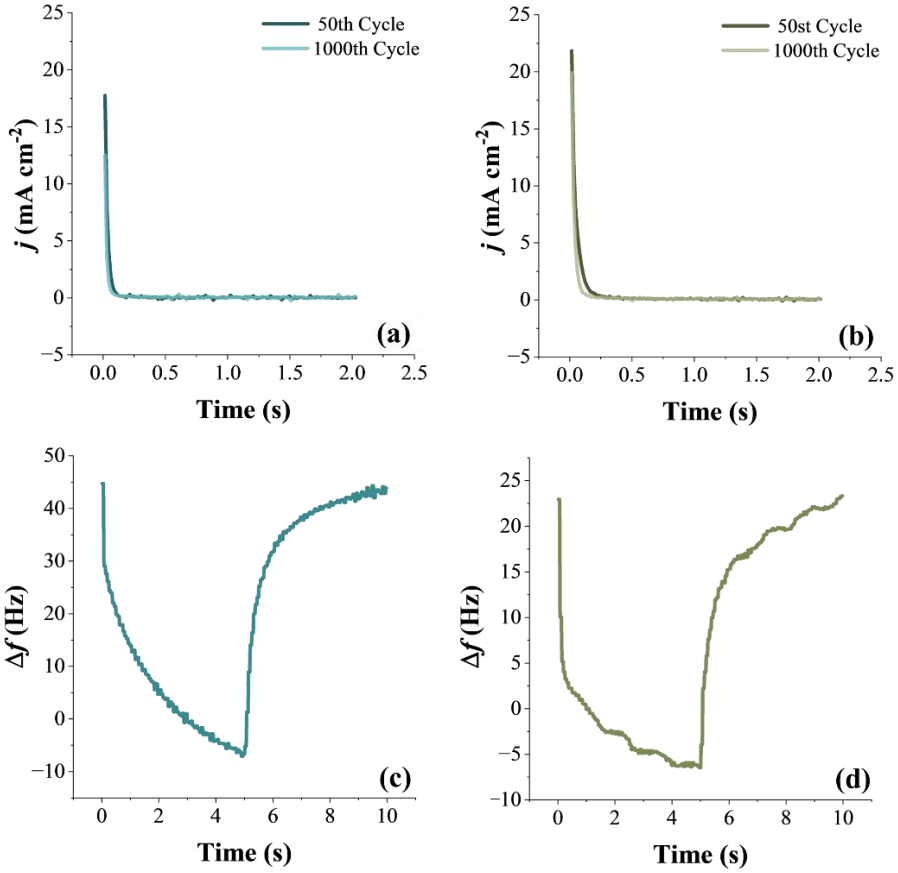

Figure 4.4 – Zoomed-in oxidation transient during the 50th and 1000th cycle of (a) PEDOT and (b) copolymer films. Frequency variation of the last cycle of (c) PEDOT and (d) copolymer films.

When their specific capacity is calculated and compared considering the deposited mass, (knowing that a great contribution comes from capacitive current) the copolymer shows an initial specific capacity of 29 mAh g^{-1}, while PEDOT presents 13 mAh g^{-1} (**Appendix C**). Nevertheless, after 1000 cycles, the copolymer suffers decrease of 33% in capacity retention, reaching a final capacity of 19 mAh g^{-1}, whereas PEDOT exhibits a lower degradation of 16% with a final capacity of 11 mAh g^{-1}. These variations, followed through battery cycling, are represented in **Figure 4.5a** and **4.5b**. Thus, it is possible to conclude that the copolymer presents the best capacity in these conditions, allowing batteries with lower weight and higher energy delivery than pristine PEDOT films. However, when the stability of the battery is considered, PEDOT polymers present a better performance.[e]

Considering the mass variation during cycling, under these conditions both films showed a significant mass increase. For PEDOT, the increase was 110 % from the initial recorded mass, while for the copolymer it reached 136 %. These results suggest that the PDA/PEDOT copolymer undergoes greater mechanical deformations, which is later reflected in the stability of the material. From **Figure 4.4b** and **4.5**, it becomes pertinent to perform additional cycles to monitor the stabilization of both materials while coupling this analysis with other techniques, such as PBD, to obtain more conclusive observations.

[e] These calculations were considered from the 50th cycle for a more stable capacity and to avoid a drastic capacity decay.

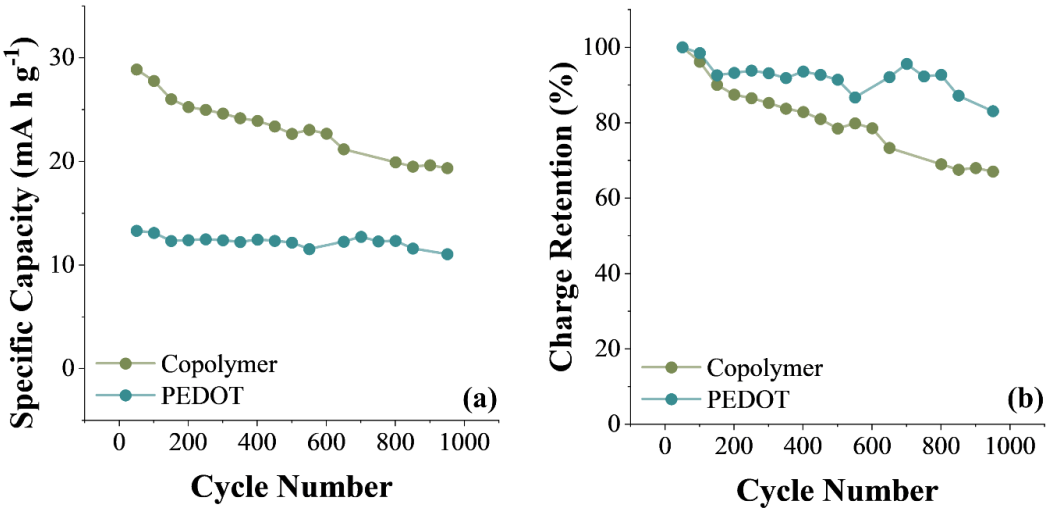

Figure 4.5 – Comparison of the (a) specific capacity and (b) charge retention in EQCM gold electrodes during battery cycling in 0.1 M $NaClO_4$ for 1000 cycles.

4.1.2 Potentiostatic Charge/Discharge Cycles with Graphite Electrodes

To study the battery cycling of the polymers with thicker films and a higher number of cycles, the electrode material was changed to graphite for a more cost-effective and sustainable approach. Due to practical issues related to the use of characterization techniques, the electroactivity, morphology, and thickness of the films were first evaluated on glassy carbon electrodes. In these tests, the parameter chosen to compare the electrodes as cathode materials was, as in the previous case, their deposited mass. For this purpose, the PDA/PEDOT copolymer film was grown for 320 s, while the PEDOT film was synthesized for 135 s under 950 mV (*vs.* Ag/AgCl) in 50 mM DS, both reaching a mass of approximately 46 µg cm^{-2}.[f] The potentiostatic synthesis and the characterization of the films has been represented in **Figure D1** (Appendix D), presenting a similar electroactivity as the one observed in polycrystalline gold electrodes.

After electrochemical characterization, the morphology of the films was studied and represented in **Figure 4.6**. As in the case of the gold electrodes described in Chapter 3.1, PEDOT films present a more porous and uneven coil-like structure (**Figure 4.6a**). In contrast, the copolymer film shows a more uniform, more compact and granular morphology (**Figure 4.6b**). The thickness of the films was also analyzed by exposing the electrode surface through a thin scratch with paper, allowing the estimation of the average thickness of the films, as represented in **Figure 4.7**.

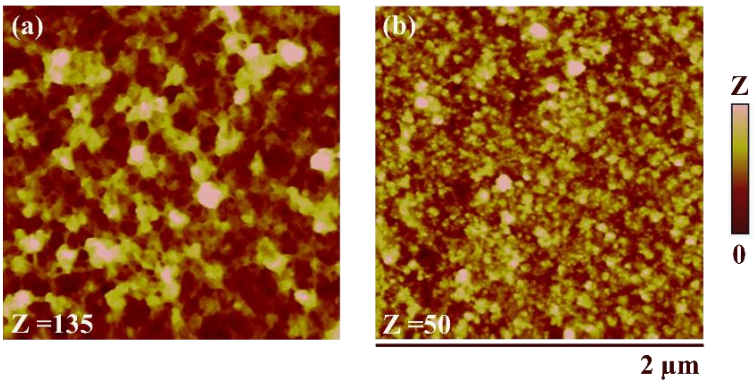

Figure 4.6 – AFM morphologies of (a) PEDOT film grown for 135 s and (b) copolymer grown for 320 s over a GC electrode.

[f] This was estimated with previous studies performed with EQCM (Chapter 3.2).

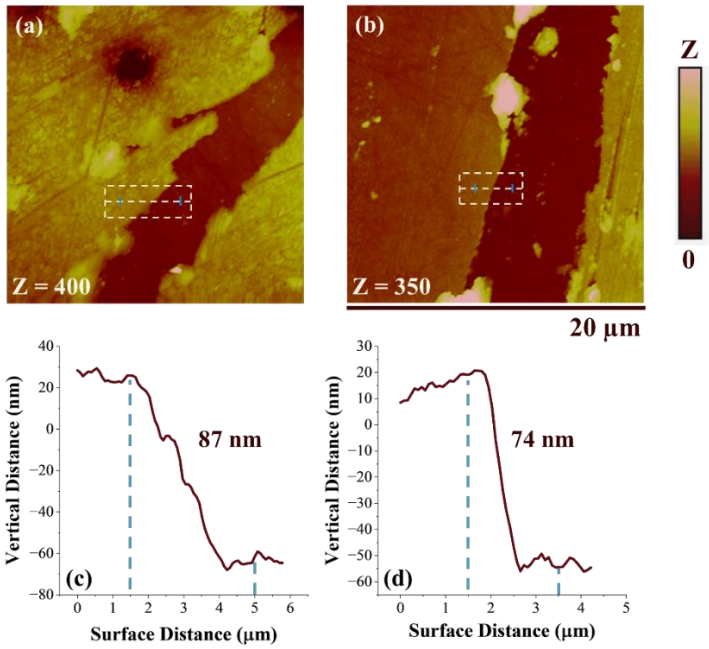

Figure 4.7 – AFM topographic images of (a) PEDOT and (b) copolymer deposited over a GC electrode with their respective height profiles in (c) and (d).

Given the comparable properties of the polymers deposited on polycrystalline gold and glassy carbon electrodes, the films were synthesized over graphite electrodes[g] (**Figure D2** – Appendix D). After their synthesis, the films were charged and discharged in 0.1 M $NaClO_4$, applying -600 mV and 700 mV (*vs.* Ag/AgCl) for 5 s per pulse over 1500 cycles. As in the case of the previously referred thin films, the pulses during the cycles of both films (not represented) showed stable currents. The zoomed-in oxidation transients of PEDOT and the copolymer of the 50th and 1500th are represented in **Figure 4.8**, where a fast charge can be observed. In this case, the process takes ~ 2 s in both polymeric films.

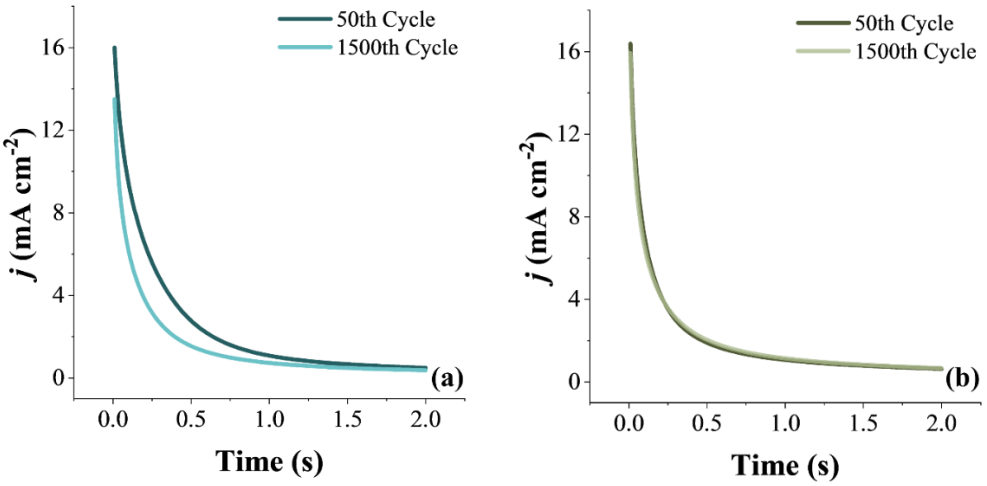

Figure 4.8 – Zoomed-in oxidation transient during the 50th and 1000th cycle of (a) PEDOT and (b) copolymer films.

[g] This approximation was adopted as a simpler and more accurate method to measure the thickness with AFM, by first scratching the GC electrodes with the edge of a paper sheet to expose the underlying surface, allowing the measurement of the height profile.

Further analysis of these data allowed to determine the specific capacity of the polymer films (**Appendix C**) and compare their evolution during cycling, as shown in **Figure 4.9**. At the beginning of the battery cycles, the PEDOT film presented a specific capacity of 33 mAh g^{-1} while the copolymer film presented 30 mAh g^{-1}. This difference, when compared to thin films, is possibly related to the different morphologies of the polymers. Since PEDOT films are more porous, the deposited mass might not compensate the different internal area, presenting a higher capacity. In the case of the copolymer, which is more compact, these differences can be more standardized, presenting similar values to the one observed with thin films.

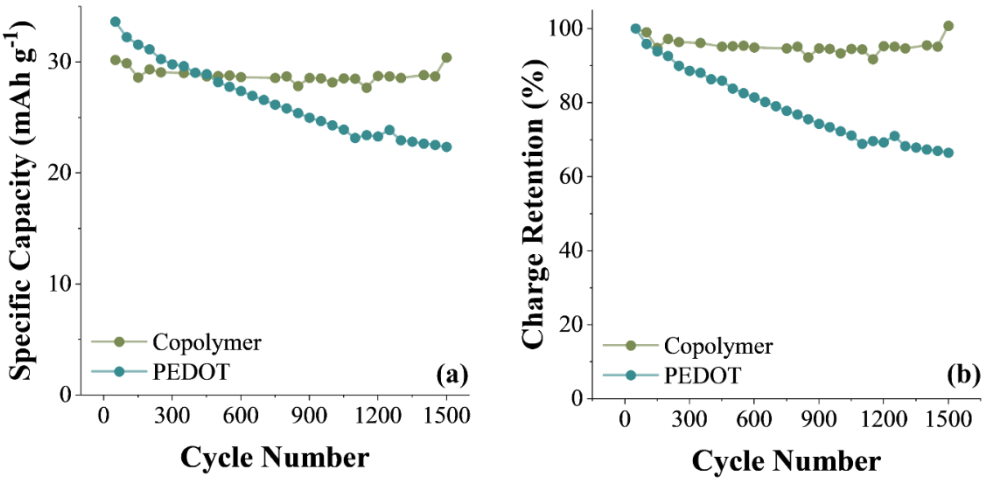

Figure 4.9 – Comparison of the (a) specific capacity and (b) charge retention of PEDOT and copolymer films deposited on graphite electrodes during modified electrode charge/discharge cycling in 0.1 M $NaClO_4$ for 1500 cycles.

Despite the higher initial capacity of PEDOT, after 1500 cycles the polymer suffered a decrease of 34 %, presenting a final capacity of 22 mAh g^{-1}. In contrast, the PDA/PEDOT copolymer showed only a slight decrease of 4 %, with a final capacity of 29 mAh g^{-1}. These variations, followed through half-cell charge and discharge, can be interpreted with **Figures 4.9a** and **4.9b**. Considering these results, it is likely that changing the electrode material to graphite promoted stronger intermolecular interactions and binding between PDA and the substrate, resulting in a more robust structure that prevented the faster degradation of the material. Furthermore, the higher thickness of PEDOT films might have also contributed to greater mechanical deformations. Therefore, under these conditions, the PDA/PEDOT copolymer proved to be the best cathode material.

4.2 Half-Cell Galvanostatic Charge/Discharge Cycles

In the case of galvanostatic cycling, two selected currents are alternatively applied to the electrochemical system to drive either the oxidation or the reduction of the material (**Figure 4.10a**), simultaneously allowing the removal and insertion of the sodium ions, anions and solvent within the polymer. Under an applied oxidation current, the progressive incorporation of anions (and/or expulsion of cations) is observed as PDA catechol groups are gradually converted into quinone moieties, while PEDOT increasingly carries a positive charge. This process is accompanied by a monotonic shift of potential towards more positive values (**Figure 4.10b**).

On the other hand, when reduction currents are applied, anions are expelled along with the solvent and/or sodium ions are progressively inserted into the copolymer by coordinating with the catechol groups in PDA, while the negative charges of the dopant are compensated as PEDOT shifts toward its neutral state. Conversely, this process is accompanied by a monotonic shift of potential towards more negative values.

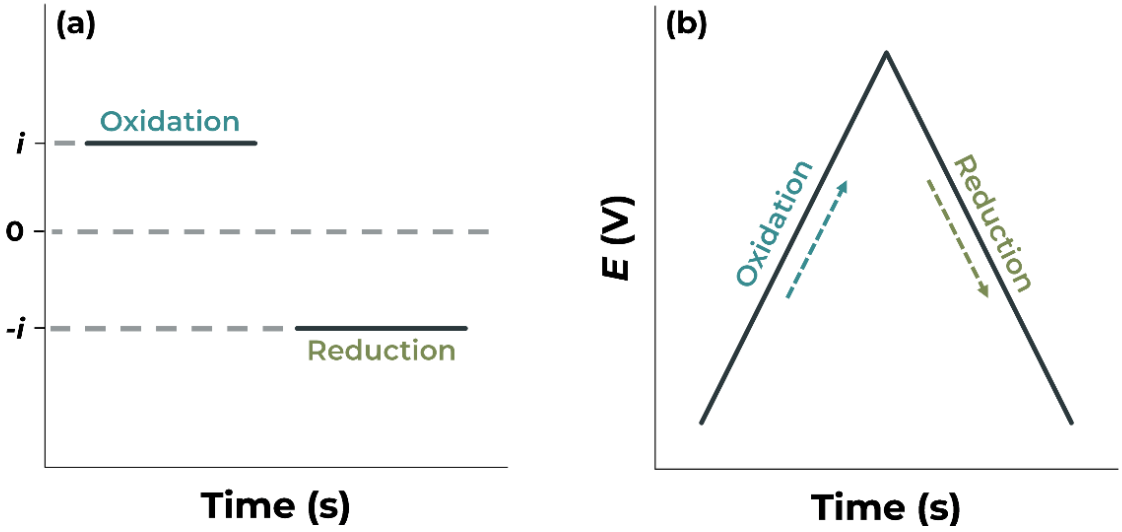

Figure 4.10 – (a) Applied current pulses during galvanostatic cycling and (b) example of the response of a galvanostatic cycle.

To properly select these currents, the film must first be characterized with cyclic voltammetry within the intended voltage window and electrolyte. From this analysis, the total charge of the material can be estimated, which then allows the selection of suitable redox currents according to the desired reaction rate (**Appendix E**). These rates are often expressed as C-rates, which describe how quickly a battery or material charges or discharges relative to its maximum capacity**.** As represented in **Equation 4.1**, a C-rate corresponds to the ratio between the applied current (I) and the total capacity of the material (Q). For instance, a 1C-rate means the material is fully charged or discharged in 1 hour. For higher C-rates (*e.g.*, 10C, 20C, 30C), it will correspond to proportionally higher currents and shorter times.[168]

$$\text{C-rate} = \frac{I\,(\text{A})}{Q(\text{Ah})} \qquad \textbf{(4.1)}$$

As in the previous potentiostatic cycling tests, the copolymer film was deposited potentiostatically over a graphite electrode in a solution with 10 mM EDOT, 20 mM DA, and 50 mM DS at 950 mV (*vs.* Ag/AgCl) for 320 s. The film was then characterized with cyclic voltammetry in 0.1 M $NaClO_4$ at 10 mV s^{-1} within the window of -600 to 700 mV (*vs.* Ag/AgCl), as previously selected for potentiostatic cycling. Based on this characterization, the appropriate current for each cycle was determined (**Appendix E**), and the copolymer film was subsequently tested at different C-rates (30C, 20C, 10C, 5C, and 2C) within the same potential window. After this, the resulting galvanostatic pulses were represented, as shown in **Figure 4.11**.

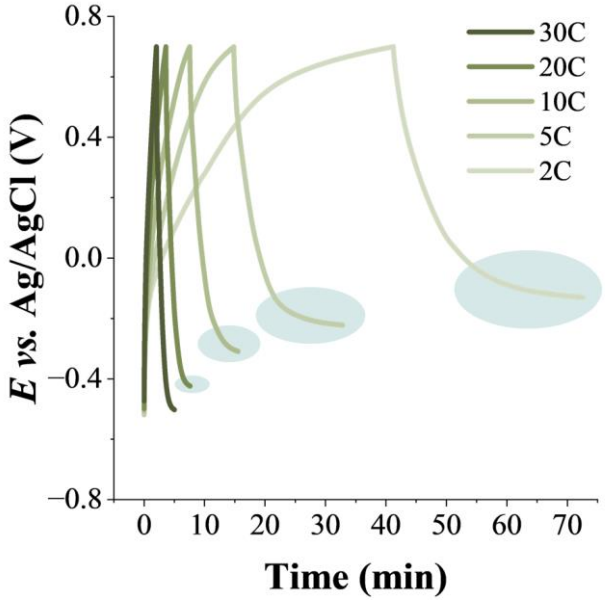

Figure 4.11 – Galvanostatic charge and discharge cycles at different C-rates (30C, 20C, 10C,5C and 2C) of the copolymer film deposited over a graphite electrode. Parasitic reaction shadowed in light blue.

As observed in **Figure 4.11**, the galvanostatic charge-discharge profiles at the lower rates do not show the expected behavior. Instead, within the potential range of -100 to -450 mV (*vs.* Ag/AgCl), the potential stabilizes, indicating that part of the applied current is being consumed by side reactions, commonly referred to as parasitic reactions. Considering the nature of graphite and its reported catalytic activity toward the oxygen reduction reaction (ORR),[169] it is likely that, if the electrode is not fully covered by the copolymer film, the exposed graphite surface contributes to the reduction of oxygen species in solution. This reasoning is supported by previous parallel studies on the activity of the copolymer toward the ORR (**Appendix F**). In these studies, the PDA/PEDOT copolymer film was deposited on a GC electrode under the same conditions described above and characterized in the presence and absence of oxygen. The results showed that the copolymer film had little to no catalytic activity for this reaction. Besides this parallel reaction, in **Figure 4.11** it is also observed that charge consumption increases with higher C-rates. This may be related to an increased capacity of the electrode to accommodate doping ions or, eventually, the occurrence of an undesirable side reaction.

Therefore, given the inadequate conditions to properly evaluate the copolymer material as a cathode material, no further analysis or conclusions were drawn from the galvanostatic pulses in **Figure 4.11**. However, considering the relevance of this technique for assessing the performance of the material as a cathode, it becomes pertinent to test the copolymer on a different substrate under optimized cycling conditions.

Despite the difficulties presented with half-cell galvanostatic charge/discharge tests, the first trial of potentiostatic cycles demonstrated the improved stability that the copolymer can provide when deposited on graphite. Future improvements in the copolymer properties, as well as the immobilization of other sodium-withdrawing species in the material, could further enhance their specific capacity. Even so, the copolymer delivered higher energies with less polymer mass when compared to PEDOT, which is very favorable for the development of lightweight batteries.

Chapter 5
Final Conclusions

“Logic will take you from A to B. Imagination will take you everywhere.”

Albert Einstein

5. Final Conclusions

Through this work, the design of a novel PDA/PEDOT copolymer, to be employed as a cathode material for sodium-ion batteries, proved to outperform the properties of its pristine polymers under the same synthesis conditions. The extensive physicochemical characterization supported the successful combination of these materials, with the electroactivity of the film showing the typical pseudocapacity of PEDOT and the redox conversion of quinone/catechol moieties of PDA. When tested as a cathode, it demonstrated greater stability and higher specific capacities than PEDOT, revealing its strong potential as a platform for next-generation hybrid organic cathode materials.

The potentiodynamic and potentiostatic electrosynthesis of the PDA/PEDOT copolymer, followed by their optimization, were first studied in Chapter 3. At this stage, high pseudocapacity and quinone/catechol redox activity were considered fundamental for optimal cathode materials. Initially, potentiodynamic electrosynthesis was performed from -800 to 900 mV (*vs.* Ag/AgCl) over 10 cycles at 50 mV s^{-1} in 10 mM EDOT, 20 mM DA, and 50 mM DS. Since the film deposition was not significant, the study was extended to 50 cycles and monitored with EQCM, concluding this method was inefficient and leading to the study of potentiostatic deposition of the films. From the previous potentiodynamic studies, it was possible to select an ideal potential range to deposit PDA/PEDOT films potentiostatically. Thus, the films were synthesized in 10 mM EDOT, 20 mM DA, and 50 mM DS, applying different potentials (-800 to 950 mV *vs.* Ag/AgCl) for 320 s. The subsequent electrochemical characterization showed that the deposition of the copolymer films was successful, presenting the expected hybrid properties of both materials.

The optimization of potentiostatic synthesis parameters, such as potential, DA monomer concentration, and electrolyte, allowed drawing several conclusions regarding the electrochemical properties of the copolymers. With increasing potential, both pseudocapacity and quinone/catechol redox activity improved, indicating progressively more oligomeric species were generated and deposited, leading to thicker copolymers. In contrast, at higher DA concentrations, a lower pseudocapacity and similar quinone/catechol conversion were observed, possibly due to the insulating growth medium imposed by DA. Regarding the electrolyte, lower DS concentration or the use of SDS or PSS decreased both responses, likely related to their more hydrophobic nature compared to DS. After optimization, the best conditions under the tested parameters were 20 mM DA, 10 mM EDOT, and 50 mM DS at a constant potential of 950 mV (*vs.* Ag/AgCl) for 320 s. Under these parameters, pristine PDA could not be deposited, while PEDOT pure films showed a comparable pseudocapacity to the PDA/PEDOT copolymer. However, EQCM studies revealed very different deposition kinetics, where PEDOT polymer reached about twice the mass of the copolymer by the end of synthesis. This finding clearly indicated the deposition of novel material and the first evidence of a distinct polymerization mechanism, likely related to a limiting step in the formation of DA-EDOT oligomeric species.

Obtaining a new material with the hybrid electroactivity of PDA and PEDOT led to the study of its physicochemical properties. To compare the copolymer synthesis against PEDOT, time deposition studies were performed using cyclic voltammetry, EQCM, and AFM. With increasing time, progressively thicker copolymer and PEDOT films were observed. Indeed, as recorded in EQCM assays, PEDOT films were always thicker than copolymer ones under the same synthesis conditions, as indicated by EQCM, and corroborated by AFM. Even so, the electroactivity of the copolymers showed an increasing pseudocapacity – always comparable to PEDOT – and the quinone/catechol redox signature. Complementary AFM analysis suggested the copolymer film evolves from a uniform, compact morphology with lower PEDOT composition at shorter times to a rougher, less uniform, and more porous coating with increasing PEDOT and PDA content at longer synthesis times.

Further characterization of two selected copolymer films, one thinner (160 s, 19 nm) and another thicker (320 s, 64 nm), was performed with FTIR, Raman, WCA, *in-situ* UV-vis and ellipsometry to gain more insights on their structural groups, wettability and dielectric properties. Spectroscopic FTIR and Raman analysis revealed a slight change in composition during film deposition, while ellipsometry confirmed the differences in compactness and aromaticity of the copolymer thinner and thicker films, which agree with the initial electrochemical and AFM time deposition studies. Additionally, the electrochemical synthesis and characterization of the films were accompanied by *in-situ* UV-vis. The spectrum of the copolymer during deposition, compared with pristine PDA and PEDOT, showed shifts in peaks and reflectance, supporting the formation of DA-EDOT oligomeric species. The spectral changes during the redox of the copolymer confirmed its behavior as a conducting polymer, where changes in the oxidized state indicated a different polymer structure compared to pristine PEDOT. Despite these interesting findings, further studies are needed to clarify the copolymer composition, adhesion, and conducting properties, as well as its polymerization and film deposition mechanisms, which could be explored using techniques such as XPS and *in-situ* spectroscopic ellipsometry.

After synthesizing and characterizing the material, it was tested as a cathode in Chapter 4. Initially, potentiostatic cycling was performed using thin PDA/PEDOT and pristine PEDOT films deposited on gold to analyze mass variation with EQCM. These results showed that thin copolymers on gold had a significantly higher specific capacity (29 mAh g^{-1} compared to 13 mAh g^{-1} for PEDOT) but experienced a faster capacity loss during cycling. For a cost-effective and sustainable approach for future applications, thicker polymeric films were deposited in graphite. In this case, the copolymer films showed initial capacities of 33 mAh g^{-1}, comparable to PEDOT (30 mAh g^{-1}). However, the copolymer presented greater stability, with a capacity retention of 96 %, while PEDOT suffered much lower retention of 66 %. Therefore, under these conditions, the PDA/PEDOT copolymer proved to be the best cathode material, holding a strong potential for further surface modification to improve the specific capacity of the film. To study polymer degradation, *in-situ* AFM could be used to monitor the expansion and contraction of the films, which is a crucial aspect on developing flexible cathode materials.

As for the galvanostatic cycles, parasitic reactions at the electrode did not allow a profound study of the material. Previous assays on the ORR of the copolymer film on GC electrodes showed that this material has little catalytic effect for this reaction, suggesting that the ORR is being promoted by the graphite substrate. In the future, it will be relevant to test other materials or a stand-alone polymer. Once experimental parameters are optimized, studies on battery cycling and capacity retention after variation of C-rates should be considered to deeply understand the behavior of the copolymer as a cathode material.

To conclude, during this work it was possible to successfully synthesize hybrid DA and EDOT copolymer material. Compared to few other reported functional materials, based on the combination of PDA and PEDOT using multi-steps procedures, the synthesis methodology proposed in this work presents a more practical approach. The results presented here provided insights into the hybrid nature of the copolymer, later proving to enhance the stability during ion intake during potentiostatic half-cycling as cathode material. As with many materials, the possibilities of synthesis, optimization, further physicochemical studies, and battery cycling are vast. Therefore, this unique family of hybrid materials is envisaged to be explored in the future to gain more insights into their properties and their chemical modification with other sodium-withdrawing compounds to further improve their specific capacities.

Chapter 6
Bibliography

6. Bibliography

(1) Armand, M.; Tarascon, J.-M. Building Better Batteries. *Nature* **2008**, *451* (7179), 652–657. https://doi.org/10.1038/451652a.

(2) Xiao, J.; Li, X.; Tang, K.; Wang, D.; Long, M.; Gao, H.; Chen, W.; Liu, C.; Liu, H.; Wang, G. Recent Progress of Emerging Cathode Materials for Sodium Ion Batteries. *Mater. Chem. Front.* **2021**, *5* (10), 3735–3764. https://doi.org/10.1039/D1QM00179E.

(3) Goodenough, J. B.; Kim, Y. Challenges for Rechargeable Li Batteries. *Chem. Mater.* **2010**, *22* (3), 587–603. https://doi.org/10.1021/cm901452z.

(4) Goodenough, J. B.; Park, K.-S. The Li-Ion Rechargeable Battery: A Perspective. *J. Am. Chem. Soc.* **2013**, *135* (4), 1167–1176. https://doi.org/10.1021/ja3091438.

(5) Deshmukh, M. K. G.; Sameeroddin, M.; Abdul, D.; Abdul Sattar, M. Renewable Energy in the 21st Century: A Review. *Mater. Today Proc.* **2023**, *80*, 1756–1759. https://doi.org/10.1016/j.matpr.2021.05.501.

(6) *Energy statistics - an overview*; Eurostat, 2025 https://ec.europa.eu/eurostat/statistics-explained/index.php?title=Energy_statistics_-_an_overview (accessed September 17, 2025).

(7) Gupta, P.; Pushpakanth, S.; Haider, M. A.; Basu, S. Understanding the Design of Cathode Materials for Na-Ion Batteries. *ACS Omega* **2022**, *7* (7), 5605–5614. https://doi.org/10.1021/acsomega.1c05794.

(8) Dunn, B.; Kamath, H.; Tarascon, J.-M. Electrical Energy Storage for the Grid: A Battery of Choices. *Science* **2011**, *334* (6058), 928–935. https://doi.org/10.1126/science.1212741.

(9) Tarascon, J.-M. Na-Ion versus Li-Ion Batteries: Complementarity Rather than Competitiveness. *Joule* **2020**, *4* (8), 1616–1620. https://doi.org/10.1016/j.joule.2020.06.003.

(10) Whittingham, M. S. Lithium Batteries and Cathode Materials. *Chem. Rev.* **2004**, *104* (10), 4271–4302. https://doi.org/10.1021/cr020731c.

(11) Kim, S.-W.; Seo, D.-H.; Ma, X.; Ceder, G.; Kang, K. Electrode Materials for Rechargeable Sodium-Ion Batteries: Potential Alternatives to Current Lithium-Ion Batteries. *Adv. Energy Mater.* **2012**, *2* (7), 710–721. https://doi.org/10.1002/aenm.201200026.

(12) Yoshino, A. The Birth of the Lithium-Ion Battery. *Angew. Chem. Int. Ed.* **2012**, *51* (24), 5798–5800. https://doi.org/10.1002/anie.201105006.

(13) He, M.; Liu, S.; Wu, J.; Zhu, J. Review of Cathode Materials for Sodium-Ion Batteries. *Prog. Solid State Chem.* **2024**, *74*, 100452. https://doi.org/10.1016/j.progsolidstchem.2024.100452.

(14) Tarascon, J.-M.; Armand, M. Issues and Challenges Facing Rechargeable Lithium Batteries. *Nature* **2001**, *414* (6861), 359–367. https://doi.org/10.1038/35104644.

(15) Nayak, P. K.; Yang, L.; Brehm, W.; Adelhelm, P. From Lithium-Ion to Sodium-Ion Batteries: Advantages, Challenges, and Surprises. *Angew. Chem. Int. Ed.* **2018**, *57* (1), 102–120. https://doi.org/10.1002/anie.201703772.

(16) Harper, G.; Sommerville, R.; Kendrick, E.; Driscoll, L.; Slater, P.; Stolkin, R.; Walton, A.; Christensen, P.; Heidrich, O.; Lambert, S.; Abbott, A.; Ryder, K.; Gaines, L.; Anderson, P. Recycling Lithium-Ion Batteries from Electric Vehicles. *Nature* **2019**, *575* (7781), 75–86. https://doi.org/10.1038/s41586-019-1682-5.

(17) Sayahpour, B.; Hirsh, H.; Parab, S.; Nguyen, L. H. B.; Zhang, M.; Meng, Y. S. Perspective: Design of Cathode Materials for Sustainable Sodium-Ion Batteries. *MRS Energy Sustain.* **2022**, *9* (2), 183–197. https://doi.org/10.1557/s43581-022-00029-9.

(18) Hwang, J.-Y.; Myung, S.-T.; Sun, Y.-K. Sodium-Ion Batteries: Present and Future. *Chem. Soc. Rev.* **2017**, *46* (12), 3529–3614. https://doi.org/10.1039/C6CS00776G.

(19) Nguyen, T. P.; Kim, I. T. Recent Advances in Sodium-Ion Batteries: Cathode Materials. *Materials* **2023**, *16* (21), 6869. https://doi.org/10.3390/ma16216869.

(20) Sommerville, R.; Shaw-Stewart, J.; Goodship, V.; Rowson, N.; Kendrick, E. A Review of Physical Processes Used in the Safe Recycling of Lithium Ion Batteries. *Sustain. Mater. Technol.* **2020**, *25*, e00197. https://doi.org/10.1016/j.susmat.2020.e00197.

(21) Walter, M.; Kovalenko, M. V.; Kravchyk, K. V. Challenges and Benefits of Post-Lithium-Ion Batteries. *New J. Chem.* **2020**, *44* (5), 1677–1683. https://doi.org/10.1039/C9NJ05682C.

(22) Dai, Z.; Mani, U.; Tan, H. T.; Yan, Q. Advanced Cathode Materials for Sodium-Ion Batteries: What Determines Our Choices? *Small Methods* **2017**, *1* (5), 1700098. https://doi.org/10.1002/smtd.201700098.

(23) Usiskin, R.; Lu, Y.; Popovic, J.; Law, M.; Balaya, P.; Hu, Y.-S.; Maier, J. Fundamentals, Status and Promise of Sodium-Based Batteries. *Nat. Rev. Mater.* **2021**, *6* (11), 1020–1035. https://doi.org/10.1038/s41578-021-00324-w.

(24) Xu, S.; Dong, H.; Yang, D.; Wu, C.; Yao, Y.; Rui, X.; Chou, S.; Yu, Y. Promising Cathode Materials for Sodium-Ion Batteries from Lab to Application. *ACS Cent. Sci.* **2023**, *9* (11), 2012–2035. https://doi.org/10.1021/acscentsci.3c01022.

(25) Mauger, A.; Julien, C. M. State-of-the-Art Electrode Materials for Sodium-Ion Batteries. *Materials* **2020**, *13* (16), 3453. https://doi.org/10.3390/ma13163453.

(26) Yu, T.; Li, G.; Duan, Y.; Wu, Y.; Zhang, T.; Zhao, X.; Luo, M.; Liu, Y. The Research and Industrialization Progress and Prospects of Sodium Ion Battery. *J. Alloys Compd.* **2023**, *958*, 170486. https://doi.org/10.1016/j.jallcom.2023.170486.

(27) More, V. S.; Yadav, M. D. Progress and Prospects in Cathode Materials for Sodium-Ion Batteries: Synthesis, Characterization, and Engineering Aspects. *Energy Fuels* **2024**, *38* (21), 20285–20313. https://doi.org/10.1021/acs.energyfuels.4c03980.

(28) Ramesh, A.; Tripathi, A.; Balaya, P. A Mini Review on Cathode Materials for Sodium-Ion Batteries. *Int. J. Appl. Ceram. Technol.* **2022**, *19* (2), 913–923. https://doi.org/10.1111/ijac.13920.

(29) Rajagopalan, R.; Tang, Y.; Jia, C.; Ji, X.; Wang, H. Understanding the Sodium Storage Mechanisms of Organic Electrodes in Sodium Ion Batteries: Issues and Solutions. *Energy Environ. Sci.* **2020**, *13* (6), 1568–1592. https://doi.org/10.1039/C9EE03637G.

(30) Zhang, H.; Gao, Y.; Liu, X.-H.; Yang, Z.; He, X.-X.; Li, L.; Qiao, Y.; Chen, W.-H.; Zeng, R.-H.; Wang, Y.; Chou, S.-L. Organic Cathode Materials for Sodium-Ion Batteries: From Fundamental Research to Potential Commercial Application. *Adv. Funct. Mater.* **2022**, *32* (4), 2107718. https://doi.org/10.1002/adfm.202107718.

(31) Yin, X.; Sarkar, S.; Shi, S.; Huang, Q.-A.; Zhao, H.; Yan, L.; Zhao, Y.; Zhang, J. Recent Progress in Advanced Organic Electrode Materials for Sodium-Ion Batteries: Synthesis, Mechanisms, Challenges and Perspectives. *Adv. Funct. Mater.* **2020**, *30* (11), 1908445. https://doi.org/10.1002/adfm.201908445.

(32) Lu, Y.; Zhang, Q.; Li, L.; Niu, Z.; Chen, J. Design Strategies toward Enhancing the Performance of Organic Electrode Materials in Metal-Ion Batteries. *Chem* **2018**, *4* (12), 2786–2813. https://doi.org/10.1016/j.chempr.2018.09.005.

(33) Häupler, B.; Wild, A.; Schubert, U. S. Carbonyls: Powerful Organic Materials for Secondary Batteries. *Adv. Energy Mater.* **2015**, *5* (11), 1402034. https://doi.org/10.1002/aenm.201402034.

(34) Asare, H.; Blodgett, W.; Satapathy, S.; John, G. Charging the Future: Harnessing Nature's Designs for Bioinspired Molecular Electrodes. *Small* **2025**, *21* (28), 2312237. https://doi.org/10.1002/smll.202312237.

(35) Han, C.; Li, H.; Shi, R.; Zhang, T.; Tong, J.; Li, J.; Li, B. Organic Quinones towards Advanced Electrochemical Energy Storage: Recent Advances and Challenges. *J. Mater. Chem. A* **2019**, *7* (41), 23378–23415. https://doi.org/10.1039/C9TA05252F.

(36) Cao, R.; Qian, J.; Zhang, J.-G.; Xu, W. Organic Cathode Materials for Rechargeable Batteries. In *Rechargeable Batteries: Materials, Technologies and New Trends*; Zhang, Z., Zhang, S. S., Eds.; Springer International Publishing: Cham, 2015; pp 637–671. https://doi.org/10.1007/978-3-319-15458-9_23.

(37) An, S. Y.; Schon, T. B.; McAllister, B. T.; Seferos, D. S. Design Strategies for Organic Carbonyl Materials for Energy Storage: Small Molecules, Oligomers, Polymers and Supramolecular Structures. *EcoMat* **2020**, *2* (4), e12055. https://doi.org/10.1002/eom2.12055.

(38) Masood, M.; Hussain, S.; Sohail, M.; Rehman, A.; Uzzaman, M. A.; Alnaser, I. A.; Karim, M. R.; Wahab, Md. A. Recent Progress, Challenges, and Opportunities of Conducting Polymers for Energy Storage Applications. *ChemistrySelect* **2024**, *9* (23), e202302876. https://doi.org/10.1002/slct.202302876.

(39) Inzelt, G. Introduction. In *Conducting Polymers: A New Era in Electrochemistry*; Inzelt, G., Ed.; Springer: Berlin, Heidelberg, 2012; pp 1–6. https://doi.org/10.1007/978-3-642-27621-7_1.

(40) Scharber, M. C.; Sariciftci, N. S. Low Band Gap Conjugated Semiconducting Polymers. *Adv. Mater. Technol.* **2021**, *6* (4), 2000857. https://doi.org/10.1002/admt.202000857.

(41) Le, T.-H.; Kim, Y.; Yoon, H. Electrical and Electrochemical Properties of Conducting Polymers. *Polymers* **2017**, *9* (4), 150. https://doi.org/10.3390/polym9040150.

(42) Chandrasekhar, P. *Conducting Polymers, Fundamentals and Applications: Including Carbon Nanotubes and Graphene*; Springer International Publishing: Cham, 2018. https://doi.org/10.1007/978-3-319-69378-1.

(43) Bredas, J. L.; Street, G. B. Polarons, Bipolarons, and Solitons in Conducting Polymers. *Acc. Chem. Res.* **1985**, *18* (10), 309–315. https://doi.org/10.1021/ar00118a005.

(44) Zhang, T.; Wu, J.; Ran, F. Poly(3, 4-Ethylenedioxythiophene) as Promising Energy Storage Materials in Zinc-Ion Batteries. *Macromol. Rapid Commun.* **2024**, *45* (23), 2400476. https://doi.org/10.1002/marc.202400476.

(45) Santos, D. R.; Zeferino, J. F.; Viana, A. S.; Wijayantha, K. G. U.; Lobato, K.; Correia, J. P. Unveiling the Mass Transport Dynamics in PEDOT:PSS Films: Insights from a Probe Beam Deflection Analysis. *Electrochimica Acta* **2025**, *529*, 146343. https://doi.org/10.1016/j.electacta.2025.146343.

(46) Su, L.; Kumar, S. S.; Manthiram, A.; Reeja-Jayan, B. A Review on Application of Poly(3,4-Ethylenedioxythiophene) (PEDOT) in Rechargeable Batteries. *Org. Mater.* **2022**, *4*, 292–300. https://doi.org/10.1055/a-1990-3149.

(47) Santos, D. R.; Zeferino, J. F.; Viana, A. S.; Wijayantha, K. G. U.; Lobato, K.; Correia, J. P. Temperature-Dependent Electrosynthesis of PEDOT:PSS: Enhanced Na^+ Transfer Targeting High-Performance Na-Ion Batteries. *Electrochimica Acta* **2025**, *518*, 145760. https://doi.org/10.1016/j.electacta.2025.145760.

(48) Sun, Y.; Huang, C.; Liu, Y.; Zhao, X.; Cai, K. Poly(3,4-Ethylenedioxythiophene)-Coated Vanadium-Doped MnO2 Nanorods for High-Performance Flexible Aqueous Zinc-Ion Battery Cathode. *ACS Appl. Mater. Interfaces* **2024**, *16* (39), 52373–52382. https://doi.org/10.1021/acsami.4c10701.

(49) Rao, L.; Cho, H.; Brooks, C. J.; Sayre, J. R.; Kim, J.-H. Advancing Extreme Fast-Charging Capabilities of LiFePO4 Using Conductive Polymer Coatings and Lithium Polyacrylate Binder. *ACS Appl. Energy Mater.* **2024**, *7* (16), 7131–7139. https://doi.org/10.1021/acsaem.4c01603.

(50) Hsiao, Y.-S.; Tseng, H.-S.; Weng, L.-Y.; Liao, S.-W.; Huang, J.-H.; Pang, W. K.; Hsu, S.-C.; Weng, H. C.; Huang, Y.-C. Interfacial Nanoarchitectonics of SiO_x via CVD Carbon Coating and Vapor-Phase Polymerized PEDOT for Enhanced Lithium-Ion Battery Anode Performance. *J. Taiwan Inst. Chem. Eng.* **2025**, *173*, 106148. https://doi.org/10.1016/j.jtice.2025.106148.

(51) Liu, A.; Wang, W.; Zhang, J.; Mo, F. Conductive Polymer-Modified Sodium Ion Intercalation in Vanadium Pentoxide for High Performance Zinc-Based Batteries. *J. Electroanal. Chem.* **2024**, *970*, 118558. https://doi.org/10.1016/j.jelechem.2024.118558.

(52) Pei, X.; Chen, Y.; Han, Y.; Zhang, D.; Ha, Y.; Li, Z.; Wang, Y. *In-Situ* Cladding PEDOT:PSS on V-Doped NCA Cathodes for Optimized Interface and High Electrochemical Performance of Li-Ion Battery. *Electrochimica Acta* **2024**, *504*, 144882. https://doi.org/10.1016/j.electacta.2024.144882.

(53) Chen, X.-C.; Ma, X.-H.; Guo, M.-K.; Lu, J. Synergistic Enhancement of Aqueous Zinc-Ion Battery Performance via Intercalated and *in-Situ* Polymerization of Poly(3,4-Ethylenedioxythiophene). *J. Alloys Compd.* **2025**, *1026*, 180532. https://doi.org/10.1016/j.jallcom.2025.180532.

(54) Wu, Y.; Zong, Q.; Zhuang, Y.; Wang, Q.; Liu, C.; Zhang, Q.; Tao, D.; Zhang, J.; Wang, J.; Cao, G. Poly(3,4-Ethylenedioxythiophene) Encapsulation/Intercalation Boosting Stability and Zinc Ion Storage Properties of Vanadyl Phosphates. *Chem. Eng. J.* **2024**, *491*, 152064. https://doi.org/10.1016/j.cej.2024.152064.

(55) Hidalgo, M. Á.; Lavela, P.; Tirado, J. L.; Aranda, M. Modification of Layered Cathodes of Sodium-Ion Batteries with Conducting Polymers. *Batteries* **2024**, *10* (3), 93. https://doi.org/10.3390/batteries10030093.

(56) Sterby, M.; Emanuelsson, R.; Huang, X.; Gogoll, A.; Strømme, M.; Sjödin, M. Characterization of PEDOT-Quinone Conducting Redox Polymers for Water Based Secondary Batteries. *Electrochimica Acta* **2017**, *235*, 356–364. https://doi.org/10.1016/j.electacta.2017.03.068.

(57) Ajjan, F. N.; Khan, Z.; Riera-Galindo, S.; Lienemann, S.; Vagin, M.; Petsagkourakis, I.; Gabrielsson, R.; Braun, S.; Fahlman, M.; Inganäs, O.; Berggren, M.; Crispin, X. Doped Conjugated Polymer Enclosing a Redox Polymer: Wiring Polyquinones with Poly(3,4-Ethylenedioxythiophene). *Adv. Energy Sustain. Res.* **2020**, *1* (2), 2000027. https://doi.org/10.1002/aesr.202000027.

(58) Oka, K.; Strietzel, C.; Emanuelsson, R.; Nishide, H.; Oyaizu, K.; Strømme, M.; Sjödin, M. Characterization of PEDOT-Quinone Conducting Redox Polymers in Water-in-Salt Electrolytes for Safe and High-Energy Li-Ion Batteries. *Electrochem. Commun.* **2019**, *105*, 106489. https://doi.org/10.1016/j.elecom.2019.106489.

(59) Emanuelsson, R.; Sterby, M.; Strømme, M.; Sjödin, M. An All-Organic Proton Battery. *J. Am. Chem. Soc.* **2017**, *139* (13), 4828–4834. https://doi.org/10.1021/jacs.7b00159.

(60) Wang, H.; Emanuelsson, R.; Liu, H.; Edström, K.; Mamedov, F.; Strømme, M.; Sjödin, M. Redox-State-Dependent Interplay between Pendant Group and Conducting Polymer Backbone in Quinone-Based Conducting Redox Polymers for Lithium Ion Batteries. *ACS Appl. Energy Mater.* **2019**, *2* (10), 7162–7170. https://doi.org/10.1021/acsaem.9b01130.

(61) Zhu, M.; Zhao, L.; Ran, Q.; Zhang, Y.; Peng, R.; Lu, G.; Jia, X.; Chao, D.; Wang, C. Bioinspired Catechol-Grafting PEDOT Cathode for an All-Polymer Aqueous Proton Battery with High Voltage and Outstanding Rate Capacity. *Adv. Sci.* **2022**, *9* (4), 2103896. https://doi.org/10.1002/advs.202103896.

(62) Oka, K.; Löfgren, R.; Emanuelsson, R.; Nishide, H.; Oyaizu, K.; Strømme, M.; Sjödin, M. Conducting Redox Polymer as Organic Anode Material for Polymer-Manganese Secondary Batteries. *ChemElectroChem* **2020**, *7* (15), 3336–3340. https://doi.org/10.1002/celc.202000711.

(63) Wang, H.; Emanuelsson, R.; Liu, H.; Mamedov, F.; Strømme, M.; Sjödin, M. A Conducting Additive-Free High Potential Quinone-Based Conducting Redox Polymer as Lithium Ion Battery Cathode. *Electrochimica Acta* **2021**, *391*, 138901. https://doi.org/10.1016/j.electacta.2021.138901.

(64) Strietzel, C.; Sterby, M.; Huang, H.; Strømme, M.; Emanuelsson, R.; Sjödin, M. An Aqueous Conducting Redox-Polymer-Based Proton Battery That Can Withstand Rapid Constant-Voltage Charging and Sub-Zero Temperatures. *Angew. Chem. Int. Ed.* **2020**, *59* (24), 9631–9638. https://doi.org/10.1002/anie.202001191.

(65) Åkerlund, L.; Emanuelsson, R.; Hernández, G.; Strømme, M.; Sjödin, M. A Crosslinked Conducting Polymer with Well-Defined Proton Trap Function for Reversible Proton Cycling in Aprotic Environments. *J. Mater. Chem. A* **2020**, *8* (24), 12114–12123. https://doi.org/10.1039/D0TA03343J.

(66) Wang, H.; Emanuelsson, R.; Karlsson, C.; Jannasch, P.; Strømme, M.; Sjödin, M. Rocking-Chair Proton Batteries with Conducting Redox Polymer Active Materials and Protic Ionic Liquid Electrolytes. *ACS Appl. Mater. Interfaces* **2021**, *13* (16), 19099–19108. https://doi.org/10.1021/acsami.1c01353.

(67) Chhin, D.; Padilla-Sampson, L.; Malenfant, J.; Rigaut, V.; Nazemi, A.; Schougaard, S. B. Conducting Polymers Doped with Bifunctional Copolymers for Improved Organic Batteries. *ACS Appl. Energy Mater.* **2019**, *2* (11), 7781–7790. https://doi.org/10.1021/acsaem.9b01104.

(68) Lukyanov, D. A.; Vereshchagin, A. A.; Soloviova, A. V.; Grigorova, O. V.; Vlasov, P. S.; Levin, O. V. Sulfonated Polycatechol Immobilized in a Conductive Polymer for Enhanced Energy Storage. *ACS Appl. Energy Mater.* **2021**, *4* (5), 5070–5078. https://doi.org/10.1021/acsaem.1c00639.

(69) Vereshchagin, A. A.; Potapenkov, V. V.; Vlasov, P. S.; Lukyanov, D. A.; Levin, O. V. Optimization of Sulfonated Polycatechol:PEDOT Energy Storage Performance by the Morphology Control. *Nanomaterials* **2022**, *12* (11), 1917. https://doi.org/10.3390/nano12111917.

(70) Sheng, L.; Fang, D.; Wang, X.; Tang, J.; Han, Q.; Zhou, J.; Tang, W. Boosting PEDOT Energy Storage with Redox Dopant and Electrolyte Additive. *Chem. Eng. J.* **2020**, *401*, 126123. https://doi.org/10.1016/j.cej.2020.126123.

(71) Admassie, S.; Elfwing, A.; Inganäs, O. Electrochemical Synthesis and Characterization of Interpenetrating Networks of Conducting Polymers for Enhanced Charge Storage. *Adv. Mater. Interfaces* **2016**, *3* (10), 1500533. https://doi.org/10.1002/admi.201500533.

(72) Noël, V.; Randriamahazaka, H. N. Redox-Assisted Hydrogen Bonding within Interpenetrating Conducting Polymer Networks for Charge-Storage Materials. *Electrochem. Commun.* **2012**, *19*, 32–35. https://doi.org/10.1016/j.elecom.2012.03.005.

(73) Volkov, A. I.; Konev, A. S.; Alekseeva, E. V.; Levin, O. V. Direct Electrochemical Co-Polymerization of EDOT and Hydroquinone. *J. Mater. Chem. A* **2025**, *13* (24), 18503–18517. https://doi.org/10.1039/D4TA07307J.

(74) Ma, T.; Zhao, Q.; Wang, J.; Pan, Z.; Chen, J. A Sulfur Heterocyclic Quinone Cathode and a Multifunctional Binder for a High-Performance Rechargeable Lithium-Ion Battery. *Angew. Chem. Int. Ed.* **2016**, *55* (22), 6428–6432. https://doi.org/10.1002/anie.201601119.

(75) Navarro-Suárez, A. M.; Carretero-González, J.; Casado, N.; Mecerreyes, D.; Rojo, T.; Castillo-Martínez, E. Hybrid Biopolymer Electrodes for Lithium- and Sodium-Ion Batteries in Organic Electrolytes. *Sustain. Energy Fuels* **2018**, *2* (4), 836–842. https://doi.org/10.1039/C7SE00551B.

(76) Ryu, J. H.; Messersmith, P. B.; Lee, H. Polydopamine Surface Chemistry: A Decade of Discovery. *ACS Appl. Mater. Interfaces* **2018**, *10* (9), 7523–7540. https://doi.org/10.1021/acsami.7b19865.

(77) Khezraqa, H.; Safavi-Mirmahalleh, S.-A.; Roghani-Mamaqani, H.; Salami-Kalajahi, M. A Review on Polydopamine as an Efficient Material in Different Components of Rechargeable Ion Batteries. *J. Energy Storage* **2024**, *79*, 110170. https://doi.org/10.1016/j.est.2023.110170.

(78) Szewczyk, J.; Aguilar-Ferrer, D.; Coy, E. Polydopamine Films: Electrochemical Growth and Sensing Applications. *Eur. Polym. J.* **2022**, *174*, 111346. https://doi.org/10.1016/j.eurpolymj.2022.111346.

(79) Lee, H. A.; Ma, Y.; Zhou, F.; Hong, S.; Lee, H. Material-Independent Surface Chemistry beyond Polydopamine Coating. *Acc. Chem. Res.* **2019**, *52* (3), 704–713. https://doi.org/10.1021/acs.accounts.8b00583.

(80) Kund, J.; Daboss, S.; D'Alvise, T. M.; Harvey, S.; Synatschke, C. V.; Weil, T.; Kranz, C. Physicochemical and Electrochemical Characterization of Electropolymerized Polydopamine Films: Influence of the Deposition Process. *Nanomaterials* **2021**, *11* (8), 1964. https://doi.org/10.3390/nano11081964.

(81) Alfieri, M. L.; Panzella, L.; Oscurato, S. L.; Salvatore, M.; Avolio, R.; Errico, M. E.; Maddalena, P.; Napolitano, A.; D'Ischia, M. The Chemistry of Polydopamine Film Formation: The Amine-Quinone Interplay. *Biomimetics* **2018**, *3* (3), 26. https://doi.org/10.3390/biomimetics3030026.

(82) Almeida, L. C.; Correia, R. D.; Marta, A.; Squillaci, G.; Morana, A.; La Cara, F.; Correia, J. P.; Viana, A. S. Electrosynthesis of Polydopamine Films - Tailored Matrices for Laccase-Based Biosensors. *Appl. Surf. Sci.* **2019**, *480*, 979–989. https://doi.org/10.1016/j.apsusc.2019.03.015.

(83) Liebscher, J.; Mrówczyński, R.; Scheidt, H. A.; Filip, C.; Hădade, N. D.; Turcu, R.; Bende, A.; Beck, S. Structure of Polydopamine: A Never-Ending Story? *Langmuir* **2013**, *29* (33), 10539–10548. https://doi.org/10.1021/la4020288.

(84) Liebscher, J. Chemistry of Polydopamine – Scope, Variation, and Limitation. *Eur. J. Org. Chem.* **2019**, *2019* (31–32), 4976–4994. https://doi.org/10.1002/ejoc.201900445.

(85) Sun, T.; Li, Z.; Wang, H.; Bao, D.; Meng, F.; Zhang, X. A Biodegradable Polydopamine-Derived Electrode Material for High-Capacity and Long-Life Lithium-Ion and Sodium-Ion Batteries. *Angew. Chem. Int. Ed.* **2016**, *55* (36), 10662–10666. https://doi.org/10.1002/anie.201604519.

(86) Mengesha, T. H.; Jeyakumar, J.; Hendri, Y. B.; Wu, Y.-S.; Yang, C.-C.; Pham, Q.-T.; Chern, C.-S.; Brunklaus, G.; Winter, M.; Hwang, B. J. Concerted Effect of Ion- and Electron-Conductive Additives on the Electrochemical and Thermal Performances of the $LiNi_{0.8}Co_{0.1}Mn_{0.1}O_2$ Cathode Material Synthesized by a Taylor-Flow Reactor for Lithium-Ion Batteries. *ACS Appl. Mater. Interfaces* **2024**, *16* (16), 21034–21049. https://doi.org/10.1021/acsami.3c19386.

(87) Almeida, L. C.; Correia, R. D.; Palys, B.; Correia, J. P.; Viana, A. S. Comprehensive Study of the Electrochemical Growth and Physicochemical Properties of Polycatecholamines and Polycatechol. *Electrochimica Acta* **2021**, *386*, 138515. https://doi.org/10.1016/j.electacta.2021.138515.

(88) Kim, R.; Nam, Y. Polydopamine-Doped Conductive Polymer Microelectrodes for Neural Recording and Stimulation. *J. Neurosci. Methods* **2019**, *326*, 108369. https://doi.org/10.1016/j.jneumeth.2019.108369.

(89) Reddy, S.; Xiao, Q.; Liu, H.; Li, C.; Chen, S.; Wang, C.; Chiu, K.; Chen, N.; Tu, Y.; Ramakrishna, S.; He, L. Bionanotube/Poly(3,4-Ethylenedioxythiophene) Nanohybrid as an Electrode for the Neural Interface and Dopamine Sensor. *ACS Appl. Mater. Interfaces* **2019**, *11* (20), 18254–18267. https://doi.org/10.1021/acsami.9b04862.

(90) Huang, W.-C.; Hung, C.-H.; Lin, Y.-W.; Zheng, Y.-C.; Lei, W.-L.; Lu, H.-E. Electrically Copolymerized Polydopamine Melanin/Poly(3,4-Ethylenedioxythiophene) Applied for Bioactive Multimodal Neural Interfaces with Induced Pluripotent Stem Cell-Derived Neurons. *ACS Biomater. Sci. Eng.* **2022**, *8* (11), 4807–4818. https://doi.org/10.1021/acsbiomaterials.2c00822.

(91) Zeng, M.; Wang, X.; Ma, R.; Zhu, W.; Li, Y.; Chen, Z.; Zhou, J.; Li, W.; Liu, T.; He, Z.; Yan, H.; Huang, F.; Cao, Y. Dopamine Semiquinone Radical Doped PEDOT:PSS: Enhanced

Conductivity, Work Function and Performance in Organic Solar Cells. *Adv. Energy Mater.* **2020**, *10* (25), 2000743. https://doi.org/10.1002/aenm.202000743.

(92) Huang, J.; Wang, C.; Liu, Z.; Qiu, X.; Yang, J.; Chang, J. Simultaneouly Enhanced Durability and Performance by Employing Dopamine Copolymerized PEDOT with High Work Function and Water-Proofness for Inverted Perovskite Solar Cells. *J. Mater. Chem. C* **2018**, *6* (9), 2311–2318. https://doi.org/10.1039/C7TC05276F.

(93) Carter, J. L.; Kelly, C. A.; Jenkins, M. J. Enhanced Adhesion of PEDOT:PSS to Substrates Using Polydopamine as a Primer. *Polym. J.* **2024**, *56* (2), 115–120. https://doi.org/10.1038/s41428-023-00846-w.

(94) Li, X.; Zhao, X.; Liu, R.; Wang, H.; Wang, S.; Fan, B.; Hu, C.; Wang, H. Mussel-Inspired PDA@PEDOT Nanocomposite Hydrogel with Excellent Mechanical Strength, Self-Adhesive, and Self-Healing Properties for a Flexible Strain Sensor. *J. Mater. Chem. B* **2024**, *12* (12), 3092–3102. https://doi.org/10.1039/D3TB02748A.

(95) Ermis, S.; Tohtayeva, J.; Altınışık, S.; Uluçay, S.; Jockusch, S.; Kiskan, B.; Koyuncu, S.; Kaya, K. Light-Driven Sustainable Synthesis of Pedot-Coated Polydopamine: A Path Towards Next-Generation Supercapacitor Electrodes. *Social Science Research Network: Rochester*, NY March 9, 2025. https://doi.org/10.2139/ssrn.5171398.

(96) Cha, I.; Lee, E. J.; Park, H. S.; Kim, J.-H.; Kim, Y. H.; Song, C. Facile Electrochemical Synthesis of Polydopamine-Incorporated Graphene Oxide/PEDOT Hybrid Thin Films for Pseudocapacitive Behaviors. *Synth. Met.* **2014**, *195*, 162–166. https://doi.org/10.1016/j.synthmet.2014.05.019.

(97) Kim, S.; Jang, L. K.; Park, H. S.; Lee, J. Y. Electrochemical Deposition of Conductive and Adhesive Polypyrrole-Dopamine Films. *Sci. Rep.* **2016**, *6* (1), 30475. https://doi.org/10.1038/srep30475.

(98) Geng, H.; Lupton, E. J.; Ma, Y.; Sun, R.; Grigsby, C. L.; Brachi, G.; Li, X.; Zhou, K.; Stuckey, D. J.; Stevens, M. M. Hybrid Polypyrrole and Polydopamine Nanosheets for Precise Raman/Photoacoustic Imaging and Photothermal Therapy. *Adv. Healthc. Mater.* **2023**, *12* (27), 2301148. https://doi.org/10.1002/adhm.202301148.

(99) Yang, M.; Wang, Z.; Ding, T.; Tang, J.; Xie, X.; Xing, Y.; Wang, L.; Zhang, J.; Cai, K. Interfacial Engineering of Hybrid Polydopamine/Polypyrrole Nanosheets with Narrow Band Gaps for Fluorescence Sensing of MicroRNA. *ACS Appl. Mater. Interfaces* **2021**, *13* (35), 42183–42194. https://doi.org/10.1021/acsami.1c11301.

(100) Kim, S.; Jang, L. K.; Jang, M.; Lee, S.; Hardy, J. G.; Lee, J. Y. Electrically Conductive Polydopamine–Polypyrrole as High Performance Biomaterials for Cell Stimulation in Vitro and Electrical Signal Recording in Vivo. *ACS Appl. Mater. Interfaces* **2018**, *10* (39), 33032–33042. https://doi.org/10.1021/acsami.8b11546.

(101) Kim, M.; Li, S.; Kong, D. S.; Song, Y. E.; Park, S.-Y.; Kim, H.; Jae, J.; Chung, I.; Kim, J. R. Polydopamine/Polypyrrole-Modified Graphite Felt Enhances Biocompatibility for Electroactive Bacteria and Power Density of Microbial Fuel Cell. *Chemosphere* **2023**, *313*, 137388. https://doi.org/10.1016/j.chemosphere.2022.137388.

(102) Yen, T.-Y.; Liu, J.-Y.; Parayangattil Jyothibasu, J.; Yang, H.; Chan, S.-H.; Lin, H.-L.; Sun, Y.-M.; Lee, R.-H. Synergistic Combination of Polydopamine and Polypyrrole in Natural Pectin/PVA-Based Freestanding Electrodes for High-Performance Supercapacitors. *ACS Omega* **2025**, *10* (6), 6025–6037. https://doi.org/10.1021/acsomega.4c10148.

(103) Han, L.; Yan, L.; Wang, M.; Wang, K.; Fang, L.; Zhou, J.; Fang, J.; Ren, F.; Lu, X. Transparent, Adhesive, and Conductive Hydrogel for Soft Bioelectronics Based on Light-Transmitting Polydopamine-Doped Polypyrrole Nanofibrils. *Chem. Mater.* **2018**, *30* (16), 5561–5572. https://doi.org/10.1021/acs.chemmater.8b01446.

(104) Tan, J.; Zhang, Z.; He, Y.; Yue, Q.; Xie, Z.; Ji, H.; Sun, Y.; Shi, W.; Ge, D. Electrochemical Synthesis of Conductive, Superhydrophobic and Adhesive Polypyrrole-Polydopamine Nanowires. *Synth. Met.* **2017**, *234*, 86–94. https://doi.org/10.1016/j.synthmet.2017.10.012.

(105) Lee, M.; Kim, S.; Jang, M.; Park, H. S.; Lee, J. Y. One-Pot Electrochemical Fabrication of High Performance Amperometric Enzymatic Biosensors Using Polypyrrole and Polydopamine. *J. Ind. Eng. Chem.* **2021**, *97*, 316–325. https://doi.org/10.1016/j.jiec.2021.02.009.

(106) Lin, Q.; Yang, Y.; Ma, Y.; Zhang, R.; Wang, J.; Chen, X.; Shao, Z. Bandgap Engineered Polypyrrole–Polydopamine Hybrid with Intrinsic Raman and Photoacoustic Imaging Contrasts. *Nano Lett.* **2018**, *18* (12), 7485–7493. https://doi.org/10.1021/acs.nanolett.8b02901.

(107) Carneiro, D. M.; Almeida, L. C.; Santos, D. R.; Correia, J. P.; Viana, A. S. Conductive Polycatecholamine (or Polycatechol)/Polypyrrole Copolymers Enriched in Catechol Moieties for Amperometric Sensing Application. *Electrochimica Acta* **2025**, *524*, 146004. https://doi.org/10.1016/j.electacta.2025.146004.

(108) Li, F.; Yang, L.; Zhao, C.; Du, Z. Electroactive Gold Nanoparticles/Polyaniline/Polydopamine Hybrid Composite in Neutral Solution as High-Performance Sensing Platform. *Anal. Methods* **2011**, *3* (7), 1601–1606. https://doi.org/10.1039/C1AY05126A.

(109) Wang, Y.; Wu, S.; Yin, Q.; Du, K.; Yin, Q.; Jiang, B.; Mo, S. Novel Hybrid P- and n-Type Organic Thermoelectric Materials Based on Mussel-Inspired Polydopamine. *ACS Appl. Mater. Interfaces* **2021**, *13* (20), 23970–23982. https://doi.org/10.1021/acsami.1c01457.

(110) Wang, X.; Lee, P. S. A Polydopamine Coated Polyaniline Single Wall Carbon Nanotube Composite Material as a Stable Supercapacitor Cathode in an Organic Electrolyte. *J. Mater. Res.* **2015**, *30* (23), 3575–3583. https://doi.org/10.1557/jmr.2015.342.

(111) Huang, Y.; Zhang, B.; Wu, J.; Hong, R.; Xu, J. Preparation and Characterization of Graphene Oxide/Polyaniline/Polydopamine Nanocomposites towards Long-Term Anticorrosive Performance of Epoxy Coatings. *Polymers* **2022**, *14* (16), 3355. https://doi.org/10.3390/polym14163355.

(112) Elanthamilan, E.; Ganeshkumar, A.; Wang, S.-F.; Rajaram, R.; Thriambakeshwar, S.; Velusamy, M. Fabrication of Polydopamine/Polyaniline Decorated Multiwalled Carbon Nanotube Composite as Multifunctional Electrode Material for Supercapacitor Applications. *Synth. Met.* **2023**, *298*, 117423. https://doi.org/10.1016/j.synthmet.2023.117423.

(113) Massoumi, B.; Abbasian, M.; Jahanban-Esfahlan, R.; Mohammad-Rezaei, R.; Khalilzadeh, B.; Samadian, H.; Rezaei, A.; Derakhshankhah, H.; Jaymand, M. A Novel Bio-Inspired Conductive, Biocompatible, and Adhesive Terpolymer Based on Polyaniline, Polydopamine, and Polylactide as Scaffolding Biomaterial for Tissue Engineering Application. *Int. J. Biol. Macromol.* **2020**, *147*, 1174–1184. https://doi.org/10.1016/j.ijbiomac.2019.10.086.

(114) Bockris, J. O.; Reddy, A. K. N. *Modern Electrochemistry 1: Ionics*; Springer US: Boston, MA, 1998. https://doi.org/10.1007/b114546.

(115) Bard, A. J.; Faulkner, L. R. *Electrochemical Methods: Fundamentals and Applications*; Wiley: New York, Weinheim, 2001.

(116) Brett, C. M. A.; Brett, A. M. O. *Electrochemistry: Principles, Methods, and Applications*; Oxford University Press: Oxford, 2005.

(117) Elgrishi, N.; Rountree, K. J.; McCarthy, B. D.; Rountree, E. S.; Eisenhart, T. T.; Dempsey, J. L. A Practical Beginner's Guide to Cyclic Voltammetry. *J. Chem. Educ.* **2018**, *95* (2), 197–206. https://doi.org/10.1021/acs.jchemed.7b00361.

(118) Pletcher, D.; Greff, R.; Peat, R.; Peter, L. M.; Robinson, J. 6 - Potential Sweep Techniques and Cyclic Voltammetry. In *Instrumental Methods in Electrochemistry*; Pletcher, D., Greff, R., Peat, R., Peter, L. M., Robinson, J., Eds.; Woodhead Publishing: Cambridge, 2010; pp 178–228. https://doi.org/10.1533/9781782420545.178.

(119) Bockris, J. O., Reddy, A. K. N. Chapter 8, Transients. In *Modern Electrochemistry 2A: Fundamentals of Electrodics*; Bockris, J. O., Reddy, A. K. N., Gamboa-Aldeco, M., Eds.; Springer US: Boston, MA, 2000; pp 1401–1454. https://doi.org/10.1007/0-306-47605-3_3.
(120) Pletcher, D.; Greff, R.; Peat, R.; Peter, L. M.; Robinson, J. 2 - Steady State and Potential Step Techniques. In *Instrumental Methods in Electrochemistry*; Pletcher, D., Greff, R., Peat, R., Peter, L. M., Robinson, J., Eds.; Woodhead Publishing: Cambridge, 2010; pp 42–75. https://doi.org/10.1533/9781782420545.42.
(121) Calvo, E. J.; Etchenique, R. A. Chapter 12 - Kinetic Applications of the Electrochemical Quartz Crystal Microbalance (EQCM). In *Comprehensive Chemical Kinetics*; Compton, R. G., Hancock, G., Eds.; Applications of Kinetic Modelling; Elsevier: Amsterdam, 1999; Vol. 37, pp 461–487. https://doi.org/10.1016/S0069-8040(99)80017-X.
(122) Deakin, M. R.; Buttry, D. A. Electrochemical Applications of the Quartz Crystal Microbalance. *Anal. Chem.* **1989**, *61* (20), 1147A-1154A. https://doi.org/10.1021/ac00195a001.
(123) Bruckenstein, S.; Hillman, A. R. Electrochemical Quartz Crystal Microbalance Studies of Electroactive Surface Films. In *The Handbook of Surface Imaging and Visualization*; Hubbard. A. T. Ed; CRC Press: Boca Raton, 1995; pp 101–112. https://doi.org/10.1201/9780367811815.
(124) Hillman, A. R. The EQCM: Electrogravimetry with a Light Touch. *J. Solid State Electrochem.* **2011**, *15* (7), 1647–1660. https://doi.org/10.1007/s10008-011-1371-2.
(125) Eaton, P.; West, P. *Atomic Force Microscopy*; Oxford University Press: Oxford, New York, 2010.
(126) Friedbacher, G.; Fuchs, H. Classification of Scanning Probe Microscopies. *Pure Appl. Chem.* **1999**, *71* (7), 1337–1357. https://doi.org/10.1351/pac199971071337.
(127) Gadegaard, N. Atomic Force Microscopy in Biology: Technology and Techniques. *Biotech. Histochem.* **2006**, *81* (2–3), 87–97. https://doi.org/10.1080/10520290600783143.
(128) Joshua, A. M.; Cheng, G.; Lau, E. V. Soft Matter Analysis via Atomic Force Microscopy (AFM): A Review. *Appl. Surf. Sci. Adv.* **2023**, *17*, 100448. https://doi.org/10.1016/j.apsadv.2023.100448.
(129) Alsteens, D.; Dupres, V.; Yunus, S.; Latgé, J.-P.; Heinisch, J. J.; Dufrêne, Y. F. High-Resolution Imaging of Chemical and Biological Sites on Living Cells Using Peak Force Tapping Atomic Force Microscopy. *Langmuir* **2012**, *28* (49), 16738–16744. https://doi.org/10.1021/la303891j.
(130) Xu, K.; Sun, W.; Shao, Y.; Wei, F.; Zhang, X.; Wang, W.; Li, P. Recent Development of PeakForce Tapping Mode Atomic Force Microscopy and Its Applications on Nanoscience. *Nanotechnol. Rev.* **2018**, *7* (6), 605–621. https://doi.org/10.1515/ntrev-2018-0086.
(131) Sedin, D. L.; Rowlen, K. L. Influence of Tip Size on AFM Roughness Measurements. *Appl. Surf. Sci.* **2001**, *182* (1), 40–48. https://doi.org/10.1016/S0169-4332(01)00432-9.
(132) Voigtländer, B. *Scanning Probe Microscopy: Atomic Force Microscopy and Scanning Tunneling Microscopy*; NanoScience and Technology; Springer: Berlin, Heidelberg, 2015. https://doi.org/10.1007/978-3-662-45240-0.
(133) Gottesfeld, S. Ellipsometry: Principles and Recent Applications in Electrochemistry. In *Electroanalytical Chemistry*; Bard, A. J.; CRC Press, 1988; pp 144–259 https://doi.org/10.1201/9781003418115.
(134) Fujiwara, H. *Spectroscopic Ellipsometry: Principles and Applications*; Wiley: Chichester, 2009. https://doi.org/10.1002/9780470060193
(135) Huhtamäki, T.; Tian, X.; Korhonen, J. T.; Ras, R. H. A. Surface-Wetting Characterization Using Contact-Angle Measurements. *Nat. Protoc.* **2018**, *13* (7), 1521–1538. https://doi.org/10.1038/s41596-018-0003-z.
(136) Peethan, A.; Aravind, M.; George, S. D. Surface Wettability and Superhydrophobicity. In *Advances in Superhydrophobic Coatings*; Saji, V. S., Ed.; Royal Society of Chemistry, 2023; pp 1–25. https://doi.org/10.1039/9781837670031-00001.

(137) Razavi, M.; Primavera, R.; Vykunta, A.; Thakor, A. S. Silicone-Based Bioscaffolds for Cellular Therapies. *Mater. Sci. Eng. C* **2021**, *119*, 111615. https://doi.org/10.1016/j.msec.2020.111615.
(138) Fomo, G.; Waryo, T.; Feleni, U.; Baker, P.; Iwuoha, E. Electrochemical Polymerization. In *Functional Polymers*; Springer, Cham, 2019; pp 105–131. https://doi.org/10.1007/978-3-319-95987-0_3.
(139) Almeida, L. C.; Correia, R. D.; Correia, J. P.; Viana, A. S. Combined Electrochemical, Ellipsometric and Microgravimetric Study of Ion Permeable Polydopamine Films. *J. Electrochem. Soc.* **2022**, *169* (4), 046503.
(140) Wang, J.; Li, B.; Li, Z.; Ren, K.; Jin, L.; Zhang, S.; Chang, H.; Sun, Y.; Ji, J. Electropolymerization of Dopamine for Surface Modification of Complex-Shaped Cardiovascular Stents. *Biomaterials* **2014**, *35* (27), 7679–7689. https://doi.org/10.1016/j.biomaterials.2014.05.047.
(141) Li, Y.; Liu, M.; Xiang, C.; Xie, Q.; Yao, S. Electrochemical Quartz Crystal Microbalance Study on Growth and Property of the Polymer Deposit at Gold Electrodes during Oxidation of Dopamine in Aqueous Solutions. *Thin Solid Films* **2006**, *497* (1), 270–278. https://doi.org/10.1016/j.tsf.2005.10.048.
(142) Melato, A. I.; Viana, A. S.; Abrantes, L. M. Different Steps in the Electrosynthesis of Poly(3,4-Ethylenedioxythiophene) on Platinum. *Electrochimica Acta* **2008**, *54* (2), 590–597. https://doi.org/10.1016/j.electacta.2008.07.030.
(143) Randriamahazaka, H.; Noël, V.; Chevrot, C. Nucleation and Growth of Poly(3,4-Ethylenedioxythiophene) in Acetonitrile on Platinum under Potentiostatic Conditions. *J. Electroanal. Chem.* **1999**, *472* (2), 103–111. https://doi.org/10.1016/S0022-0728(99)00258-2.
(144) Zhou, H.; Zhi, X. Surfactant-Assisted Potentiodynamically Polymerized PEDOT Fibers for Significantly Improved Electrochemical Capacitive Properties. *Mater. Lett.* **2018**, *221*, 309–312. https://doi.org/10.1016/j.matlet.2018.03.140.
(145) Tamburri, E.; Orlanducci, S.; Toschi, F.; Terranova, M. L.; Passeri, D. Growth Mechanisms, Morphology, and Electroactivity of PEDOT Layers Produced by Electrochemical Routes in Aqueous Medium. *Synth. Met.* **2009**, *159* (5), 406–414. https://doi.org/10.1016/j.synthmet.2008.10.014.
(146) Harris, A. R.; Molino, P. J.; Kapsa, R. M. I.; Clark, G. M.; Paolini, A. G.; Wallace, G. G. Effective Area and Charge Density of Dextran Sulphate Doped PEDOT Modified Electrodes. *Synth. Met.* **2016**, *220*, 394–401. https://doi.org/10.1016/j.synthmet.2016.07.010.
(147) Melato, A. I.; Viana, A. S.; Abrantes, L. M. Influence of the Electropolymerisation Mode on PEDOTh Films Morphology and Redox Behaviour—an AFM Investigation. *J. Solid State Electrochem.* **2010**, *14* (4), 523–530. https://doi.org/10.1007/s10008-008-0684-2.
(148) Sakunpongpitiporn, P.; Phasuksom, K.; Paradee, N.; Sirivat, A. Facile Synthesis of Highly Conductive PEDOT:PSS via Surfactant Templates. *RSC Adv.* **2019**, *9* (11), 6363–6378. https://doi.org/10.1039/C8RA08801B.
(149) *Dextran Sulfate Sodium Salt, MW ca 40,000, 100 g;* Thermo Scientific Chemicals. https://www.thermofisher.com/order/catalog/product/J63606.22 (accessed August 8, 2025).
(150) Cui, J.; Ma, C.; Li, Z.; Wu, L.; Wei, W.; Chen, M.; Peng, B.; Deng, Z. Polydopamine-Functionalized Polymer Particles as Templates for Mineralization of Hydroxyapatite: Biomimetic and in Vitro Bioactivity. *RSC Adv.* **2016**, *6* (8), 6747–6755. https://doi.org/10.1039/C5RA24821C.
(151) Famkar, E.; Pircheraghi, G.; Nazockdast, H. Effectively Exerting the Reinforcement of Polyvinyl Alcohol Nanocomposite Hydrogel via Poly(Dopamine) Functionalized Graphene Oxide. *Compos. Sci. Technol.* **2022**, *217*, 109119. https://doi.org/10.1016/j.compscitech.2021.109119.

(152) Kvarnström, C.; Neugebauer, H.; Blomquist, S.; Ahonen, H. J.; Kankare, J.; Ivaska, A. In Situ Spectroelectrochemical Characterization of Poly(3,4-Ethylenedioxythiophene). *Electrochimica Acta* **1999**, *44* (16), 2739–2750. https://doi.org/10.1016/S0013-4686(98)00405-8.

(153) Cakić, M.; Nikolić, G.; Ilić, L.; Stanković, S. Synthesis and FTIR Characterization of Some Dextran Sulphates. *Chem. Ind. Chem. Eng. Q.* **2005**, *11* (2), 74–78.

(154) Gribkova, O. L.; Iakobson, O. D.; Nekrasov, A. A.; Cabanova, V. A.; Tverskoy, V. A.; Vannikov, A. V. The Influence of Polyacid Nature on Poly(3,4-Ethylenedioxythiophene) Electrosynthesis and Its Spectroelectrochemical Properties. *J. Solid State Electrochem.* **2016**, *20* (11), 2991–3001. https://doi.org/10.1007/s10008-016-3252-1.

(155) Łapkowski, M.; Proń, A. Electrochemical Oxidation of Poly(3,4-Ethylenedioxythiophene) — "*in Situ*" Conductivity and Spectroscopic Investigations. *Synth. Met.* **2000**, *110* (1), 79–83. https://doi.org/10.1016/S0379-6779(99)00271-4.

(156) Garreau, S.; Louarn, G.; Froyer, G.; Lapkowski, M.; Chauvet, O. Spectroelectrochemical Studies of the C14-Alkyl Derivative of Poly(3,4-Ethylenedioxythiophene) (PEDT). *Electrochimica Acta* **2001**, *46* (8), 1207–1214. https://doi.org/10.1016/S0013-4686(00)00693-9.

(157) Almeida, L. C. Electrosynthesis of Biocompatible Polycatecholamine Films. Ph.D. Dissertation, Faculty of Sciences of the University of Lisbon, Lisbon, Portugal, 2024. https://repositorio.ulisboa.pt/handle/10400.5/98532 (accessed September 19, 2025).

(158) Xie, X.; Gao, N.; Zhu, L.; Hunter, M.; Chen, S.; Zang, L. PEDOT:PSS/PEDOT Film Chemiresistive Sensors for Hydrogen Peroxide Vapor Detection under Ambient Conditions. *Chemosensors* **2023**, *11* (2), 124. https://doi.org/10.3390/chemosensors11020124.

(159) Cheng, X.; Zhao, J.; Fu, Y.; Cui, C.; Zhang, X. Electrosynthesis and Characterization of a Multielectrochromic Copolymer of Tris[4-(2-Thienyl)Phenyl]Amine with 3,4-Ethylenedioxythiophene. *J. Electrochem. Soc.* **2012**, *160* (1), G6. https://doi.org/10.1149/2.040301jes.

(160) Kabanova, V.; Gribkova, O.; Nekrasov, A. Poly(3,4-Ethylenedioxythiophene) Electrosynthesis in the Presence of Mixtures of Flexible-Chain and Rigid-Chain Polyelectrolytes. *Polymers* **2021**, *13* (22), 3866. https://doi.org/10.3390/polym13223866.

(161) Zozoulenko, I.; Singh, A.; Singh, S. K.; Gueskine, V.; Crispin, X.; Berggren, M. Polarons, Bipolarons, And Absorption Spectroscopy of PEDOT. *ACS Appl. Polym. Mater.* **2019**, *1* (1), 83–94. https://doi.org/10.1021/acsapm.8b00061.

(162) Wang, F.; Han, R.; Liu, G.; Chen, H.; Ren, T.; Yang, H.; Wen, Y. Construction of Polydopamine/Silver Nanoparticles Multilayer Film for Hydrogen Peroxide Detection. *J. Electroanal. Chem.* **2013**, *706*, 102–107. https://doi.org/10.1016/j.jelechem.2013.08.008.

(163) Harman, D. G.; Gorkin, R.; Stevens, L.; Thompson, B.; Wagner, K.; Weng, B.; Chung, J. H. Y.; in het Panhuis, M.; Wallace, G. G. Poly(3,4-Ethylenedioxythiophene):Dextran Sulfate (PEDOT:DS) – A Highly Processable Conductive Organic Biopolymer. *Acta Biomater.* **2015**, *14*, 33–42. https://doi.org/10.1016/j.actbio.2014.11.049.

(164) Yamato, H.; Kai, K.; Ohwa, M.; Wernet, W.; Matsumura, M. Mechanical, Electrochemical and Optical Properties of Poly(3,4-Ethylenedioxythiophene)/Sulfated Poly(β-Hydroxyethers) Composite Films. *Electrochimica Acta* **1997**, *42* (16), 2517–2523. https://doi.org/10.1016/S0013-4686(96)00442-2.

(165) Abrantes, L. M.; Correia, J. P.; Melato, A. I. An Ellipsometric Study of Poly(3,4-Ethylenedioxythiophene) Electrosynthesis – from the Initial Stages to Thick Layers Formation. *J. Electroanal. Chem.* **2010**, *646* (1), 75–84. https://doi.org/10.1016/j.jelechem.2010.02.025.

(166) Abrantes, L. M.; Correia, J. P.; Jin, G. The Heterogeneous Growth of P(3MeTh)—an Ellipsometric Study. *Electrochimica Acta* **2001**, *46* (26), 3993–3999. https://doi.org/10.1016/S0013-4686(01)00706-X.

(167) Attia, P. M.; Das, S.; Harris, S. J.; Bazant, M. Z.; Chueh, W. C. Electrochemical Kinetics of SEI Growth on Carbon Black: Part I. Experiments. *J. Electrochem. Soc.* **2019**, *166* (4), E97. https://doi.org/10.1149/2.0231904jes.

(168) Yang, X.; Rogach, A. L. Electrochemical Techniques in Battery Research: A Tutorial for Nonelectrochemists. *Adv. Energy Mater.* **2019**, *9* (25), 1900747. https://doi.org/10.1002/aenm.201900747.

(169) Soliman, A. B.; Abdel-Samad, H. S.; Abdel Rehim, S. S.; Hassan, H. H. Surface Functionality and Electrochemical Investigations of a Graphitic Electrode as a Candidate for Alkaline Energy Conversion and Storage Devices. *Sci. Rep.* **2016**, *6* (1), 22056. https://doi.org/10.1038/srep22056.

Appendix

Appendix

Appendix A – Summary of Hybrid Carbonyl and PEDOT Materials

Table A1 – Synthesis method, specific capacities, and cycling conditions of reported hybrid carbonyl/PEDOT materials.

Material	Synthesis Method	Theoretical Capacity, Experimental Capacity	Number of cycles, Speed and retention	Electrolyte	References
PEDOT-Quinone Conducting Redox Polymer	Potentiodynamic Growth	163 mAh g^{-1}, -	50, 30C, 63 %	~15 M LiTFSI in water/DMC (1:1 mass ratio)	56,58
PTC-PEDOT Conducting Redox Polymer	Potentiodynamic Growth	225 mAh g^{-1}, 62.0 mAh g^{-1}	1000, 20 A g^{-1}, 80 %	0.5 M H_2SO_4 aqueous solution	61
PEDOT Doped with a poly(4-vinylcatechol-r-styrenesulfonic acid (PEDOT:P(4VC-36))	Potentiodynamic growth	95 mAh g^{-1}, 52 mAh g^{-1}	200, 10 mV s^{-1} (CV), 80 %	0.2 M H_2SO_4 aqueous solution	67
PEDOT doped with sulfonated polycatechol (PEDOT:SPVQ)	Potentiodynamic growth	330 mAh g^{-1}, 95 mAh g^{-1}	1000, 20 mV s^{-1} (CV), 57 %	0.1 M $HClO_4$ aqueous solution	68, 69
PEDOT-BQ Conducting Redox Polymer	Potentiodynamic growth	160 mAh g^{-1}, 90 mAh g^{-1}	125, 600 mA g^{-1}, 44%	Equimolar 2-fluoropyridinium triflate-2-fluoropyridine electrolyte slurry	59
$Q(CF_3)_2$-PEDOT	Potentiodynamic growth	-, ~40 mAh g^{-1}	200, 50 mV s^{-1} (CV), , 67%	0.2 M $LiPF_6$ in propylene carbonate	60
PEDOT/PDAAQ Composite Polymer	Two-step Galvanostatic Growth	-	-	-	72
PDAAQ/PEDOT Composite Polymer	Two-step Galvanostatic growth	-, 106 mAh g^{-1}	2000, 2 A g^{-1}, 91 %	0.1 M $HClO_4$, aqueous solution	71
pEP(NQ)E Conducting Redox Polymer	Potentiostatic Growth	76 mAh g^{-1}, ~ 76 mAh g^{-1}	> 50, 1C, 99 %	1 M $MnSO_4$ + 0.05 M H_2SO_4 aqueous solution	62
PEDOT/PHQ Copolymer	Potentiostatic Growth	-, ~112 mAh g^{-1}	200, 0.2 mA cm^{-2}, 65 %	0.1 M $HClO_4$ aqueous solution	73
AQS Doped PEDOT	Potentiostatic growth	-, 0.27 mA h cm^{-1}	10000, 20 mA h cm^{-1}, 82 %	1 M H_2SO_4 aqueous solution	70

p(Qz-EPE)	Post-deposition polymerization	68 mA h / g^{-1}, 60 mA h / g^{-1}	500, 1.5C, 74%	1 M $LiPF_6$ in EC/DEC (1:1 v/v)	63
pEP(NQ)E	Post-deposition polymerization	75 mAh g^{-1}, 68 mAh g^{-1}	100, 3C, ~ 100%	0.5 M H_2SO_4 aqueous solution	64
p(EPE-trap-EPE)	Post-deposition polymerization	84 mAh g^{-1}, 81 mAh g^{-1}	200, 2C, 98 %	1 M $LiPF_6$ in EC/DEC	65
poly(QzH_2-EPE)	Post-deposition polymerization	68 mAh g^{-1}, 58 mAh g^{-1}	500, 4.5 C, 75 %	Protic ionic liquid: 1-methyl-1,2,4-triazole trifluoromethanesulfonimide (MeTriHTFSI)	66
PACA–PEDOT nanocomposite	Two-step chemical oxidative polymerization	-, 198 mAh g^{-1}	5000, 32 A g^{-1}, 60 %	0.1 M $HClO_4$, aqueous solution	57
DTT with PEDOT Binder	Slurry casting method	285 mAh g^{-1}, 220 mAh g^{-1}	200, 1C, 93 %	2 M LiTFSI in 1,3-dioxolane (DOL)/dimethoxyethane (DME) with 1 wt% $LiNO_3$ additive	74
Lignin/PEDOT C65 composite	Chemical oxidative polymerization	-, 159 mAh g^{-1}	25, C/20, ~ 46 %	1 M $NaPF_6$ EC/DMC	75

Table A2 – Synthesis method, monomer concentration, and substrate and medium used during synthesis of reported PDA/PEDOT hybrid materials.

Application	**Synthesis**	**EDOT/DA Concentration**	**Substrate**	**Dispersed Medium**	**Reference**
Detection and Modulation of Neural Networks	Potentiostatic Growth	20 mM EDOT; 2 mg mL^{-1} DA·HCl	Gold Microelectrode	Aqueous Sodium Phosphate Buffer (SPB) (10 mM; pH = 6)	88
Neural electrode for brain-machine interfaces	Potentiodynamic Growth	0.01 M EDOT; 0.01M DA·HCl	ITO-glass	Aqueous solution (pH=6)	90
Multifunctional neural electrode with DA detection	Two-step chemical oxidative polymerization	0.02 M EDOT; 0.1 mg/mL DA·HCl	ITO	Aqueous Tris-HCl Buffer (10 mM; pH= 8.5)	89
Enhanced work function for solar cells	Immobilization of DA·HCl on commercial PEDOT:PSS	10 mL PEDOT:PSS; 10 mg DA·HCl	ITO-glass	Aqueous solution	91

	Chemical oxidative polymerization	1 g EDOT; 0.2 g DA·HCl	Glassy Carbon	Aqueous solution	92
Flexible optoelectronic device	Two-step chemical oxidative polymerization	(0.00-2.50 wt%) PEDOT:PSS; 2mg/mL DA·HCl	Polypropylene; polyethylene terephthalate	Aqueous Tris Buffer (0.05 mg/L; pH=8.5)	93
Hydrogel mechanical sensor for human monitoring	Chemical oxidative polymerization	0.1 M EDOT; 0.1 M DA·HCl	-	Aqueous Tris Buffer (pH=8.5) in ethanol:water (3:1)	94
Supercapacitor Electrode	Light-driven photopolymerization	DA:EDOT 1:5 mol	Metal coin; steel plate; resin dice	EtOH	95
Pseudocapacitive Electrodes	Two-step chemical oxidative polymerization followed by potentiodynamic deposition	10 mM EDOT; 0.25 mg/mL DA·HCl	ITO	Aqueous solutions of pH 8.5 (chemical synthesis) and 0.1 M LiClO4 (electrosynthesis)	96

Appendix B – Synthesis and Optimization of PDA/PEDOT Copolymers

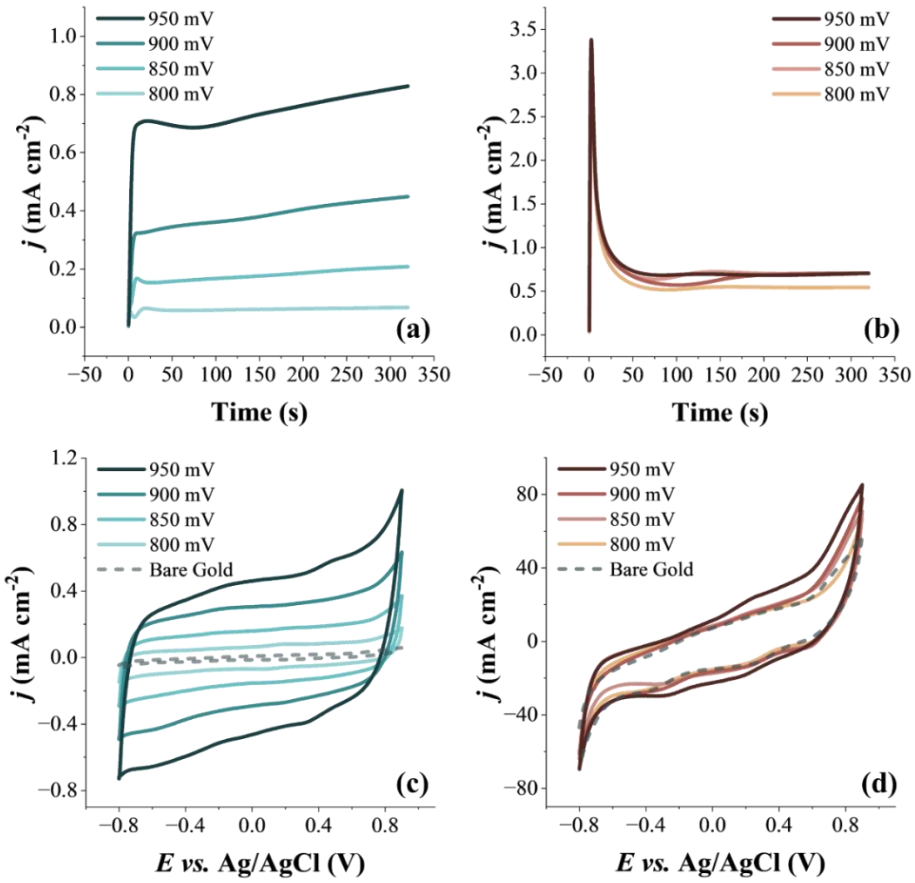

Figure B1 – (a) Potentiostatic growth of PEDOT films in 10 mM EDOT and (b) PDA films in 20 mM DA in 50 mM DS at different potentials (800 to 950 mV *vs.* Ag/AgCl) for 320 s. (c) and (d) 10th characterization cycle of the electrode in deoxygenated 50 mM of DS at 50 mV s^{-1}.

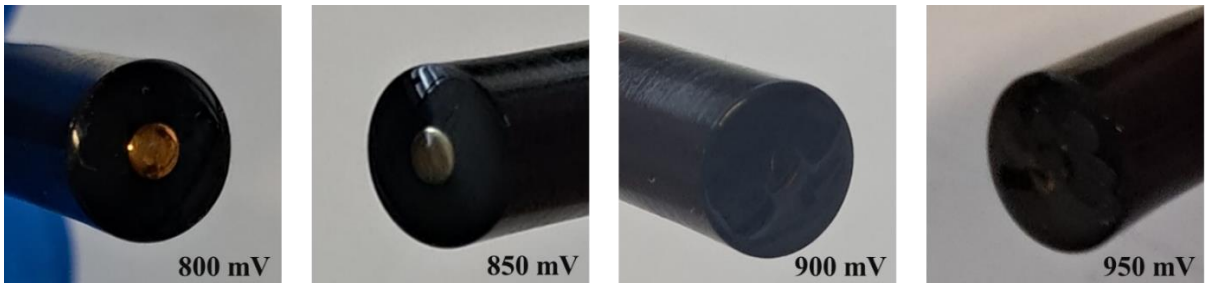

Figure B2 – Electrode after each potentiostatic deposition of copolymer under 10 mM EDOT and 20 mM DA in 50 mM DS at 950 mV (*vs.* Ag/AgCl) for 320 s.

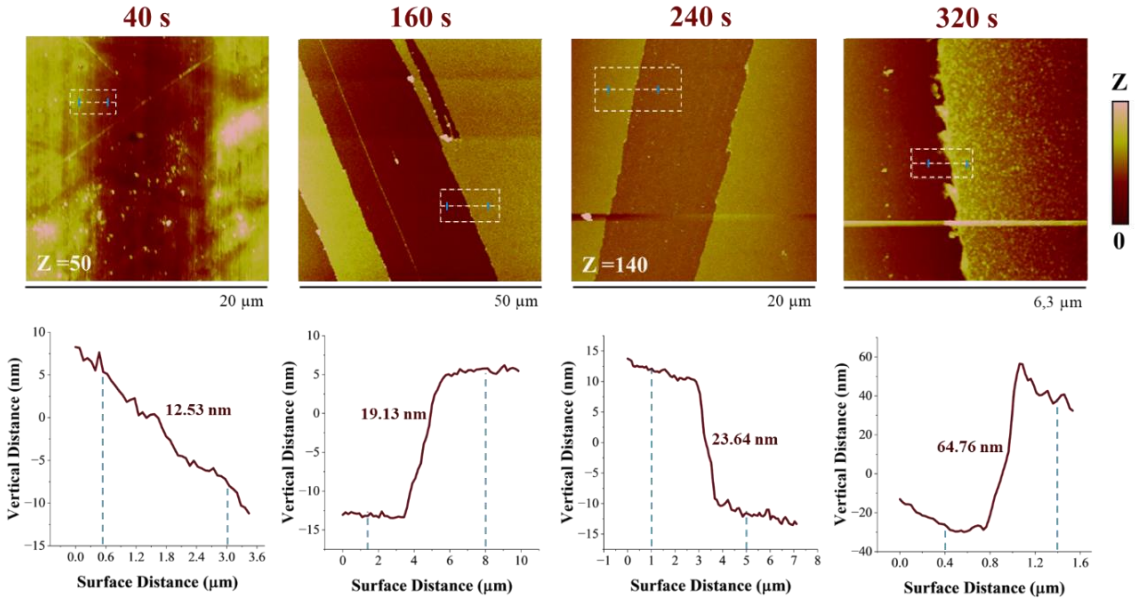

Figure B3 – *Ex-situ* AFM film thickness of the potentiostatic deposition of copolymer films (20 mM DA and 10 mM EDOT) in 50 mM of DS at 950 mV (*vs.* Ag/AgCl) in regions A (40 s), B (160 s), C (240 s) and D (320 s).

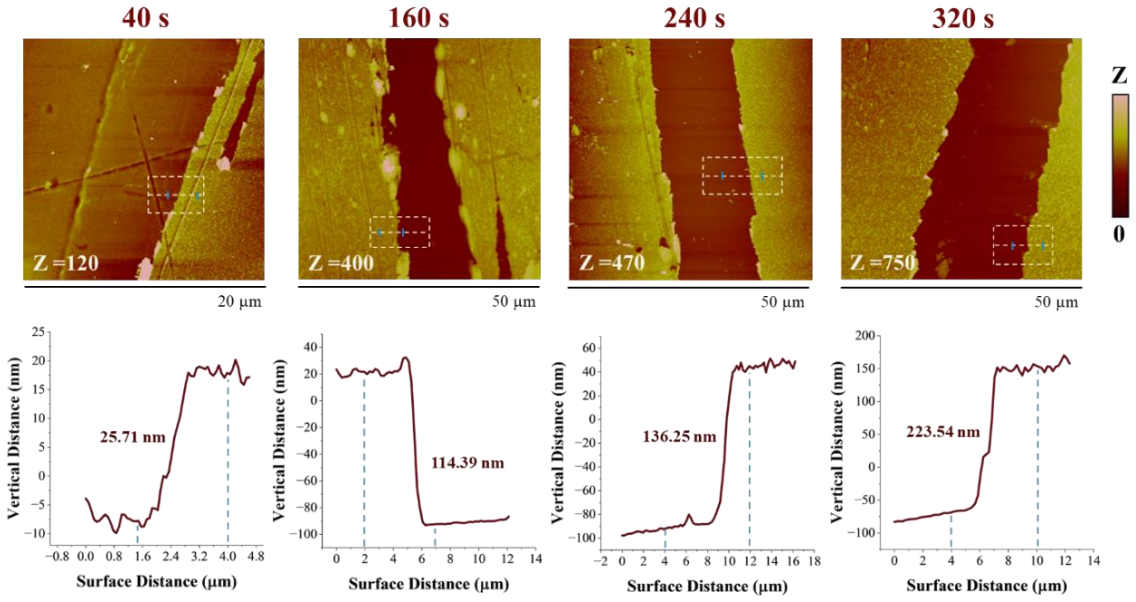

Figure B4 – *Ex-situ* AFM film thickness of the potentiostatic deposition of copolymer films (20 mM DA and 10 mM EDOT) in 50 mM of DS at 950 mV (*vs.* Ag/AgCl) in regions A (40 s), B (160 s), C (240 s) and D (320 s).

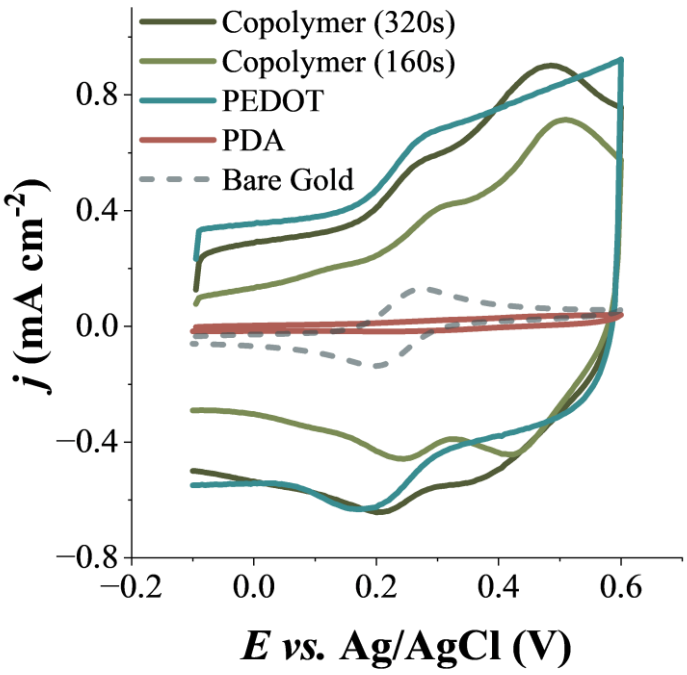

Figure B5 – Redox behavior of the copolymer films (320s and 160s), PEDOT (320 s), PDA and bare gold in 1mM $K_3Fe(CN)_6$ and 0.25 M KNO_3.

Table B1 – Wavenumber assignments for the main vibrations in the FTIR spectra of electrodeposited PDA.[87]

Wavenumbers (cm^{-1})	Assignments
1630-1548	$\nu(C=C)_{ring}$ / $\delta(NH_2)$
1159	ν(C-O)
808	$\delta(NH_2)$
783	δ(C-H)

Table B2 – Wavenumber assignments for the main vibrations in the FTIR spectra of electrodeposited PEDOT.[166]

Wavenumbers (cm^{-1})	Assignments
1556	$\nu(C=C)_{ring}$
1422-1371	$\nu(C-C)_{ring}$
1245	ν(S=O) from dopant (DS)
1144-1063	ν(-COROC-)
990	ν(S=O) from dopant (DS)
830	$\nu(C-S)_{ring}$
699	δ(C-S-S)

Appendix C – Determination of the Specific Capacity

To determine the specific capacity (mAh g^{-1}) from the potentiostatic pulses described in Chapter 4.1, the selected current (I) *vs.* time (t) oxidation transients were integrated according to the following equation, giving place to the total charge (Q).

$$Q\,(\mathrm{C}) = \int_{t_0}^{t_1} I(t)dt$$

After calculating the total charge, it was converted into the standardized unit of mAh g^{-1} to obtain the specific capacity. This was done by converting the units accordingly and dividing by the mass of the cathode material. In this case, the active mass (m) was estimated from the EQCM results presented in Chapter 3 and related to the electroactive area (A) of the electrode, as expressed in the following equation.

$$\text{Specific Capacity}\left(\text{mAh g}^{-1}\right) = \frac{Q\,(\text{As})}{3.6\, m(\text{g cm}^{-2})A(\text{cm}^{-2})}$$

For the estimation of charge retention, the charge measured at the 50th cycle was taken as the reference value for comparison across all cycles. Accordingly, the analysis was performed using the following equation.

$$\text{Capacity Retention (\%)} = \frac{Q}{Q_{50\text{th}}} \times 100$$

Appendix D – Copolymer and PEDOT film Deposition in GC and Graphite

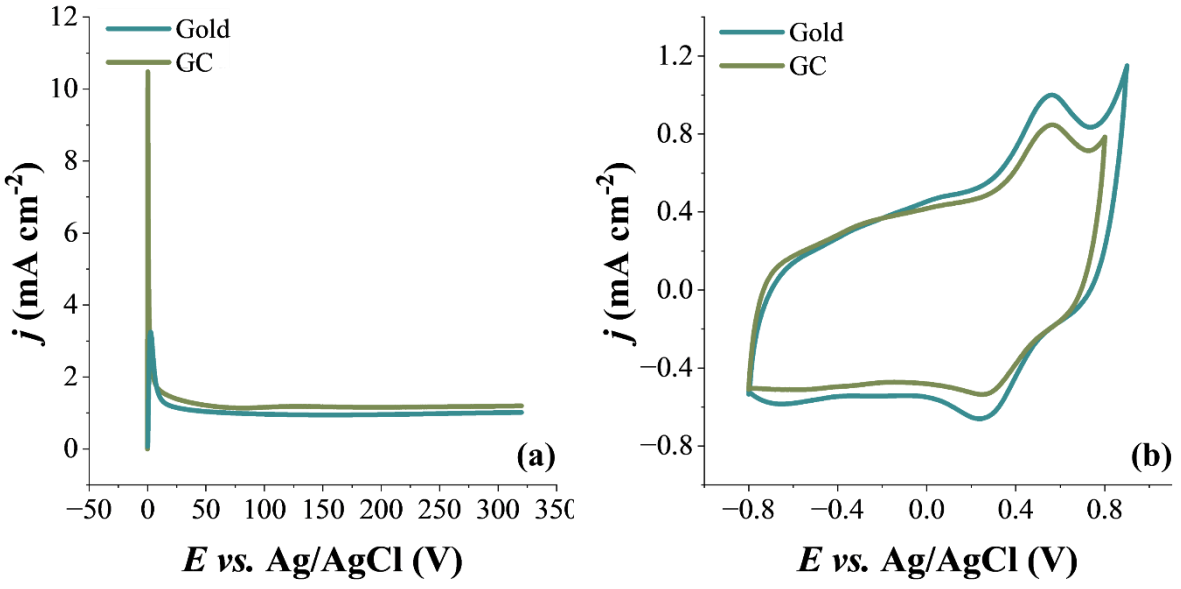

Figure D1 – (a) Potentiostatic synthesis of the copolymer (20 mM DA, 10 mM EDOT and 50 mM DS) at 950 mV (*vs.* Ag/AgCl) over a Gold and GC electrode. (b) 10th characterization cycle of the copolymer synthesized over Gold and GC in 50 mM DS at 50 mV s^{-1}.

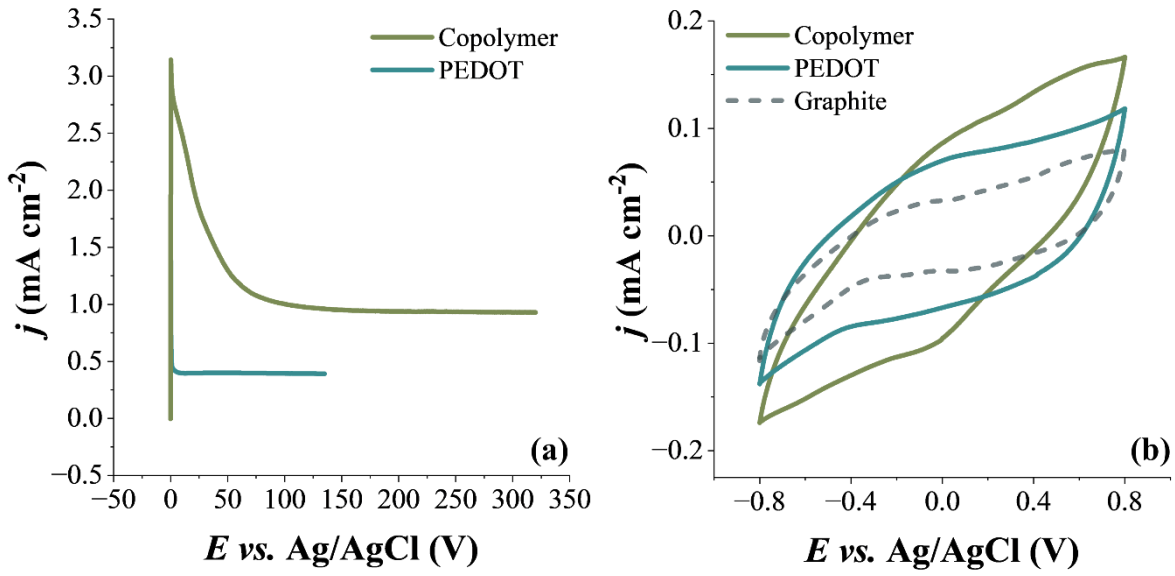

Figure D2 – (a) Potentiostatic synthesis of the copolymer (20 mM DA and 10 mM EDOT) and PEDOT (10 mM EDOT) in 50 mM DS under 950 mV (*vs.* Ag/AgCl) over graphite electrode and (b) 10th characterization cycle in 50 mM DS at 50 mVs^{-1} of deposited copolymer and PEDOT in graphite electrodes.

Appendix E – Determination of Current Pulses for Galvanostatic Cycling

To estimate the current pulses for galvanostatic cycling, the films were first characterized in 0.1M $NaClO_4$ at 10 mV s^{-1}. After this, the charge was determined by integrating the current (*I*) *vs.* time (*t*) of each oxidation and reduction process. To then estimate the currents to be applied, the calculated charge was multiplied by the desired C-rate. An example of this calculation, considering a rate of 30C, is shown in the following equation.

$$I\,(\mathrm{A}) = Q(\mathrm{Ah}) \times \text{C-rate} = Q \times 30$$

In the case of the film used for galvanostatic cycles in **Figure 4.11**, the oxidation and reduction charge were 0.0229 C and 0.0222 C, respectively. Therefore, after the previously described calculations, the current applied for each C-rate was recorded in **Table E1**.

Table E1 – C-rates and the corresponding currents estimated and applied for the copolymer material in Figure 4.11.

C-Rate	Current (*I*)	
	Oxidation	Reduction
2C	12.750 µA	12.344 µA
5C	31.875 µA	30.861 µA
10C	63.750 µA	61.722 µA
15C	0.096 mA	0.093 mA
20C	0.128 mA	0.123 mA
30C	0.191 mA	0.185 mA

Appendix F – Oxidation Reduction Reaction on Copolymer Films

In a parallel study to assess the potential of the copolymer for fuel cell applications, the ORR activity of the films was evaluated. For this, a PDA/PEDOT copolymer film was deposited over a GC electrode under the same conditions described above and characterized in deoxygenated phosphate buffer (PB; 0.1 M; pH 7) within a potential window of –700 to 400 mV (*vs.* Ag/AgCl) at 20 mV s^{-1}. Afterward, the solution was aerated for 1 h and the film was characterized again under the same parameters. This procedure was then applied to bare GC for comparison. With the voltammograms represented in **Figure F1**, it is possible to conclude that the GC electrode has little activity for ORR and in the case of the copolymer, little to no catalysis for this reaction could be detected.

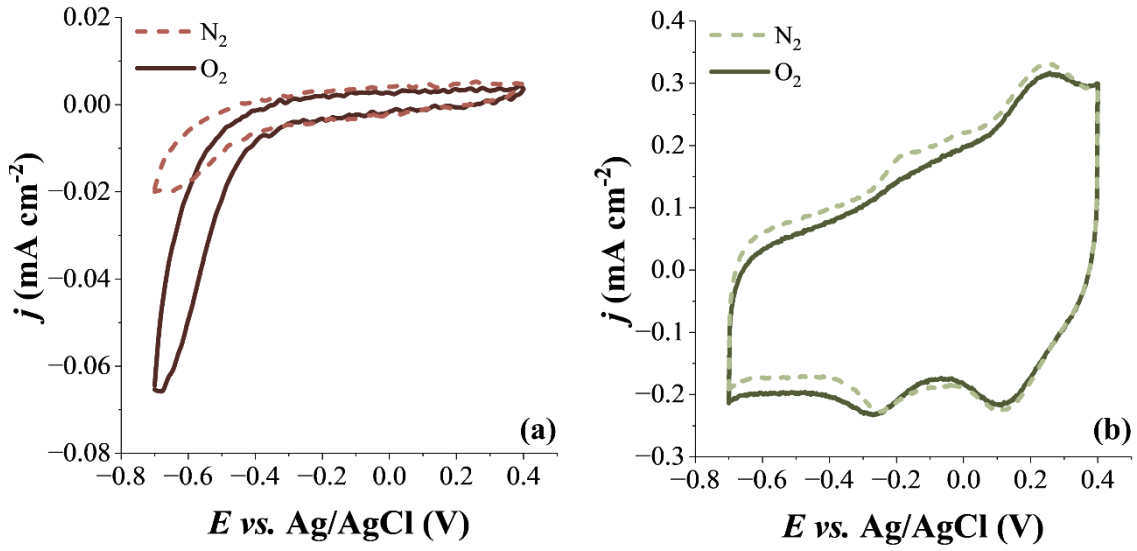

Figure F1 – Assessment of the ORR on (a) bare GC electrode and (b) copolymer film deposited on GC in deoxygenated solution (N_2) and aerated solution (O_2) at 20 mVs^{-1} in PB (0.1 M; pH=7).